Wide-area slope disaster risk evaluation using DIPM and freely-available global DTM

March　２０２０

Ahmed Muhammed Edris

Wide-area slope disaster risk evaluation using DIPM and freely-available global DTM

Graduate School of Systems and Information Engineering
University of Tsukuba

March　２０２０

Ahmed Muhammed Edris

Abstracts

Depth-integrated (or shallow water) formulation has been widely used in debris flow and river engineering simulations so far (Kalkwijk and De Vriend 1980, Hervouet 2007). Recently, this formulation has been applied into particle method (Pastor et al. 2009, 2014). A simplified version of this method called Depth Integrated Particle Method (DIPM) had been used by previous researchers in the division the Geotechnical laboratory under the department of the Energy and Mechanics Engineering of the University of Tsukuba. Nakata (2017) made a pioneering work on evaluation of wide-area landslide hazard using DIPM and GIS applying to two wide-areas as a case studies: the Nova Friburgo (6.72 km by 4.5 km) in Brazil and the Hofu (4.75 km by 2.50 km) in Japan. And a mixing model based on a two-step evaluation scheme was proposed together with DIPM by Zhang (2015) to quantitatively evaluate the debris flow hazards in Zhouqu and Wenchuan earthquake stricken areas.

However, in these mentioned works, a precipitation simulations were not taken into account which is a necessary approach to locate the water catchment area where most of the erosions and sediment processes occurs. It is essential also to identify a potential soil saturation area which contributes in the delineation of the initial slope failure area and the maximum debris flow affected drainage channels. Moreover, a new approach of calibrating the material parameters of the numerical model was implemented here using a recorded landslide events for a selected case study area in Japan by considering only the initial and final deposition places of each debris flow surges which was not taken into account by previous workers. We identify the lower and upper bound values of the material parameter which were used to evaluate the most and the least risk regions for the case study area in Ethiopia where the available in situ records of the affected area and a documented mechanical test results of the material parameters are rarely available.

The methodology implements a twofold strategy: first we assess a slope disaster risk in the given area by evaluation of the stability condition of the slopes using the available records. There are several classical ways to evaluate the stability of a slope and yet the subject is arguably the most complex and challenging sub-discipline in geotechnical engineering. We used a 1D slope formula to compute factor of safety (F_S) of a slope with the assumption that a critical slope failure angle (θ_f) can be roughly evaluated from the available record of the saturated and unsaturated bulk density and the depth of the ground water of the unstable mass under consideration.

Secondly, after a surface soil mass fails and starts to slide, usually it will be mixed up with masses of liquids and the flow behavior of the mixture is strongly influenced by its material properties such as size distribution of geological grains (from micron scale to meter scale), grain shape and crushability, water contents, etc. However, there are no universal constitutive laws governing landslides that are straightforward to incorporate into numerical models (Pastor et al. 2012). Moreover, what is necessary for wide-area risk evaluation of landslide hazards is not a sophisticated and highly accurate constitutive models but rather primitive ones with the smallest number of material parameters that can be easily identified. Therefore, a simplifications of constitutive models appears to be a reasonable approach towards a systematic application of simulating the deposition process of debris flows.

We have developed a simple depth-integrated particle method (DIPM) which is a simplification of an SPH. The model is based on depth-averaged shallow flow equations solved on a set particles obtained from the Digital Terrain Model (DTM) constructed using Grass GIS open source application software. The resultant forces acting on each particle is considered to be similar to the forces acting on the columns of soil in a limit equilibrium slope-stability analysis in which the gravity force and the hydraulic pressure are the driving forces and the resistance force to motion comes from the basal shear stress computed from Manning's formula combined with the equation of steady and uniform flow. Hence the model contains only two material parameters, the Manning's coefficient n and the critical slope angle for the flow θ_{cr}. The former is the most common parameters used in river engineering to characterize the flow resistance of river channels and stream canals. The latter can be regarded as the final slope angle that debris flows stop. Previous disaster surveys show that the deposition angle of debris flow ranges from 3 degrees to 15 degrees depending on the material and water contents (Hungr et al 2001).

The hydraulic pressure was determined by the interaction between the neighboring particles and thus it was affected by mesh size of a DTM used to acquire information about the topography of the area of interest. In this study we construct a DTM from worldwide digital sources offered at 30-m and 12.5-m resolutions. The ALOS 30m was obtained from Japan Aerospace eXploration Agency (JAXA). A relatively smaller mesh size DTM at 12.5-m that has a higher resolution was obtained from ALOS-PALSAR (Phase Array type L-band Synthetic Aperture Radar) developed

(Alaska Satellite Facility (ASF), 2015). Another freely available DTM was also derived from Google earth application by extracting elevation values using free software called TCX converter.

ALOS 30-m was used for wide area slope disaster risk evaluations in the case study areas in Ethiopia after evaluating its accuracy by comparing with a 10-m resolution DTM constructed by stereo-photogrammetric method from images taken by ALOS. The results showed a similarity of cross sectional views at a longer length profiles but at a closer view the ALOS 30-m DTM showed some local flat planes problems which was corrected by a simple adjacent average smoothing by adding points along the path so that the model fits a smooth functions.

A similar comparison was made between the ALOS 30-m, ALOS 12.5-m and airborne survey 1-m DTM. And it was seen that the terrain correction made by Alaska Satellite Facility enhanced the resolution of the ALOS 12.5-m DTM.

We also made a comparison between the ALOS 12.5-m and airborne survey 1-m DTM its ability in reproducing actual events using the numerical models. The results of the model runs using the two DTMs was compared on the basis of identifying each surge of the debris flow and on the basis of an agreement in the depositional patterns with observations. For a very local area investigations the result showed that the applications of freely available DTM can be limited only to give an approximate overview about the area of inundation and can serve also as a first estimates of the areas potentially affected by mass flows. However, for a wide area incidents, with a deep-seated slope failure that usually happen in many places of Ethiopia, having several kilometers width and lengths, the DTM from ALOS 30-m after a correction of the local flatness and from ALOS 12.5-m without need of correction was found to be capable to be used in the evaluation of slope disaster risks using a calibrated material parameters.

There are several approaches to calibrate the material parameters of numerical models. We used a calibration technique based on a visual comparison of the main external aspects of landslide behavior such as how far do the debris flow travel and how wide do the flow spread in the deposition fan. Though this approach is subjective, it is simple to implement when the model contains few adjustable parameters that dominate characteristics of flow behaviors.

The initial slope failure area need to be determined in advance in order to calibrate the flow parameters (n and θ_{cr}). This is due to the flow inundation results are sensitive to the initial mass discharges of the debris flow. Therefore we employ a user defined assignment of the initial slope

failure area, for a debris flow involving a single surge (the Kumamoto area). However, due to the inconvenience of user defined assignment for a debris flow with multiple number of surges (Hofu case), we use a critical slope failure angle, θ_f to locate these places. From the sensitivity analysis between the initiation area obtained using some slope inclination and the actual slope failure area, it was able to select 40 and 42 degree for the western and eastern side respectively, to locate the initial slope failure zone in this area.

For the Komamoto case study area it was seen that the case for smaller n (smaller bottom shear stress) leads to an excess flow acceleration and results in the too much deviation from the path of valley bottom in the upper stream. On the other hand, in the downstream deposition fan, the simulated inundated width is narrower than the observed one for larger n. Using a comparison at time history of the maximum velocity of the flowing mass with the evaluation by Mizuno et al. (2003) a lower and upper bound value of (n and θ_{cr}) was estimated to be in the range (0.05 to 0.10, 5 to 7 deg.). For Hofu case study area range values between (0.05 to 0.08, 0.5 to 7 deg.) was estimated to be fitting for the western part of the study area. And a range values between (0.05 to 0.08, 0.5 to 4 deg.) was estimated to be fitting for the eastern side of the study area.

A similar approach proposed by Galas et al (2007) was adopted with addition of an index value to separately maximize the intersection between the predicted and observed failure area and both failure and the safe area distinctly for the Debre Sina landslide area . It was found that the index values were maximum until a critical slope failure angle of 32 degree.

A relatively higher number of particles were also found corresponding to the main and major initial slope failure area estimated by slope inclination value of 32 degree. After estimating the initial slope failure area we used the calibrated material parameters of the model to replicate the past landslide event. The replication of past landslide event was made using two extreme cases of the calibrated parameters, namely the lower bound values ($n = 0.05$ and $\theta_{cr} = 0.5\ deeree$) and upper limit values ($n = 0.08$ and $\theta_{cr} = 7\ degree$).

The lower bound values replicated a simulation debris mass under highly fluidized condition thus the simulated showed several number of surges which reveals its impact energy, that represent one of the most destructive cases. These replicated results were in agreement with the investigations made in the study area by previous researchers. In the case of upper bound values the simulation

results reproduces a deposition of debris flows with shorter runout distances both in the upper slope failure area and the lower river canals.

For the Ankober area, we used the topographic map of the study area together with the satellite images taken in the year 2019 to identify the places that demands to be protected primarily such as villages, roads, and forest covered areas. We set a higher critical slope failure angle $\theta_f = 43^o$ to predict the initiation area. From the overlap of the predicted slope disaster area and the topographic map it was seen that the eastern and western side of Ankober town, the road that connects to the capital city and the forest cover area are found to be near the predicted dangerous slope failure zones.

Before we made a flow spreading simulations using the two extreme cases of the calibrated parameters, we made a precipitation simulations to identify the most vulnerable places for surface erosions and debris flow deposition areas. The result showed a high concentrations of simulated raindrops in the eastern most side of the study area. Simulations were made using the two extreme cases of the calibrated parameters, namely the lower bound values (n=0.05 and θ_{cr}=0.5 degree) and upper limit values (n=0.08 and θ_{cr}=7 degree). In both cases of the simulation results obtained by the calibrated parameters of the lower and the upper bound values, it was seen that the identified places such as villages, roads, and forest covered area that necessitates to be protected primarily were simulated to be under high slope disaster risks.

Moreover from the overlap of the simulated results and the satellite images, it was found that the most possible debris flows occurrence could be in the flood plains covered with trees or heavy brush, whose Manning's coefficient n is about 0.1. A most dangerous case of a flow was also assumed by setting θ_{cr} a zero value. The results found using these material parameters showed a wide inundated area having a high value of velocity and it covers relatively large number of houses. The predicted flow velocity at the initial stage was much higher than the previous case study areas due to a comparatively steep slope failure angle value more than 43 (deg.) occur in this area. The mean velocity of the predicted flow was found to be quite large value compared to the mean velocities of common debris flows under a channel gradients varying from about 40° in the starting zones to about 3° in the deposition zone (Hutter et al 1994). In general, the results showed the potential damages of slope disaster risks in the area and the necessity for further investigations.

The key issue here is to develop a method that is capable to obtain important material parameters from available in situ records that show the initial slope disaster locations as well as the extent and distributions of the debris flow surges in the given area. The availability of a model that can be integrated with a terrain model obtained from a global freely available sources through an open source Grass GIS application make it essentially applicable all over a slope disaster susceptible places for both experts and practitioners, while models that are commercially available tend to be expensive. Moreover the model results are found to be directly applicable into risk assessment calculations in order to be used as a visualization and communication tools.

However, several key challenges remain, particularly the sensitivity of models to topographic resolution. Prediction of the flow-path and the deposition fan of the debris flows is found to be more reliable with airborne survey high resolution terrain source compared to a freely available global source. However, calibration of the model parameters using globally available terrain source with identical resolutions all over the world will resolve the differences in the values of material parameters due to topographic resolutions.

It also turned out that the prediction of initial slope failure is still a big issue to be improved. For more accurate prediction, we incorporated erosion behavior of debris flow into the model. Zhang and Matsushima (2016) proposed a simple diffusion model to describe the entrainment of debris material resting on the valley bottom by the flow.

Moreover, it should be recognized that calibrated parameter values can depend strongly on the roughness of the input topography; therefore, until a standard approach to model setup is adopted widely, calibration results documented by different workers using different models may not be directly comparable. Therefore, the model need to be applied to several case studies in central and escarpment area of the highlands of Ethiopia in order to create a valuable database of calibrated parameters. Detail geotechnical field investigations and laboratory works need be done to adjust the input parameters for specific to the geologic and topographic conditions of Ethiopian highlands.

Table of contents

List of Figures

List of Tables

1 Introductions

1.1 Problem statement

Wide area slope disaster risk evaluation is an essential duty in landslide-threatened areas throughout the world. Slope disaster risks, frequently lead to loss of life, property, and infrastructures in mountainous areas. It involves collapsing of soil or rock material which may proceed by flowing of soil and water mixtures sliding downslopes. Evaluating such risks needs to consider ground conditioning factors that made slopes susceptible to movement such as the type the soil/rock conditions and geomorphological characterization such as slope angle and altitude.

Landslides remain initiated often by failure of slopes due to a torrential rain and/or large earthquake, generating sliding mass of soil-water mixture which flows down more than tens of kilometers as a debris flow (Aipassa, 1991). Depending to their fluidity, they can travel long distances, often reaching the valley floor and moving beyond. During the course of their travel, the flows erode river beds, increasing the involved volume of mass which enhances the destructing nature of such events.

Landslides that change into flows usually are characterized by high-velocity movement and long run-out distance that exert the paramount threat to human life. This is because, in the highlands, usually settled areas are located near to drainages and river channels because these areas are more favorable to urban development (Sidle et al 2004). Consequently these regions are vulnerable for risk of slope failures and flows. Therefore, slope failures and flows are a source of severe natural disasters and societal hazard in mountainous regions.

Yearly property destruction from slope failures worldwide is estimated in the tens of billions of dollars (Schuster et al 1986). There are countless small to large-size slope failures that cumulatively inflict costs to people life and damages to infrastructures due to catastrophic events that draw so much attention (Shang et al 2003). Destruction to ecologies has not usually been predictable, that such events may destroy territories, for example by hindering streams and shedding slopes. All these damages demand for a multidisciplinary and combined methodology to hazard assessment and risk mitigation and preventions (Renn 2008).

The data show that in total 55, 997 people were killed in 4862 distinct landslide events in the period from January 2004 to December 2016 excluding those triggered by earthquakes. The majority of

the events involved a single slope failure and their spatial distributions (Figure 1) is clearly heterogeneous with high areas of incidence in cities and occur most frequently in countries with lower gross national income (Froude et al 2018).

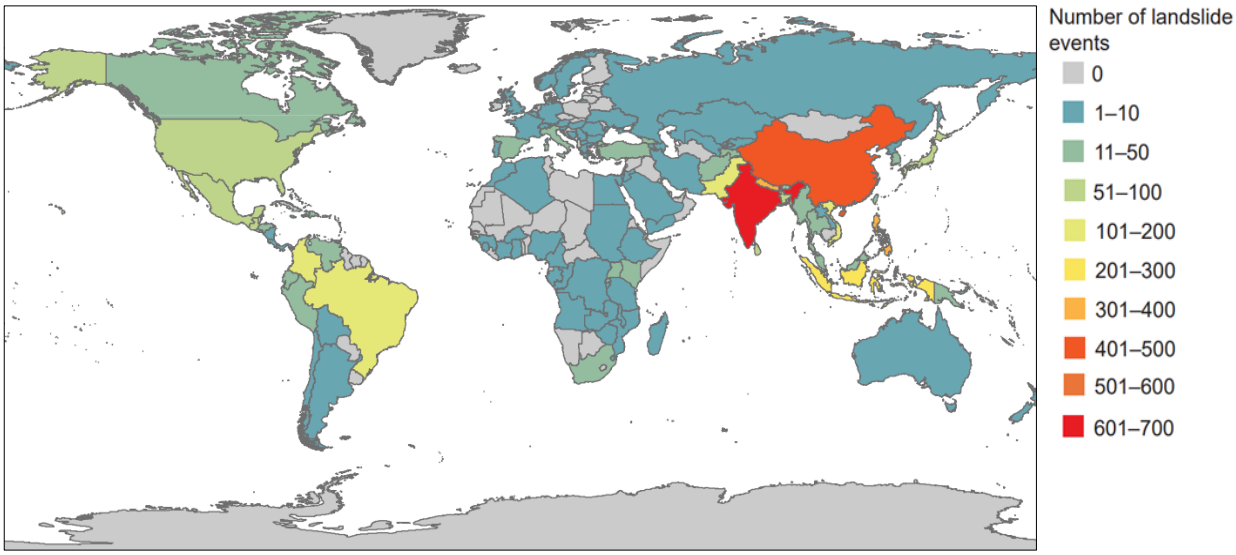

Figure 1 worldwide non-seismically triggered landslide events (from 2004 to 2016) (source: Froude et al 2018)

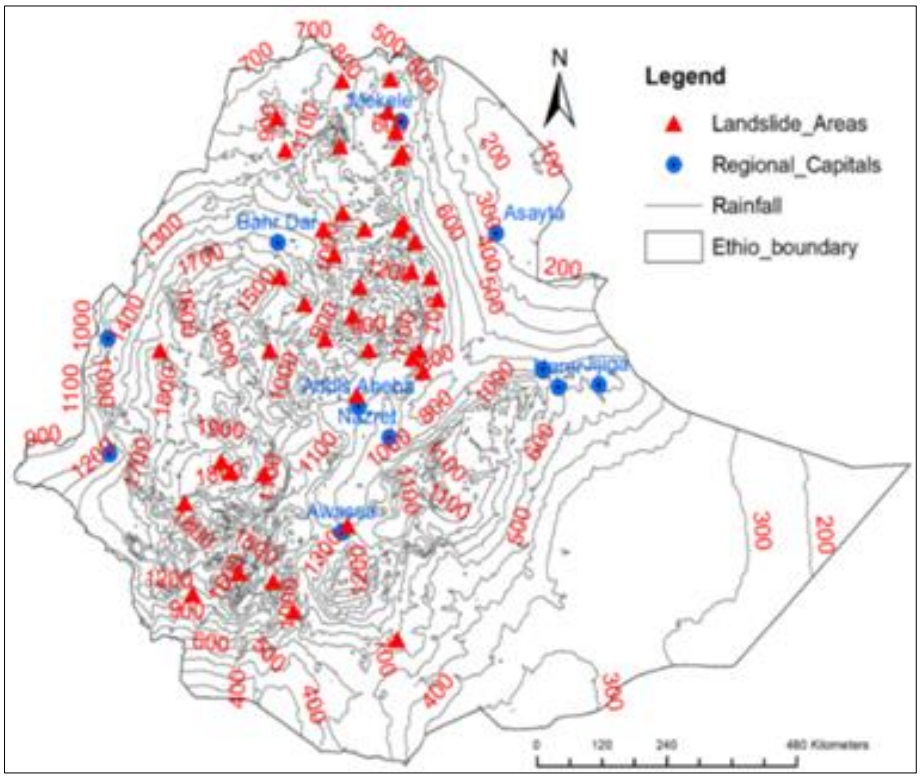

Figure 2 location map of reported occurrences of landslides in Ethiopia. Source: Woldearegay 2013

In Ethiopia, slope failure-generated hazards are becoming serious concerns. The ruggedness of the topography, the capricious seasonal rainfall and the seismicity of the Horn of Africa aggravated the incidents (Fubelli et al 2015). These slope disaster incidents often lead to eviction of inhabitants, damage to

housing, infrastructure and arable land and even loss of human lives (Woldearegay et al 2013). In a recent occasion an Ethiopian news service reported that at least 41 people have been killed when the heavy rain triggered a landslide in place called Kindo Didaye district on 09 May 2016 (http://floodlist.com). A summary of the major slope failures reported so far in the country is shown in Figure 2.

A densely distributed reported occurrences exits mainly in the central highly populated area of the country. It can be seen also that some of the regional government towns including the capital city Addis Ababa are exposed to such threats caused by risks of slope failures. The major patterns of distributions are lined north-northeast south-southwest following similar alignment with active volcano epicenters in the history of the African Rift System (Figure 3).

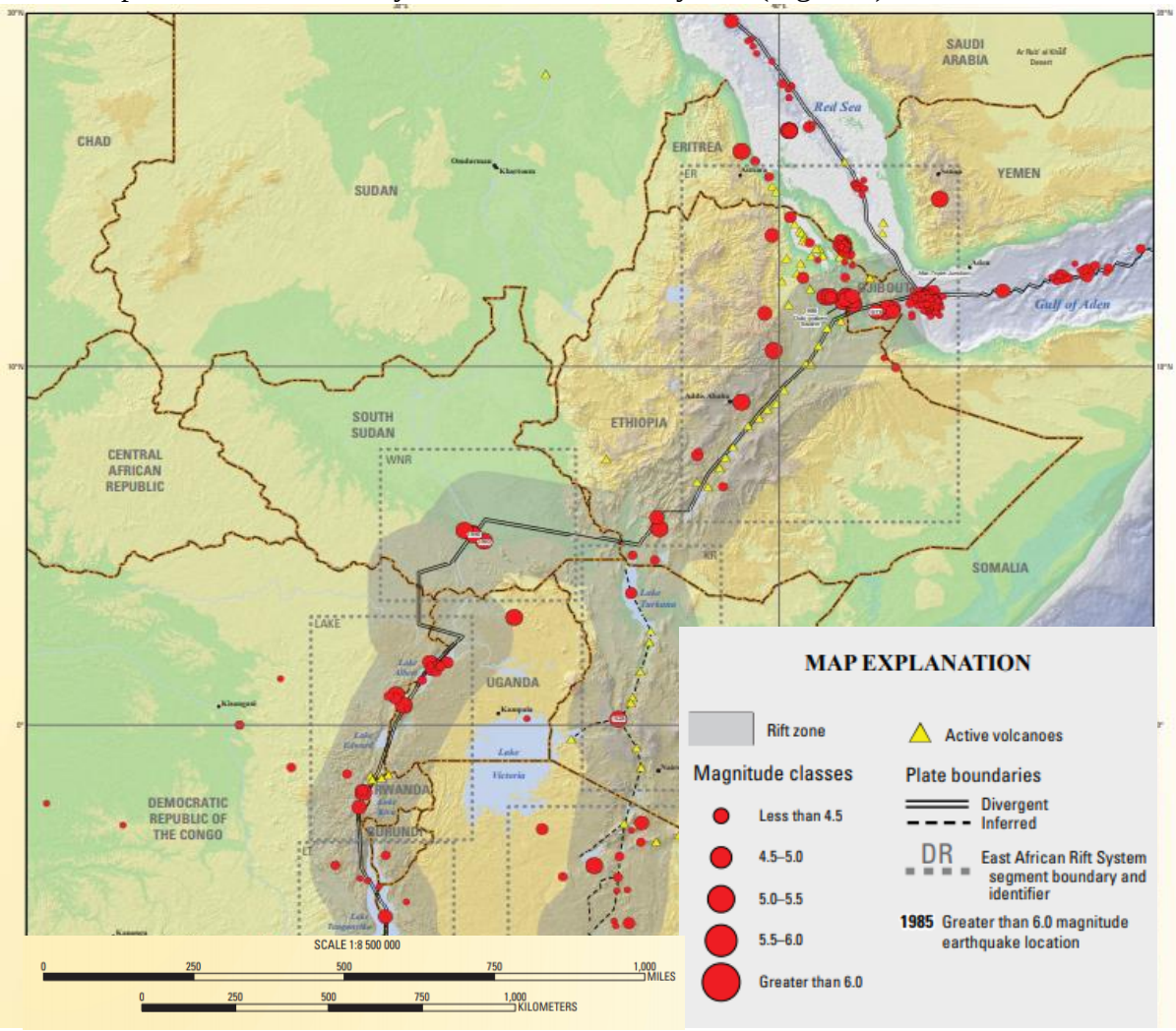

Figure 3 Seismicity of East African Rift 1900–2013 source: Hayes et al 2014 USGS Open-File Report 2010–1083–P

The East African Rift System is a diffusive extensional region marking a triple junction, where three plates named as Somalian and Nubian plate in African, and the Arabian plate meet. It is prone to significant level of seismic hazard due to the presence of the active regional tectonic and volcanic activities.

Moreover, the sustainability of most people is from sources of foods which depend on the productivity of the land. However, the topsoil is eroded and ruined by the landslides and associated hazards. The slope failure in the highlands are also main sources of debris-flows that cause floods which damage the agricultural lands in the lowland areas. Besides, due to the escalation of overburden on the land, many rural individuals are moving into areas which are potentially threatened by slope instability hazards.

1.2 Disaster risk management in Ethiopia

Since April 2018, the Ethiopian National Disaster Risk Management Commission, Early Warning and Emergency Response Directorate (NDRMC)-led a multi-sector National Flood Task Force and issued the first Flood Alert based on the National Meteorology Agency (NMA) Mid-Season Forecast for the season (April to May 2018).

Subsequently, on 20 May, the National Flood Task Force updated and issued a second Flood Alert based on the monthly NMA weather update for the month of May 2018 which indicates a geographic shift in rainfall from the southeastern parts of Ethiopia (Somali region) towards the western, central and some parts of northern Ethiopia including southern Oromia, some parts of SNNPR, Amhara, Gambella, Afar and Tigray regional states during the month of May 2018.

Flood risk areas were identified (Figure 4). The condition of flooding is characterized by sudden onset with little lead time for early warning and often resulting in considerable damage on lives, livelihoods and property. These risk areas are mainly concentrated in the landslide prone areas aligning with the escapements between the highland and lowland region and the rift margins areas in central part of the country.

Getahun and Gebre (2015) rated and combined flood generating factors such as slope, elevation, rainfall, drainage density, land use, and soil type to delineate flood hazard zones using a multi-criteria evaluation technique in a GIS environment. According to their findings nearly 2,103

and 35,406 km^2 area were found to be in a very high and high flooding hazard conditions along the Awash River basin alone.

According to Fubelli et al (2008) the main triggering factor of slope movements in Ethiopia is heavy rainfall. Canuti et al. (1985) pointed out that infiltration of rain water plays a pivotal role in triggering landslides by increasing the total weight of the slope material as well as the water table level and the pore pressure in fine-grained deposits thus weakening the links between their component particles.

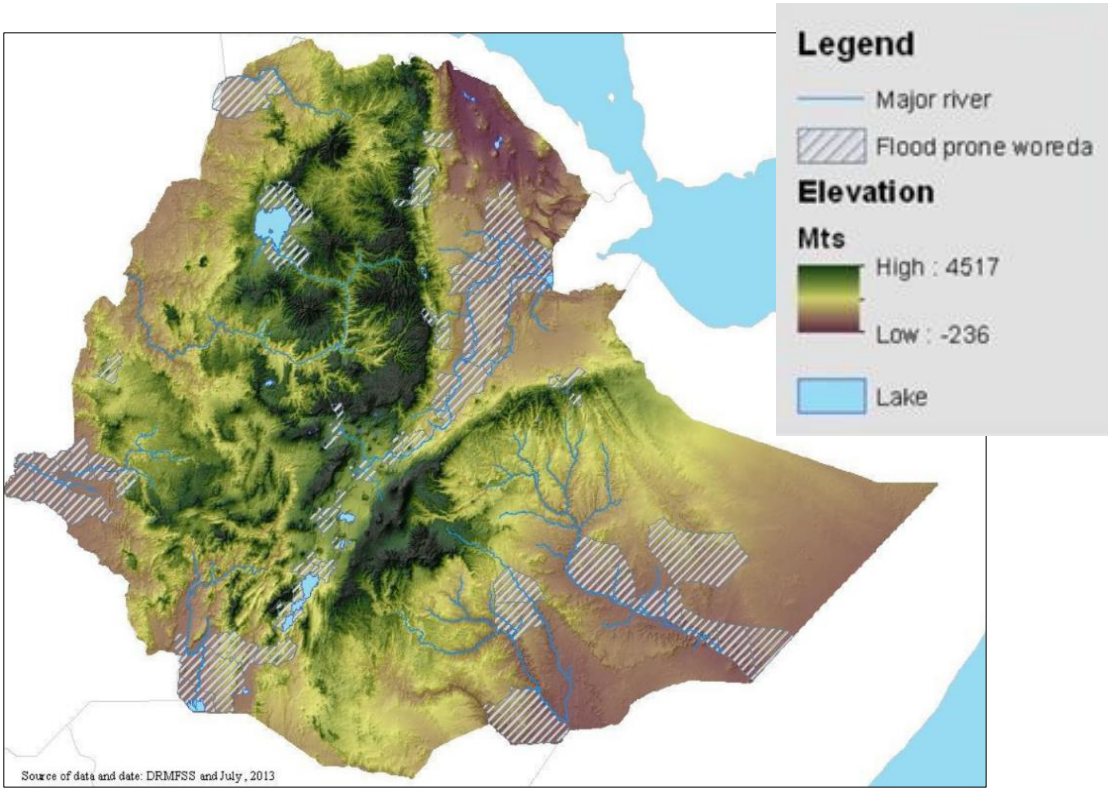

Figure 4 Identified flood prone areas in Ethiopia.

1.3 General objective of the research

In order to protect peoples and infrastructures of these areas, mitigation measures are needed to be taken. The extent to which a potential area is vulnerable and the intensity of the impact have to be identified to assess the risk. The prediction of the flow propagation (deposition area and its influence) is essential. This analysis can provide relevant information for land use planning and susceptibility mapping. Therefore, prediction of the affected places, including the potentially vulnerable populated sites, is of great relevance in slope failures and flows risk assessments.

Many researchers in the universities and studies in the institutes had been given emphasis to understand slope failures and associated landslides and debris/earth flows (Ayalew et al 2004). Statistical index and certainty factor methodologies were implemented to investigate coactive factors for landslides in the Blue Nile gorge (Asfaw 2010). Remote sensing techniques for the investigation of a large landslide occurrence with a difficult accessibility were implemented to provide information about its extent, kinematics, zonation and evolution over time of a landslide that occurred around Debre Sina town (Kropáček et al 2015).

Numerical simulation methods have been used as an alternative technique of doing time-consuming and hard works in both field survey and experiments. Simulation methods provide more useful results than the traditional experimental methods in terms of displaying insightful and whole round information that cannot be directly measured or detected, or difficult to explore through other ways (Liu and Liu, 2003). Moreover, numerical models have the potential to provide more information because they can also be used to estimate relevant landslide intensity parameters, such as flow depths, flow velocities, and impact pressures, within a certain limits (Mcdougall 2016). Nevertheless, researches and studies in Ethiopia made thus far seldom employ the application of numerical simulations for the analysis and identifying potentially slope failure areas and propagation and deposition patterns of debris/earth flows associated with such slope failures. There have been limited comprehensive studies with diverse methodological practices (Haregeweyn et al 2017). These margins in diversifying the methodologies of forecasting and evaluation slope failures and flows problems comprises the basic motivations.

Depth-integrated (or shallow water) formulation has been widely used in debris flow and river engineering simulations so far (Kalkwijk and De Vriend 1980, Hervouet 2007). Recently, this formulation has been applied into particle method (Pastor et al. 2009, 2014). A simplified version of this method called Depth Integrated Particle Method (DIPM) had been used by previous researchers in the division the Geotechnical laboratory under the department of the Energy and Mechanics Engineering of the University of Tsukuba. Nakata (2017) made a pioneering work on evaluation of wide-area landslide hazard using DIPM and GIS applying to two wide-areas as a case studies: the Nova Friburgo (6.72 km by 4.5 km) in Brazil and the Hofu (4.75 km by 2.50 km) in Japan. And a mixing model based on a two-step evaluation scheme was proposed together with DIPM by Zhang (2015) to quantitatively evaluate the debris flow hazards in Zhouqu and Wenchuan earthquake stricken areas. However, previous researchers did not includes a

precipitation simulations which is essential to locate the water catchment area where most of the erosions and sediment processes occurs. This helps to identify a potential soil saturation area and thereby contributes in the delineation of the initial slope failure area and a debris flow vulnerable drainage channels.

Moreover, in this research work a calibration of the material parameters of the numerical model was made using a recorded landslide events for a selected case study area in Japan by considering only the initial and final deposition places of each debris flow surges rather than making the comparison of the accuracy of the model in its ability to replicate the whole affected area by both the initial slope failure and the subsequent debris flow events which was made by previous researchers. This helps to identify the lower and upper bound values of the material parameter that can be used to evaluate the most and the least risk area using these calibrated parameters for the case study area in Ethiopia where the available in situ records the affected area and a recorded mechanical test results of the material parameters are rarely available.

Models that are calibrated in one case study area can also be potentially well-suited to another area with a similar geotechnical conditions. The calibration was done on the comparison of the agreement between the simulation and observation on the basis of identifying the initiation and deposition fan of each surge of the debris flow in the study area. This approach is applicable for a model with unsophisticated rheological parameters but adequately capability of simulating the bulk behavior of inundation and the distribution of deposits, which is the main goal in a wide-area risk evaluations. In some cases, this approach may also have convenience and cost effectiveness in practice because specialized material testing is not required (McDougall 2016).

1.4 Specific objectives and outlines of the methods

From the general objectives, the following specific objectives were formulated:

1. To design and evaluate a suitable rheological models for wide area slope disaster assessments.
2. Explore the material parameters of numerical models.
3. Calibrate the parameters the numerical model using actual slope disaster case study areas.
4. Evaluate the resolutions of the digital terrain models obtained from global freely available sources.

We consider two case study area in two countries, namely in Ethiopia (the Debre Sina landslide and Ankober rift margin area) and in Japan (Kumamoto prefecture and Hofu city debris flow and shallow landslide events). It is organized in 7 chapters.

After an introductions in the first chapter we give a detail literature review of slope stability analysis and assessments of the current status of the numerical simulation models in the second chapter. In the 3rd chapter we made a comparison of a 30 meter mesh size (ALOS 30-m) digital terrain model (DTM) obtained from Japan aerospace exploration agency (JAXA) and a DTM obtained from google earth application, with a 10m mesh size DTM obtained under commercial dealing. We also use a high resolution airborne survey 1m mesh size DTM to compare a 12.5 meter mesh size DTM freely obtained from ALOS 12.5m global source. And the effect of the resolutions of the DTM from these sources on the numerical simulation results were also investigated.

In Chapter 4 we give a detail formulation of the proposed numerical method. Then, in chapter 5, we demonstrate the calibration of the material parameters of numerical model using the performance of the method from a case history in Kumamoto and Hofu area in Japan. In chapter 6 we made application of the method into wide area risk evaluation in Ankober and Debre Sina area in Ethiopia. The final, chapter 7 contains conclusions and recommendations.

1.5 Methodology

The first step in the process of evaluation of wide area landslide risk begins with a preparation Digital Terrain Model (DTM) to represent the topographic feature of the area of interest. Previous researchers in this field construct the DTM of the study area from stereo-photogrammetric method from images taken by the PRISM sensor mounted in ALOS satellite (Nakata 2016 and Zhang 2019). However for regions with difficulty of accessibility the preparation of DTM from freely available global sources is inevitable. In this study we prepare DTM from worldwide digital elevation sources which were obtained free of charge with 30-m and 12.5-m mesh.

We compared the resolutions of the DTM from these sources with a more accurate ALOS 10-m commercial and 1-m airborne survey sources. And the effect of the resolutions of the DTM from these sources on the numerical simulation results were also investigated.

A conventional linear stability analysis for each pixel of the DTM was adopted by considering the physical and mechanical properties of surface soil at rest, including the water saturation, and the demarcation of the area of initial slope failure. Finally, the flow simulation is carried out for the entire area to obtain the affected area due to the slope failure and the subsequent flow and the simulation result then compared with the actual damage area in a quantitative manner. Figure 5 shows the flowchart of evaluation procedure.

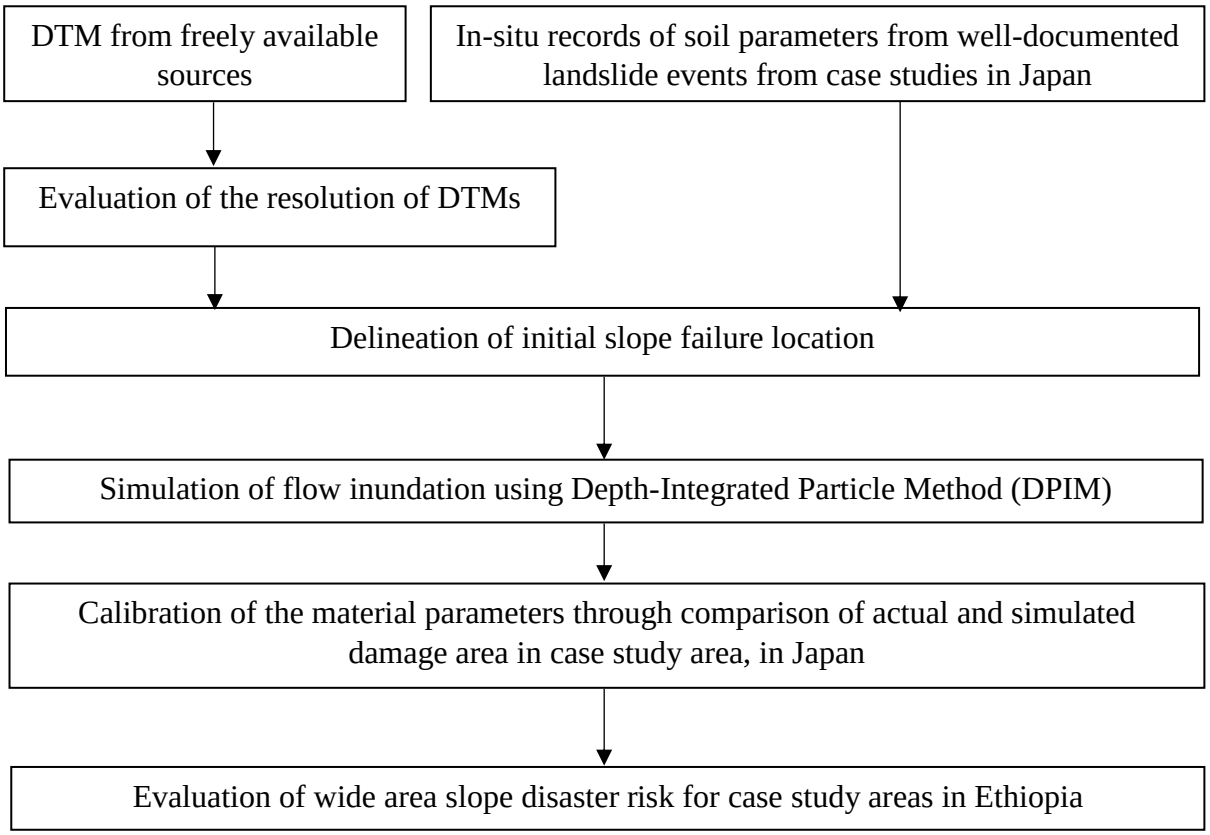

Figure 5 Flowchart of wide area slope failure risk evaluation

2 Literature review: slope stability analysis and assessments of numerical simulation models

2.1 1D slope stability

The equation of Safety Factor (F_S) have been implemented to analyze the stability of natural slopes. Several safety factor formulations were introduced such as Fellenius method (Matsui et al 1992), Bishop Method (Hungr et al 1989), etc. We adopted a basic formula of the Safety Factor (F_S) of a slope (of soil material) defined as equation (2-1) with the assumption that the angle of the slope failure can be roughly evaluated by in-situ records of the area for the case of shallow one dimensional (1D) slope failure as presented in scheme shown by Figure 6.

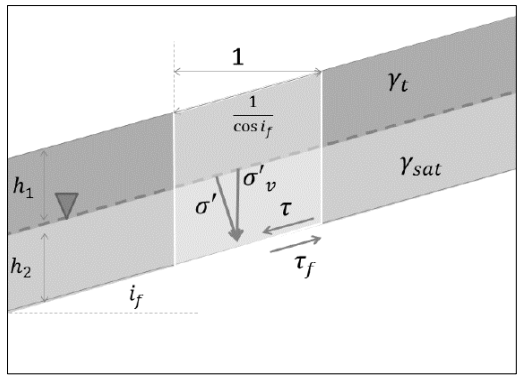

Figure 6 scheme for 1D slope stability

$$F_s = \frac{shear\ strength\ of\ soil}{shear\ stress} = \frac{\tau_f}{\tau} \qquad 2\text{-}1$$

Here, the shear strength of the surface soil is given as equation (2-2)

$$\tau_f = C' + \sigma'_v \tan \emptyset' \qquad 2\text{-}2$$

Where C' and $\emptyset'$ are the cohesion and the internal friction angle of surface soil, respectively and $\sigma_v{}'$ is the effective normal stress given as equation (2-3):

$$\sigma'_v = \sigma_v - \gamma_w h_2 \cos i_f \quad where \quad \sigma_v = (\gamma_t h_1 + \gamma_{sat} h_2) \cos i_f \qquad 2\text{-}3$$

The shear stress τ in equation (2-1) is given as in equation (2-4):

$$\tau = \sigma_v \sin i_f \qquad 2\text{-}4$$

Then substituting equation (2-4) in to equation (2-1) and using the expression in equation (2-2) and (2-3) the formula of the Safety Factor (F_S) can be given as equation (2-5):

$$F_s = \frac{C' + \{\gamma_t h_1 + (\gamma_{sat} - \gamma_w) h_2\} \cos i_f{}^2 \tan \emptyset'}{(\gamma_t h_1 + \gamma_{sat} h_2) \sin i_f \cos i_f} \qquad 2\text{-}5$$

Where, γ_t and γ_{sat} are the unsaturated and saturated bulk density of the surface soil, h_1 and h_2 are the non-saturated and saturated soil heights γ_w is the density of water and i_f is the critical slope angle for failure.

2.2 Assessments of numerical simulation models

Once a surface soil mass fails to be stable and starts to slide, its mechanical characteristics changes considerably and cannot be described by the behavior of soil masses in its stable conditions. A soil mass under sliding conditions usually will be mixed up with masses of liquids during the flowing process and even behaves like a complex fluid when the water content is large. Consequently, simulations of inundations have been applied either in a slope failure or in a fluid flow regime.

The flow behavior of landslide mass is strongly influenced by its material properties such as size distribution of geological grains (from micron scale to meter scale), grain shape and crushability, water contents, etc. There are considerable number of studies on this issue, and various constitutive models describing the detailed flow behavior have been proposed so far. However, considering the difficulty in obtaining the flow parameters of surface soils in several landslide prone areas in Ethiopia, it is reasonable to divide the analysis method into slope stability analysis to demarcate each location of slope failure vulnerable zone and to apply detail flow behavior to obtain flow inundation area using simple constitutive formulations for flow affected area.

Simplifications of constitute models appears to be a reasonable approach towards a systematic application of simulating the deposition process of debris flows. Hakuno& Uchida (1991) made a simplifications on discreet element method to analyze an aggregate of particles instead of an equation of motion formulated for each particles derived from the theoretical analysis of granular matter originated by Cundall and Otto (1979). Flow situation on irregular slopes and numerical simulations of the behavior and impact pressure when a debris flow collides with a vertical wall was also investigated by Hakuno& Uchida (1991).

Due to the complexity and constitute ranges between clays and boulders, such simplifications have limitations in fully describing the natural debris flow phenomenon. A another simplification a complex 3D problem into a 1D numerical model for unsteady flow called DAN (Dynamic ANalysis) was formulated for modelling post failures (Hungr 1995). The models has some ability to simulate actual behavior in a number of configurations and for varying material properties.

However, the model can only be used for cases where the rheology is constant and known in advance due to the model basis on a generalized rheological kernel which needs to be calibrated for a particular landslide type.

Another approach with a relatively detailed flow behavior based on depth-averaged model equations and an advanced numerical integration scheme making use of a Lagrangian representation (i.e. the grid moves with the deforming pile) was proposed by Koch et al (1994). The numerical solutions based on a Finite Difference Method (FDM) representation was found fitting with the experimental data surprisingly well with restriction of limited ability to determine time series of complete contour plots of the evolving topographies.

Several simulation code including FLO-2D solves the equations using FDM on a fixed rectangular grid. The FLO-2D computer model was developed at the Colorado State University. It is a grid-based physical process model capable calculating depth, velocities and pressures at any time on any grid-cell and its grid-based input and output structure favors to combine with a Geographical Information Systems (GIS) application. However, the application of the FLO-2D mode1 requires high quality input data, especially of a DEM and of rheological parameters of the debris flow material (Hübl and Steinwendtner 2001). Moreover, constructing a regular grid for irregular or complex geometry usually requires additional complex mathematical transformation that can be more expensive than solving the problem itself (Liu and Liu, 2003).

An extension of a Savage & Hutter theory to a 2D depth-integrated for a gravity-driven free-surface flow was proposed by Pudasaini and Hutter (2003). This formulation of depth-averaged avalanche model gave an advantage of flexibility of application and was found to be suited to realistic situations in connection with the use of Geographical Information and Visualization Systems (GIVS).

We have been developing a numerical method called depth-integrated particle method (DIPM) with a simple constitutive model (Hoang et al. 2009, Nakata and Matsushima 2014) that is able to use of the GIS from which a topographic information can be available. The model resemble with DAN analysis in the prediction of the mass movement and a definition of a typical values for mechanical parameters. When a mixture of various sizes of sediment (from clay to boulders), water and air, down a steep slope, are deformed in the presence of a gravitational field, segregation or grading of the particles can occur and particles having the same or similar properties tend to collect

together Hutter et al (1994). And hence it follows that theoretical concepts not incorporating any one of these cannot describe particle segregations.

DIPM deals with the equation of motion of soil columns as individual 'particles' that are subjected to bottom shear friction computed from modified Manning's formula and particle-to-particle interaction formulated from their hydraulic gradient. Accordingly, the material parameters governing the flow behavior are only two: the Manning's coefficient, n, and the critical slope angle, θ_{cr}. This procedure with a limited number of the material parameters governing the flow behavior made the DIPM to be capable of reproducing a natural flow phenomenon at a satisfactory level with a relatively high computational efficiency.

3 Evaluation and modification of freely available DTM

3.1 Evaluation of ALOS 30-m mesh size DTM

The accuracy of the DTM (Digital Terrain Model) considerably affects the evaluation result of debris flow inundated area. 20 years ago, DTMs having a global coverage were available in a 1km resolution like GTOPO-30 (Global Topography in 30 arc-sec) and GLOBE (The Global Land 1km- Base Elevation Project). Recently, more advanced global DTMs with better resolutions have become available free of charge, such as the Shuttle Radar Topography Mission (SRTM) (version 4, C-Band DEM of 3 arc-second, 90-m resolution) and the Advanced Spaceborne Thermal Emission and Reflection Radiometer (ASTER) (version 2, 30 m resolution) DTMs. Apart from these freely available sources, commercial DTMs with much higher resolution based on stereo-images from a number of satellites (IKONOS, SPOT, ASTER sensors) are also available.

Recently Japan Aerospace eXploration Agency (JAXA) has published the elevation data set (5-meter mesh version) of the "World 3D Topographic Data" based on the images acquired by Advanced Land Observation Satellites (ALOS) operation, and its less accurate 30-meter mesh version is freely available for the entire globe (ALOS Global Digital Surface Model, 2019).

Another freely available DTM was also derived from Google earth application by extracting elevation values using free software called TCX converter. A Keyhole Markup Language (KML) extension file of random points were collected by drawing paths on the google earth map of the research area. Then, elevation values for these random locations were found through internet

connection. The longitude and latitude values in the degree decimal were changed into Universal Transverse Mercator (UTM) meter values using zone 37 northern hemisphere used for central Ethiopia via GIS applications.

3.1.1 Spatial interpolation methods

We use interpolation methods to obtain elevation values at the desired interval values. The commercial ALOS DTM was obtained at 10 meter intervals from the providing sources. The ALOS 30-m mesh and the randomly collected google earth DTMs were changed into 10-m mesh size using natural neighbor algorithm in the Grass GIS invironment. Natural neighbor interpolation algorithm calculates the point value depending on the neighbour points. Similar to the Inverse Distnace Weighting (IDW) technique this algorithm also gives a higher weight to the nearset point and then the weight decreases as the distance increases (Ochoa et al 2019).

Equation (3-1) shows the estimation of elevation value ($Z_{x,y}$) at the point (x,y) from the elevation values of 30 meter and random intervals at the location i(x_i, y_i, z_i)

$$Z_{x,y} = \sum_{i=1}^{n} w_i \, Z(s_i) \qquad 3\text{-}1$$

Where, $Z_{x,y}$ is the estimate of the elevation at the point (x, y), w_i is a weight that determines the relative importance of point Z, $Z(s_i)$ is the measured value at the location s_i(x_i, y_i) and n is the number of points.

The two freely available DTMs namely, ALOS 30m and Google earth DTM were evaluted against the ALOS commerial source DTM. We use frequency of elevation values, the contour map for each DTM and the cross sectional sectional view along selected profiles to evalutae the DTMs.

3.1.2 Results and discusions

In order to compare the accuracy of these DTMs, we took a 10 km by 10 km region in Ankober area in the central Ethiopia as an example. It is located at the margin of the Ethiopian Main Rift (EMR) and includes the highly mountains terrains (about 3,400 m above sea level) in the west part as well as the lower lands (about 1,400 m above sea level) in the east part.

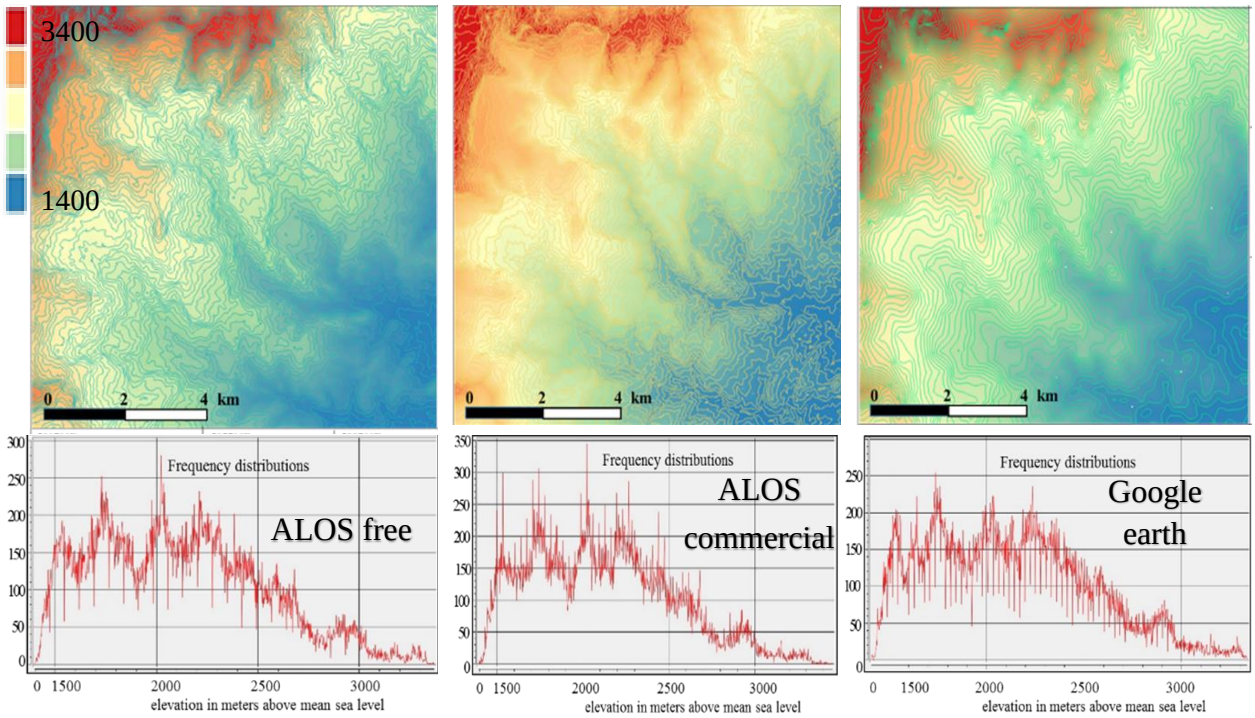

Figure 8 Contour map and frequency of the elevation values on the DTMs around Ankober area in Ethiopia.

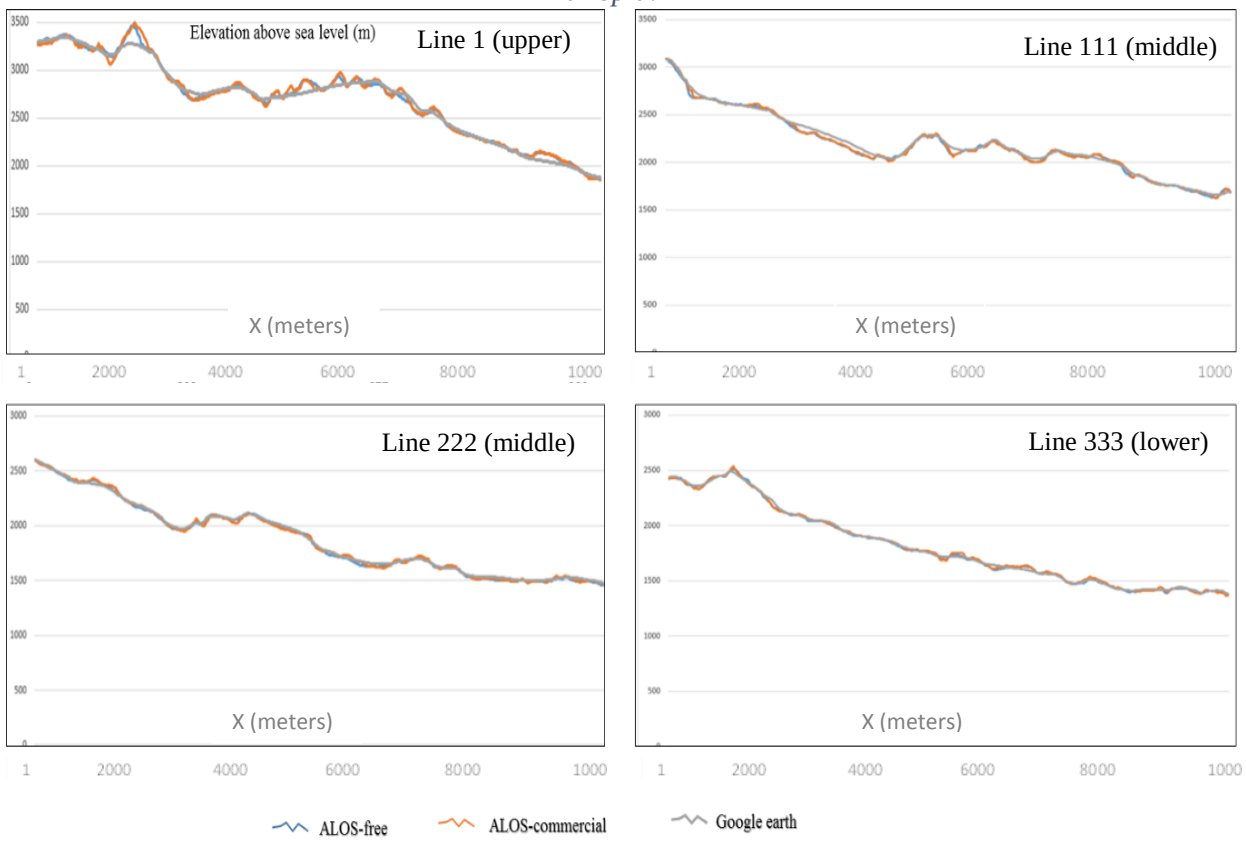

Figure 7 cross-sectional view at some selected profiles of the three digital terrain models.

Figure 8 shows the frequency and contour lines of the elevation values on the ALOS freely and commercially available as well as the google earth DTM. Figure 7 shows the cross-sectional view at some selected profiles of the three digital terrain models. There are 333 lines in the 100 square kilometer study area using 30m equal intervals. Four cross sectional views at line 1, line 111 line 222 and 333 were selected to make comparisons.

The terrain discretization and smoothening effects of a DTM is evident in frequency distributions and contour line spacing. The highly varying frequency distribution on DTM derived from the google earth application shows the effect of terrain smoothening and this causes in a loss of topographic details. It is clearly seen from the figures that the free and commercial ALOS DTMs show more or less similar values in this scale, whereas the google earth DTM whose mesh size is 30 m (same as free ALOS DTM) has much smoother topography particularly in the highland rugged places. The differences are more than 100 m in some places.

The similarity of cross-sectional views at a longer profiles shows the equivalence of the resolution of the DTM on regional level. However for a local area investigation the resolution of the DTMs need to be checked at a closer view up at some selected places. At a closer view (Figure 9) it was found that free ALOS DTM has some local flat planes probably because of the process of accuracy reduction This artefact affects the evaluation of local slope inclination from which the force acting on a numerical soil column is computed (in chapter 4). In order to avoid this effect, we adopt a simple adjacent average smoothing by adding points along the points so that the model fits a smooth function along the path. Figure 9 includes an example of the topography after smoothing, which is free from the jaggy

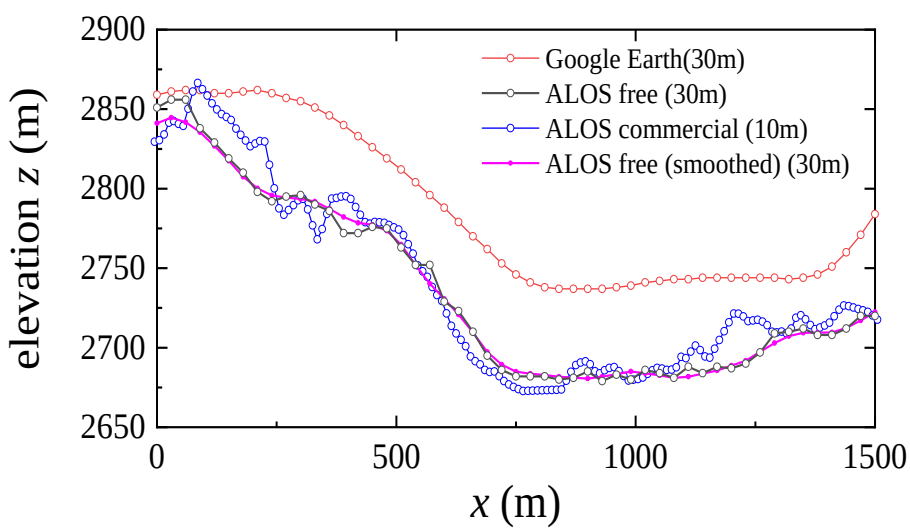

Figure 9 example of close-up data of three different DTMs and the smoothed ALOS free data in Ankober area.

artefact while, most of the important (large-scale) topographic details were preserved.

3.2 Conclusions of the evaluation of ALOS 30m DTM

We made comparison of the DTMs considering that the commercial ALOS has a better morphological representation of the study area and we made evaluation of the freely available DTMs in their topographical representation of the of the study area. From these two sources the ALOS 30m mesh was the best at representing the topography both in mountainous and in flat area. Interpolations of the DEMs down to 10 meter mesh and the reduction of the accuracy introduce a local flatness and some artefacts in the freely available sources. We made adjacent average smoothing to eliminate these problems.

3.3 Evaluation of ALOS 12.5m DTM

A relatively smaller mesh size Digital Terrain Model (DTM) at 12.5m mesh size was obtained from ALOS Phase Array type L-band Synthetic Aperture Radar (PALSAR) developed by Alaska Satellite Facility (ASF) which is part of University of Alaska Fairbanks (Alaska Satellite Facility, 2015) (Alahmadi 2018). We made evaluation of the ALOS 12.5 mesh size DTM using a high

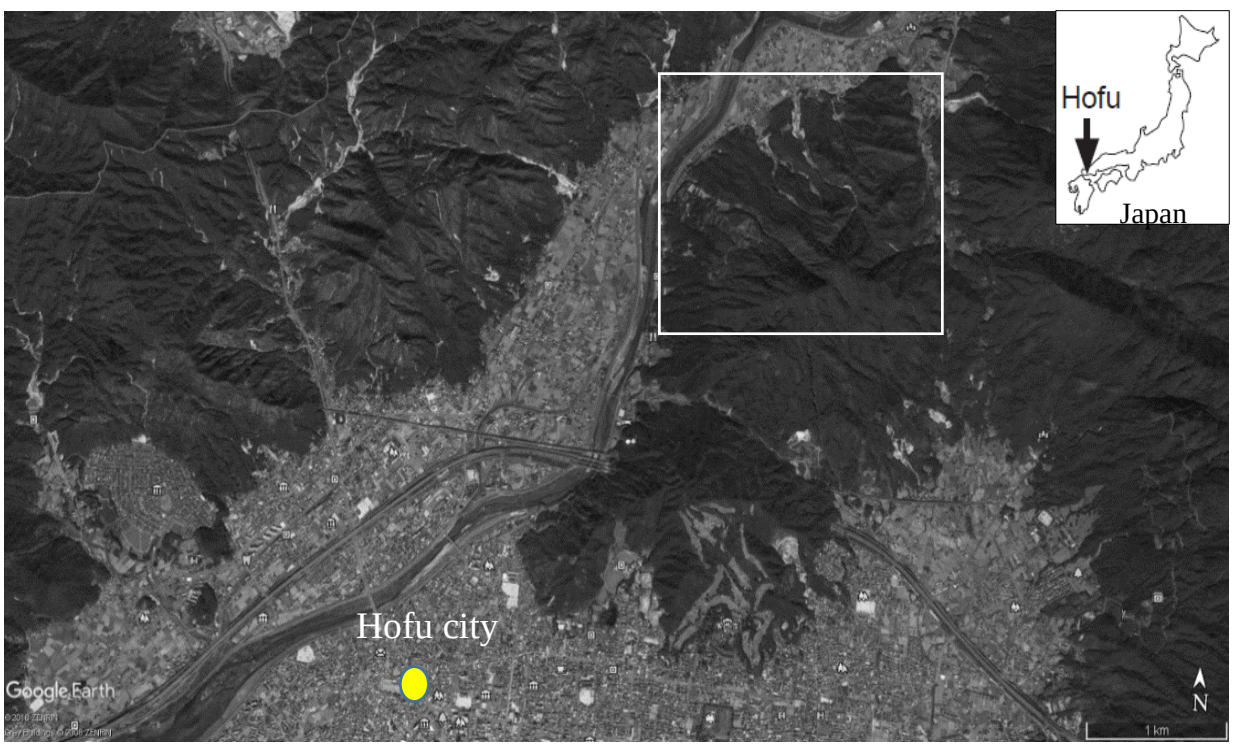

Figure 10 satellite image of ALOS 12.5-m and ALOS 30-m mesh evaluation area (white polygon) Around Hofu city, Japan.

resolution airborne survey DTM with 1m mesh size was obtained from Yamaguchi Office of River and National Highway in Chugoku Regional Development Bureau u, MLIT (Yamashita et al 2017) for the study area around Hofu city in Japan (Figure 10).

3.3.1 Evaluation of the resolution of ALOS 12.5m and ALOS 30m DTM without interpolations

Space-borne earth-observation sensors provide new perspectives in DTM generation for virtually any location on earth (Huggel et al 2008). However, the potential capability and the limitations of these sources for wide area slope disaster risk evaluations need to be evaluated. The travel distance and the delineation of the distal hazard zoning the numerical model result are strongly affected the digital representation of the drainage channel and valley cross-section of by DTM.

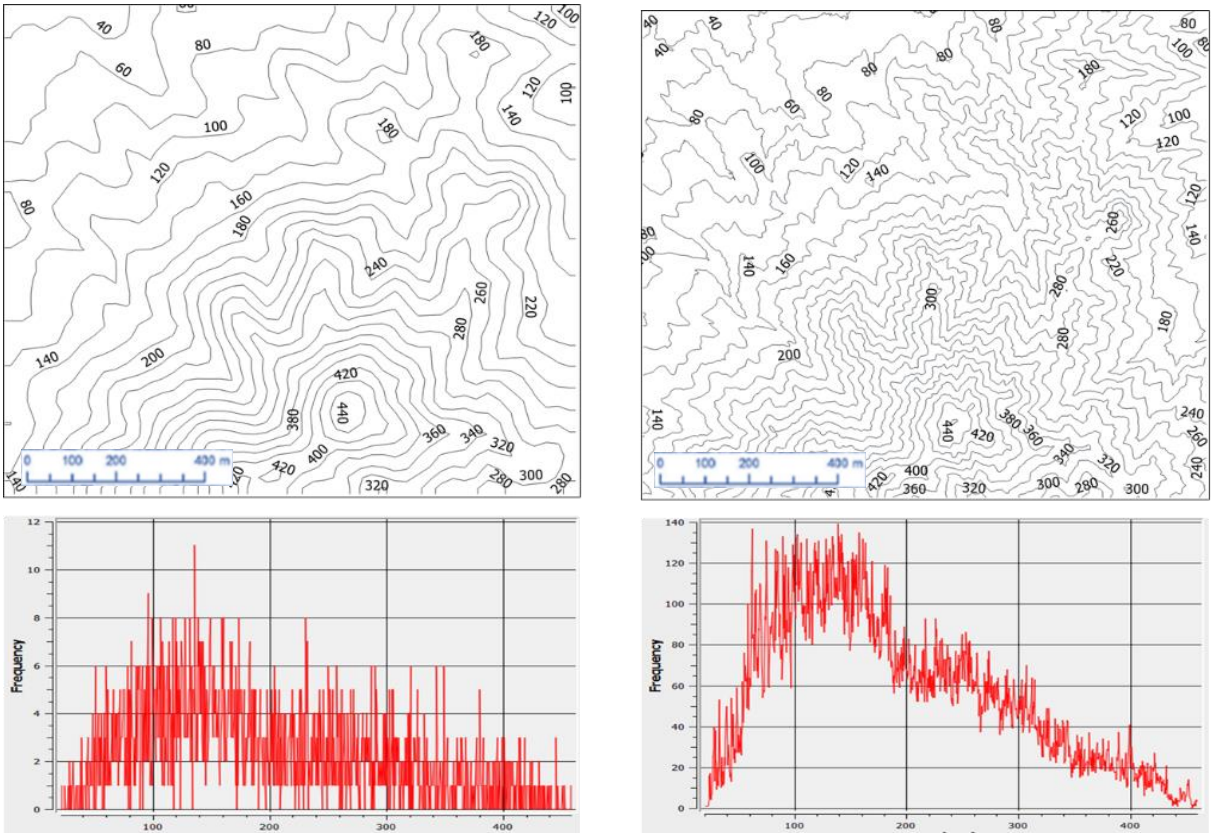

Figure 11 contour map (above) and frequency distribution (below) of the elevation values on the ALOS 30m (left) and airborne survey (right) DTMs around Hofu city in Japan.

We prepared the DTM of the study area from the three sources without making interpolations. Figure 11 and Figure 12 show the frequency and contour lines of the elevation values on the ALOS 30m and ALOS 12.5m as well as airborne surveyed 1m mesh DTM. The frequency distribution map of ALOS 12.5m mesh DTM shows a high frequency value for the values between 100 and

200 meter elevation value and then decreases as the elevation value increases which is similar to the airborne survey DTM.

The contour line distribution of the both of the freely available DTMs differ from the airborne survey DTM. The lower (40m) and higher (440m) contour value of ALOS 30-m show a similar range to the airborne survey DTM. Whereas, the ALOS 12.5m show a 20-m higher value in both lower and higher places. Next we compared using a cross-sectional view at a selected profile as shown in the Figure 11 and Figure 12.

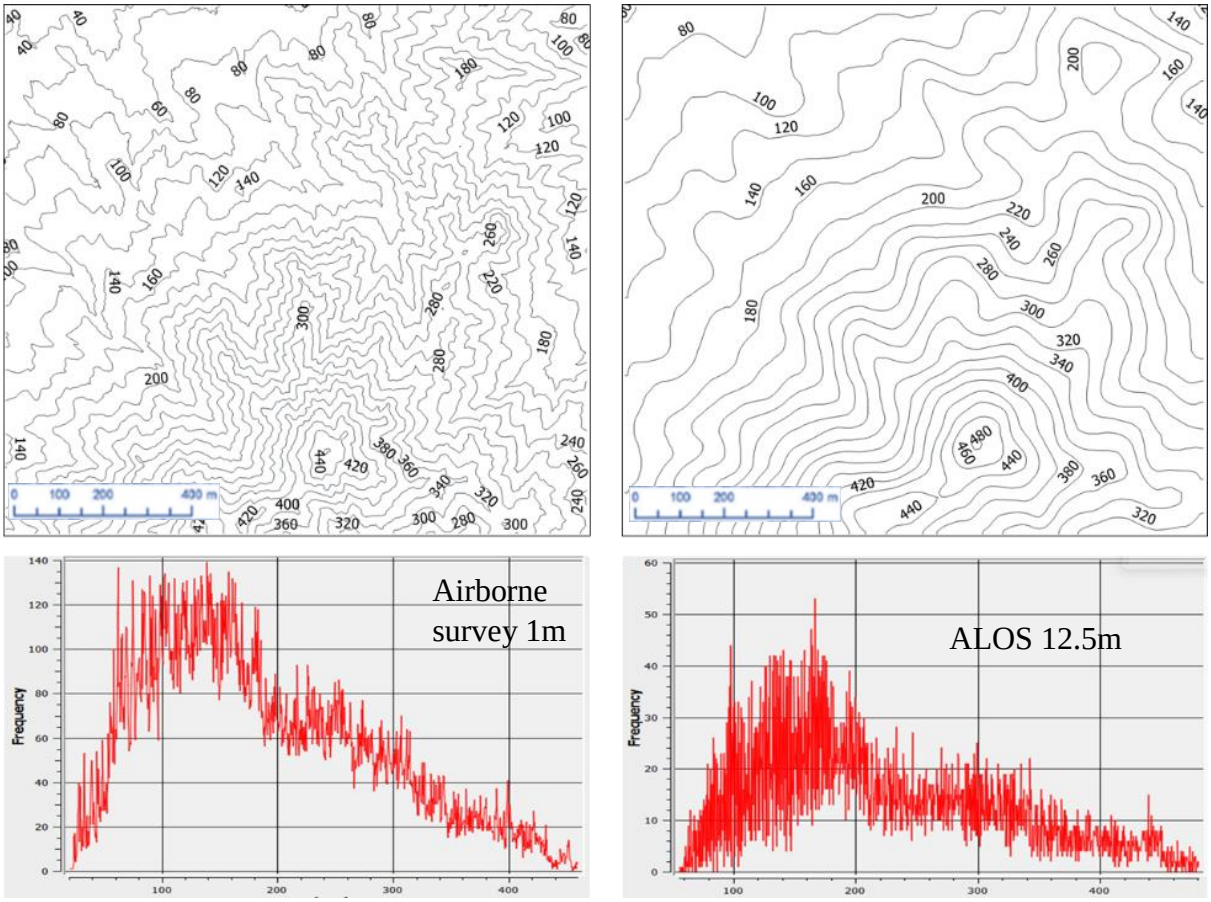

Figure 12 contour map (above) and frequency distribution (below) of the elevation values on the airborne survey (left) and ALOS 12.5m (right) DTMs around Hofu city in Japan.

ALOS 12.5m DTM showed better similarity to the airborne survey DTM compared to the ALOS 30m mesh DTM both in the medium and low elevation area. At higher altitude values ALOS 30m showed near to airborne survey DTM. We made also a comparison of the DTM from the three sources by preparing slope classes and frequency distribution map of the DTM Figure 13.

The distribution of the local slope inclination of at each location determines the computation of the force acting on a numerical soil column. The slope distribution map from airborne survey 1m mesh DTM show high value of magnitude up 76 degree slope value and depicts the morphological

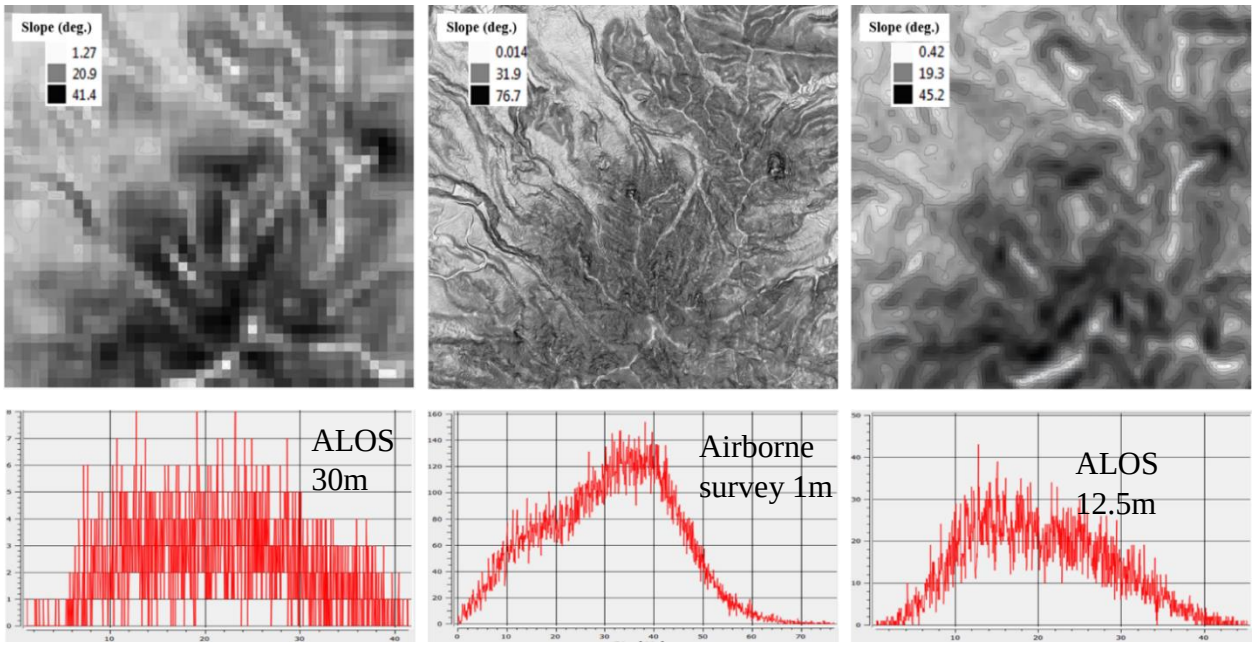

Figure 13 slope distribution map (above) and frequency distribution (below) of the slope values showing the resolution of the three different DTM.

features at a high resolution. It can be seen that ALOS 12.5m DTM showed a result close to this both in terms of the frequency distribution and slope magnitude compared to the ALOS 30m.

Figure 14 shows the cross-sectional view at some selected profiles of the three digital terrain models without making interpolations. It can be seen a similarity in the distribution of elevation values between the ALOS 12.5-m and the airborne survey DTM. Whereas the ALOS 30-m DTM differs considerably. Generally, it was found that ALOS 12.5m had shown a better improvement compared to ALOS 30m DTM.

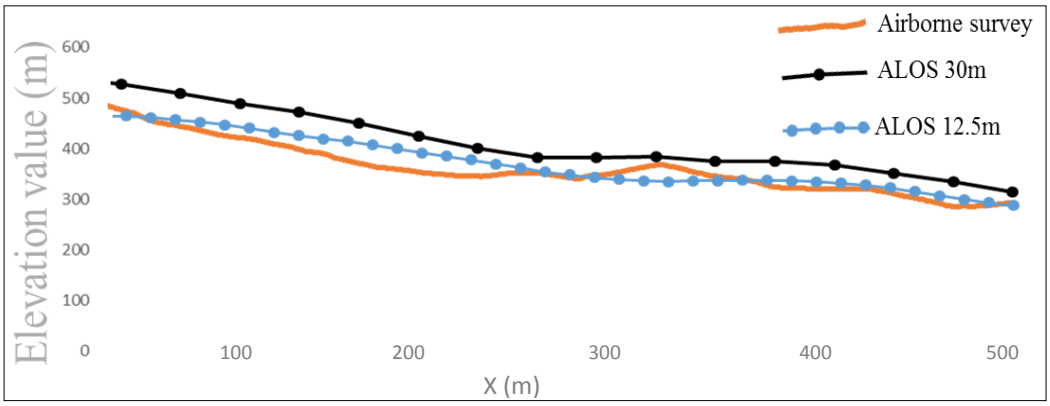

Figure 14 cross-sectional view of the three DTMs along a selected profile.

3.3.2 Evaluation of the sensitivity numerical simulations to the topographic input

Numerical models are sensitive to the resolutions of the topographic input. All other numerical parameters being equal, the rougher the resolutions, the higher the simulated momentum losses and the shorter the modelled runout distance (McDougall 2016). The accuracy of numerical simulating models depends on two factors, the nature and veracity of the flow model itself, and the accuracy of the topographic data set over which it is run (Stevens et al 2003).The effect of difference in the accuracy, quality, and spatial resolution of a DTM from different sources has not yet been investigated sufficiently. Huggel et al. (2008) compared numerical simulation results from two different remote sensing derived DTMs of 30–90 m grid size. In this section we evaluate

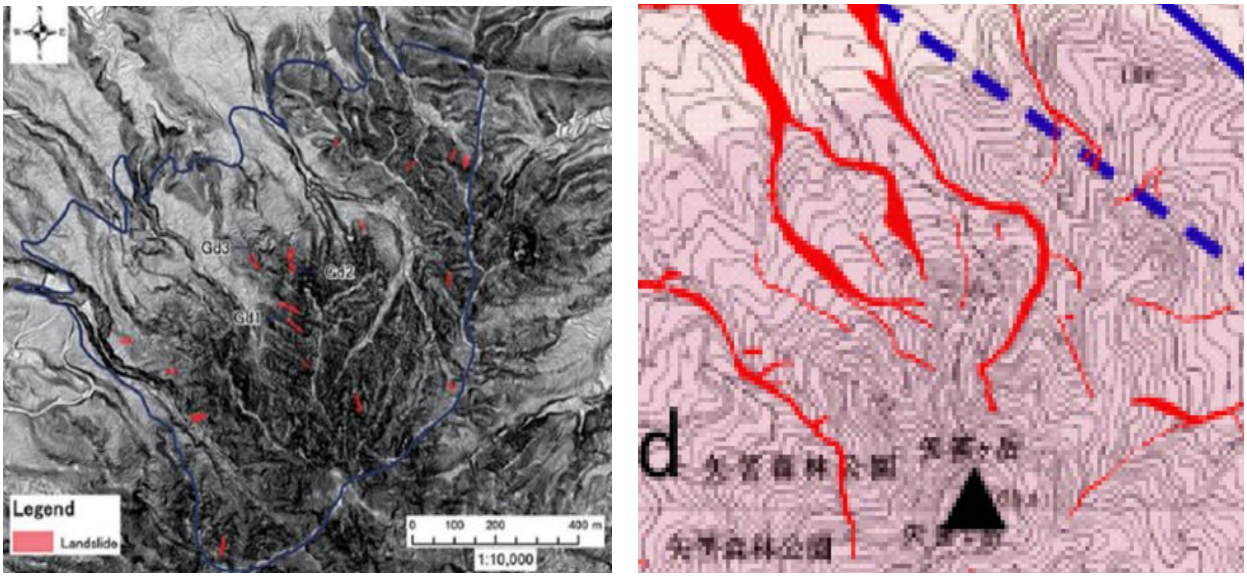

Figure 15 high resolution slope map and distribution of shallow landslides in Yahazuga-dake area from (Yamashita et al 2017) (left); distribution of the debris movement map (red polygons) from (Wakatsuki et al 2010) (right).

the effect of varying in the resolutions of the DTMs between the freely available and the airborne survey high resolution source.

In order to do the evaluation, we use a high resolution slope map and distribution of shallow landslides in the Yahazuga-dake area near by Hofu city (left side of Figure 15) obtained from Yamaguchi Office of River and National Highway in Chugoku Regional Development Bureau, MLIT (Yamashita et al 2017). And a distribution of the debris movement map (debris flow affected area) (outlined by red polygons) was obtained from interpretation of aerial photograph by (Wakatsuki et al 2010). The former show the damaged area due to shallow landslides at higher resolutions and the later display the total damaged area due to both failure of slope and mass flows inundations in a local of 1470m east west length and 1350m north-south width.

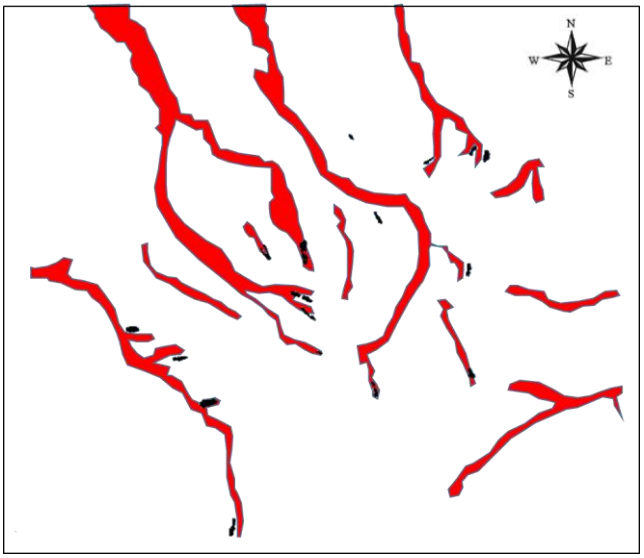

Figure 16 identified shallow landslide area (in black) and debris movement distribution map (in red).

We combine these two available maps of observed damaged area from two sources as shown in (Figure 16). The red polygons represent distribution of soil movement map and the black polygons represent detected shallow landslides areas. Interpretations of aerial photographs have been used to map geomorphological features associated with the mass movements such as scarps, counterscarps, trenches, debris flows, rock falls and debris fans (Strozzi et al 2013). Shallow landslide areas were detected from more than 1m surface lowering between DTMs in 2005 and those in 2009 (Yamashita et al 2017).

It can be seen that a substantial amount of identified shallow landslide area coincides with the initiation area of the soil movement distributions map obtained from interpretation of aerial photographs.

The two broadly different DTM with grid spacing of 12.5m (from ALOS 12.5m DTM) and a 1m mesh size high resolution DTM from airborne survey were used to make a replication of the observed affected area.

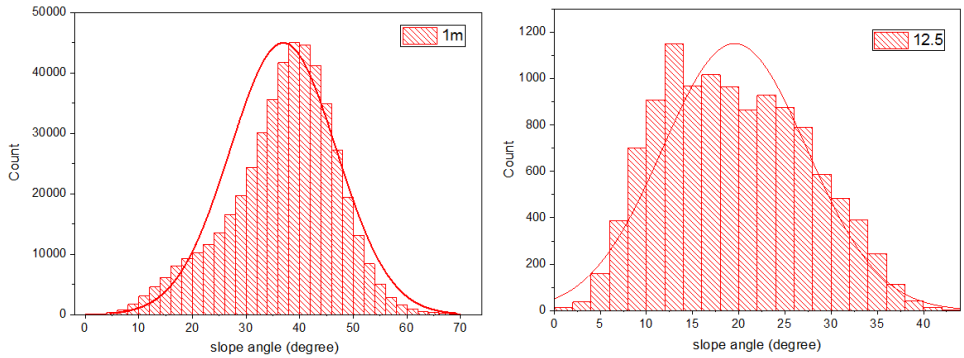

Figure 17 distribution of slope angle values obtained from 1m and 12.5m mesh size ALOS and airborne survey DTM sources.

Figure 17 shows distributions of slope angle values in the study area obtained from 1m and 12.5m mesh size DTM sources. At higher resolutions and at smaller value of the mesh size the counts of each slope angles and the magnitude of slopes in the study area remain to be higher compared to a lower resolution DTM. A higher magnitude up to 70 degree and large number of frequency distributions of each slope value can be seen in the case of a 1m mesh size compared to the a 12.5m mesh size ALOS DTM. In order to obtain a similar frequency distributions of slope angles on both DTM sources we apply a natural neighbor algorithm on both of the DTM sources to change into a 2-m meter intervals.

Figure 18 shows distributions of slope values at 2m mesh size from both the airborne survey and ALOS source. A similar frequency distributions can be seen in both cases. It can be seen also when the mesh size become at equal intervals the difference in the ranges of the magnitudes of slopes from both sources becomes narrower through an increase in the magnitude of slopes on ALOS DTM and a decrease in the values of slopes in the case of airborne survey DTM.

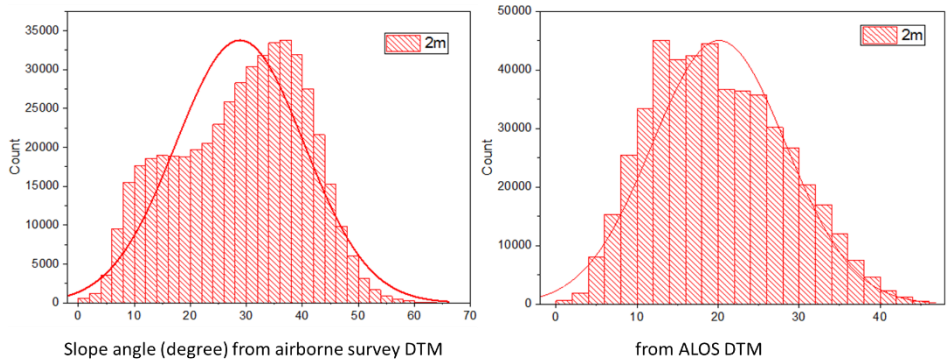

Figure 18 distributions of slope values at 2m mesh size from the airborne survey and ALOS source.

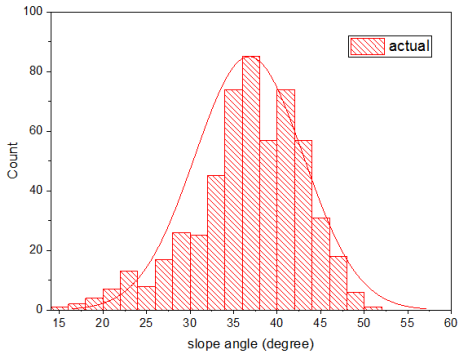

Figure 19 distribution of the slope angle values of the actual shallow landslide area shown in black dots in the figure 16 obtained using 2m mesh size airborne survey DTM.

Figure 19 shows the distribution of the slope angle values of the actual shallow landslide area shown in black dots in the figure 15 obtained using 2m mesh size airborne survey DTM. A higher frequency of values can be seen for slope angle values between 35 and 40 degree. The average value the slope angle distribution was found to be 36.78 degree which quite agree with the estimated value of 34-36 degree value obtained by Yamashita et al (2017). We used 47 degree as parameter for the numerical model to estimate the initial slope failure area on the airborne survey DTM and we used 38 and 44 degree slope angle values on the ALOS DTM.

Unlike other numerous the commercially available and noncommercial numerical simulation models that require several input parameters such as: the volume failure mass, the path profile and geometry of the sediment properties, the model employed here did not necessitate many of the input parameters obtained from the in situ records of the affected area.

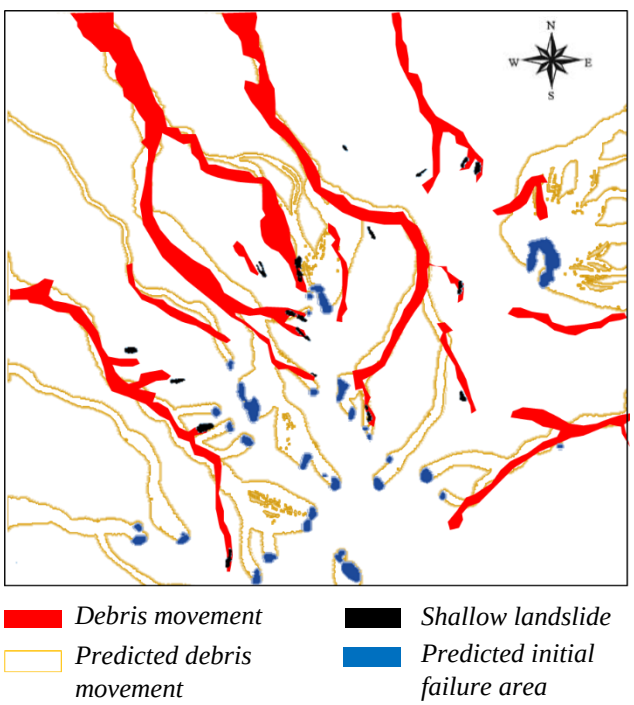

Figure 20 comparison of simulated and observed damaged area obtained from the model run using airborne survey DTM using Manning's coefficient, n=0.08, critical deposition angle, $\theta_{cr} = 3^o$ *and critical failure angle,* $\theta_f = 47^o$.

Figure 20 shows simulated result of flow area in darker yellow and the initial failure zone in blue polygons obtained using a DTM from the airborne survey. We set a manning's coefficient value of 0.08, a critical deposition angle of 3 degree and a critical slope failure angle of 47 degree.

Figure 21 shows simulated result in darker yellow and the initial failure zone in blue polygons obtained using a DTM from ALOS

12.5m source. The left side show a simulation result obtained using a manning's coefficient value of 0.08, a critical deposition angle of 3 degree and a critical slope failure angle of 38 degree. And the right side show a simulation result obtained using a manning's coefficient value of 0.13, a critical deposition angle of 3 degree and a critical slope failure angle of 44 degree.

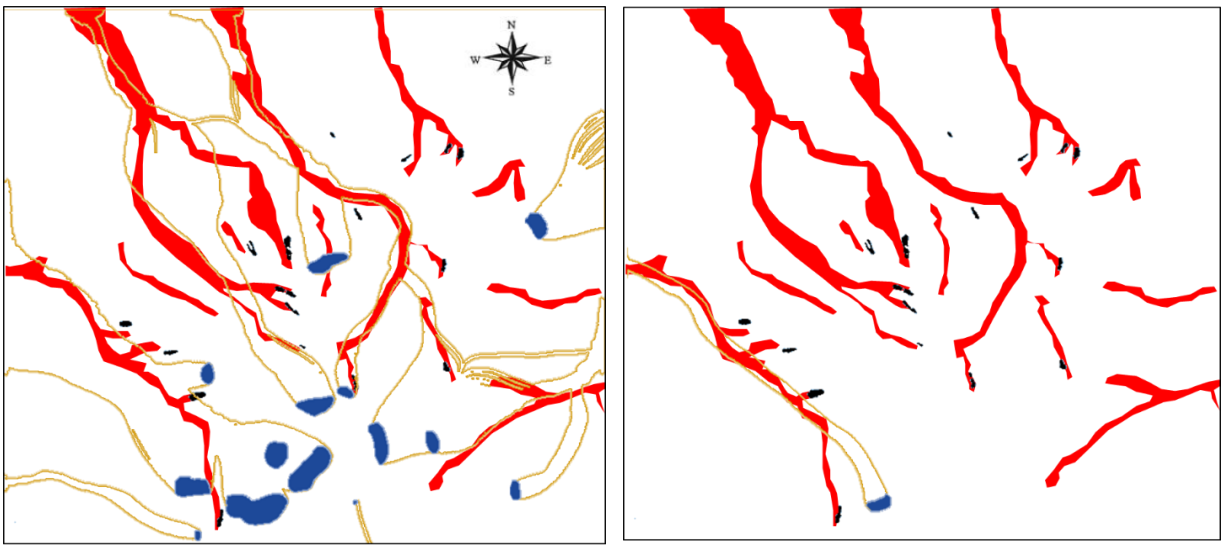

Figure 21 Simulated damaged area obtained from ALOS 12.5m source DTM. The left side show simulations based on: Manning's coefficient, n=0.08, critical deposition angle, $\theta_{cr} = 3^o$ *and critical failure angle,* $\theta_f = 38^o$. *And the right side show simulations based on: Manning's coefficient, n=0.13, critical deposition angle,* $\theta_{cr} = 3^o$ *and critical failure angle,* $\theta_f = 44^o$

The simulation results were obtained using the material parameters of the model through selection of the best match between the simulation results and the observations results of previous studies. The model is capable of reasonably reproducing the depositional patterns through calibration of the parameters using an observed inundated area from the maps of previous studies. Such capability of the model parameters to be calibrated using data from the previous studies is the elegancy of the model to be applicable in all places in the world where the sediment concentration of the debris flows and the rheology of the complete mixture may not be readily available.

Calibrations of the material parameters of the numerical model was done using the comparison of the observed and simulated results and it was found dependent on the resolutions of the DTM used to make the simulation results. In the case of using the high resolution airborne survey DTM, the material parameters values of (n=0.08, $\theta_{cr} = 3^o$) were found to be able to make a good replications of the actual event in the total area of the study area.

In the case of using ALOS 12.5m DTM, the material parameters values of (n=0.08, $\theta_{cr} = 3^o$) a critical failure angle of 38 degree were able to make a good replications of the actual event in the western and northwestern side of the study area. Whereas for the southeastern side of the area a material parameters of (n=0.13, $\theta_{cr} = 3^o$) and a critical failure angle of 44 degree was found to best fit the actual event.

It can be seen that though there is only a small overlaps between the locations of the initial failure zone of simulation result found using the model run with the DTM from airborne survey with the locations of shallow landslides identified by Watatsuki et al 2010. Moreover, it can be seen that the initial slope failure area identified by the simulation results remains in the vicinity of the locations of the shallow landslides. And most of the simulations of flow inundations quite agree with the soil movement distribution map obtained by aerial photographs. However, in the case of the result obtained by the model run using the DTM from the ALOS 12.5m source there exists a significance difference in both the location and the extent of the initial failure zones of the flows. Moreover, the flow simulations found using a manning's coefficient value of 0.08, a critical deposition angle of 3 degree and a critical slope failure angle of 38 degree show a significant deviation with observed results in the south western part of the study area. We adjusted the manning's coefficient to 0.13 and the critical failure angle to 44 degree and the result was in a better agreement with observation results.

Generally, the debris-flow affected area considered here for a comparison of the effect of DTM resolutions comprise several main and secondary surges in a total area about 2 square kilometers. The results of the model runs using the two DTMs can be compared on the basis of identifying each surge of the debris flow and on the basis of an agreement in the depositional patterns with observations. The result of the model run with airborne survey DTM covers most of the flows with appropriate bending of the channel. Whereas in the case the result obtained with the run using freely available DTM the number of surges and the pattern of deposition considerable differ. Identifying each surge and accurately capturing the curved surfaces remain crucial because of the variation of flow dynamics at such locations due to the occurrence of transverse shearing and cross-stream momentum transport when the topography obstructs or redirects the surge of debris masses. Extra longer estimation of initiation area of the flowing mass was observed on both cases.

In the case of freely available DTM most of channel are not modeled with the highest accuracy. Moreover, result of model run using freely available DTM show overestimations of flow spreading's and were not also able to correctly identify a large area of flow surges. Local artifact observed slope inclinations on ALOS 30m mesh DTM was not observed on ALOS 12.5 and hence it did not required to apply smoothening with adjacent interval points. However yet, apart wide area risk evaluations, for such a local area investigations with short runout distance debris flow and a total area having less than a one and half kilometer length and width, the freely available source DTM can be limited only to give an approximate overview about the area of inundation and can serve also as a first estimates of the areas potentially affected by mass flows. In this a local area investigation, the total run out distance until the final deposition area of the main surges were not include in the area considered here. The result found by the runs of both DTM can be improved by accounting each surges of the mass flows down until the observed deposition areas.

Though the results found using the DTM from the airborne survey was more accurate in modeling both the bending and sinuosity of channels as well as the extent and the flow dispersion spans similar to the high resolution results of shallow landslides and the distribution of the debris movement map. Yet it can be seen that errors in the representation of the topography affects the local flows and the resulting depositional pattern. The results also showed how far a detailed spatial resolution of the channel and fan topography improves the model results (Rickenmann et al 2006). Nevertheless, yet due to factors such as highly dynamic active debris-flow channels and fans or uncertainties related to landslide and debris-flow initiation conditions, it is important to emphasize that even with high resolution DEMs the model results cannot give an absolute safety in prediction of risks in such hazard events. However, the contributions the results from both cases of DTM sources, in providing a support for identifying vulnerable areas, planning measures, and taking related decisions cannot be under estimated (Stolz and Huggel 2008).

3.4 Summary of the evaluation and modification of the freely available DTM

We compared the resolutions of the ALOS 30-m, ALOS 12.5-m and the google earth freely available DTM sources against a commercial available ALOS 10-m mesh and airborne survey DTM in their performance both in the representation of a realistic way of the topography and in the ability to make a replication of actual events in the numerical simulation models. Frequency and contour lines of the elevation values and the cross-sectional view at some selected profiles

were employed to compare the resolution of the DTM in representation of the topography. Regarding ALOS 30m DTM a local flatness artifacts were found which were corrected using smoothening of adjacent nodes.

Regarding ALOS 12.5m DTM, it was seen that the terrain correction made by Alaska Satellite Facility enhanced its resolution and hence we made comparison with a high resolution airborne survey DTM in its ability in reproducing actual events using the numerical models. The results of the model runs using the two DTMs was compared on the basis of identifying each surge of the debris flow and on the basis of an agreement in the depositional patterns with observations. The result of the model run with airborne survey DTM covers most of the flows with appropriate bending of the channel. Whereas in the case the result obtained with the run using freely available DTM the number of surges and the pattern of deposition considerable differ.

The comparison was made on a selected local area about 2 square kilometers and result showed that for such a local area investigations with short runout distance of a debris flow and a total area having less than a one and half kilometer length and width, the performance this DTM can be limited only to give an approximate overview about the area of inundation and can serve also as a first estimates of the areas potentially affected by mass flows. A comparison of numerical simulation results from two different remote sensing derived DTMs of 30–90 m grid size made by Huggel et al. (2008) showed that the total travel distance of the debris flow modeled differs by as much as 15– 20% according to the DTM used.

However, for a wide areas investigation, with a deep-seated slope failure that usually happen in many places of Ethiopia, having several kilometers width and lengths, the DTM from ALOS 30-m after a correction of the local flatness and from ALOS 12.5-m without need of correction was found to be used in the evaluation of landslide risks. Wide area landslides have a longer runout distance (having several tens of meters) and they commonly travel at a higher velocity (in the order of tens m/s) hence causes severe damages (Devoli et al. 2008; Hungr et al. 2001; Pastor et al. 2008).

4 Overview of DIPM

4.1 Introductions to numerical models

Following an idealization of the physical reality of the problem with a mathematical model through sets of governing equations, there comes a need for solutions of the governing equations. Numerical solutions are important because they provide more information about solutions of the equations, particularly about a landslide intensity parameters, such as velocities and depths of the flows.

In the past, the numerical solution of the governing equations has usually been achieved by the finite difference Method (FDM), where the resulting flow patterns have been shown to correspond, within acceptable tolerances, to experimental results (Cheng 1970). In FDM approach, a continuous problem domain is discretized so that the dependent variables are considered to exist only at discrete points. Then derivatives are approximated by differences resulting in an algebraic representation of the partial differential equations (PDE), written in the strong form, using the Taylor expansion to approximate the spatial dimension of the PDEs into ordinary differential equations (ODE) in time. The ODEs can then be solved by powerful ODEs methods such as the Runge-Kutta method.

In FDM errors from the discretization, the stability conditions of the solutions and the effect of the gird size are required to be considered in order the solution obtained can be a good approximation to the exact solution of the original PDE (Imamura 1996). The accuracy of the method increases as the grid size and the time step approach to zero but by using higher order of approximations impose an increases in the computation time as well. Using large time steps helps also to increase the simulation speed in practice. However, too large time steps creates instabilities and affect the data quality (Hoffman and Frankel (2001) and Jaluria and Atluri (1994)). Although, it is possible to write most specific FDM as Petrov-Galerkin finite element methods (FEM) with some choice of local reconstruction and quadrature (Griffiths and Lorenz 1978), there is no Galerkin orthogonality, and hence convergence may be more difficult to prove. Moreover, in FDM the solution is only defined pointwise, so reconstruction at arbitrary locations is not uniquely defined.

Generally, FDM is well suited for the numerical simulation of various types of conservation laws and it can be used on arbitrary geometries using structured or unstructured meshes. Furthermore,

it can be extended to arbitrarily high order of accuracy in many ways. However, it uses a topological square network of lines to construct the discretization of the PDE. This is a potential bottleneck of the method when handling complex geometries in multiple dimensions. This issue motivated the use of an integral form of the PDEs and subsequently the development of the Finite Element Method (FEM) and finite volume Method (FVM) (Peiró et al 2005).

In a FVM, the numerical solutions of the equations are written in a form which can be solved for a given finite volume and then for every volume the governing equations are solved. The basic advantage of this method over FDM is it does not require the use of structured grids, and the effort to convert the given mesh in to structured numerical grid internally is completely avoided. However, as with FDM, the resulting approximate solution is a discrete, but unlike the FDM the variables are typically placed at the centers of each volume rather than at nodal points. Thus FVM are generally expected to provide better conservation properties but like FDM they provide discrete solutions not a continuous (up to a point) solution which can be obtained in FEM.

In FEM the computational domain is divided into smaller domains (finite elements) and the solution in each element is constructed from the basis or test functions. Then the PDE equations that are solved are obtained by restating the conservation equations in weak form by multiplying with an appropriate test functions, and then integrated over an element. Since the FEM solution is in terms of specific basis functions, a great deal of information can be known about the solution than for either FDM or FVM. Moreover the accuracy of the result can be improved by constructing meshes of the computational domain with proper sizes and shapes. However, in all the three of methods, the problem spatial domain is discretized into meshes named as elements in FEM, grids in FDM and volumes in FVM. Such discretization of the spatial domain of the problem into meshes impose difficulties in handling problems related to mesh distortions. Moreover, the construction of adequate meshes for problems with complicated boundary conditions turns to be a tough issue which limit their application for problems involving large deformations in the field of geotechnics. To surpass this problem mesh free methods have been implemented.

The mesh free methods establish a system of algebraic equations for the problem domain without the use of meshes but uses instead a set of local nodes scattered within the problem domain and its boundaries. The field functions are then approximated locally using these nodes. There are a number of mesh free methods that use such local nodes for approximations (Liu 2009). Among

them the longest established and has matured compared with other meshless methods is the smooth particle hydrodynamics (SPH). It was originally developed in the 1970s for the simulation of astrophysical phenomena (Lucy 1977; Gingold and Monaghan 1977). In this approach, the field variables such as mass, density, stress tensor, etc., are divided up into a collection of so-called "smooth particles".

Unlike Eulerian approach (fixed frame of reference) SPH is a purely based on a Lagrangian approach (moving frame of reference) in which particles carry field variables and move with the material velocity. Due to its Lagrangian formulation SPH has advantages in handling a large deformation compared to other grid-based numerical methods. And its adaptive nature allows to handle complex geometries without any difficulties.

Nevertheless, almost all of the theory in fluid dynamics is developed in Eulerian or field form. In Eulerian descriptions the frame of reference is fixed in space and the particles move with respect to the grid. Therefore remeshing procedure are avoided making this formulation suitable for fluid or large deformation solid problems. However, this formulation suffers an advective term due to a relative motion between the particles and the mesh points which introduce a numerical difficulties that requires an implementation of a suitable numerical stabilization techniques.

The Reynolds Transport Theorem had been used to transform the Eulerian description into field coordinates. This involves to deal with the material derivative that relates the time rate of the changes observed by following a moving particle $D(\ )/Dt$ to the time rate of changes observed at a fixed position $\partial(\ )/\partial t$ and the advective rate of changes in field coordinates $V \cdot \nabla(\ )$. This term represents the transport of fluid properties at a definite rate and direction and it is nonlinear which involves a product of an unknown velocity and the first partial derivative of a field variable and so the wide array of methods that are available to solve linear PDEs will not be applicable. We avoided this via replacing the continuum formulations by an interactions of particle as used in Molecular Dynamics (Alder and Wainwright 1959) and Discrete Element Method (Cundall and Strack 1979).

This simple depth-integrated particle method (DIPM) is a simplification of an SPH (Hoang et al. 2009, Nakata and Matsushima 2014, Zhang and Matsushima 2016). In this approach, the field variables are divided up into a collection of particles similar to an SPH but unlike SPH it does not suffer to require a sufficient number of particles in the smoothening domain to achieve a reasonable

accuracy of computations. Moreover, the weighted average of variables that are connected to the second order derivative of the smoothing function were not to consider here, to avoid numerical problems such as the tensile instability. In other words, we use a set of equations on a discrete system instead of the continuum equations. This approach helps a computational efficiency but it has strong dependence on the size of the particles which is a function of the mesh size of the terrain model that represent the region of interest.

The set of equations are constructed by superposition of the particles. Hence as each particle moves, it pushes on all of its neighbors, so that in areas with a denser concentration of particles, the flow depth and depth gradients will be greater and, in general, so will the spreading forces. A major advantage of this method is that the particles are free to split apart from each other to move around obstacles in the path without causing mesh distortion problems (McDougal 2016).

The model is based on the continuity and Navier-Stokes equations solve on a grid of networks obtained from the digital elevation model constructed using Grass GIS open source application software. The Grass GIS environment provides a uniform grid system to describe complex topography though a raster grid. The continuity and momentum equations are solved numerically and the soil-water mixture are considered as particles or columns moving in a Lagrangian coordination. It's suitable for the simulation a wide area risk evaluations (Nakata et al., 2014, Zhang et al, 2016). The code is written in a FORTRAN programming language and has a graphical user interface. The flowing sections shows the procedures used in the numerical method

1. Start
2. Reading topographic data
3. Step 1: generation of debris sources
4. Slope failure judgment and put particles on the slope failure position and judgment of the deposition angle
5. Step 2: simulation of debris flow
6. Use the position information of debris sources
7. Loop for each particle calculation steps
8. Loop for neighboring particles
9. Inter-particle distance judgment: if larger the maximum influence distance, go to (15)
10. Calculation of hydraulic pressure

11. Next neighboring particle: go to (8)
12. Next particle: go to (7)
13. Calculation of gravitational force and
14. Critical slope judgment and calculation of bottom shear stress
15. Sum up the total forces
16. Solve the equation of motion and obtain the next position of particles
17. Next calculation step: go to (11)
18. Repeat (7)-(16)
19. Output
20. End

It consists of 4 modules:

- Main module (reading input data file and topographic data).
- Calculation of topographic slope.
- Inter-particle distance judgment and calculation of hydraulic pressure.
- Calculation of bottom shear stress and critical deposition slope judgement.

The input data contain two categories:

- The "*.txt" files containing information about the topography. From which the gridded mesh points are generated using mesh-generator application.
- The "*.dat" files containing information about the type of the event, the control parameters of the simulation and the material properties.

4.2 Governing equations

Shallow water equations are used in computational fluids dynamics when the horizontal dimensions are much larger than the vertical length scale. SWE is obtained from depth integration of the Navier-Stokes Equations. Navier-Stokes equations can be formulated from the Lagrangian form a flow of a continuum, which can be put in vector differential equation as:

$$\frac{D\vec{v}}{Dt} = -\frac{\nabla \boldsymbol{\sigma}}{\rho} + \boldsymbol{f} \qquad 4\text{-}1$$

Where, $\bar{\boldsymbol{v}}$ is the depth-averaged flow velocity, $\boldsymbol{\sigma}(\sigma_x, \sigma_y, \sigma_z)$ is the total stress force acting on the 'particle', ρ is the density the 'particle 'assumed to be constant , **f** contains all of the body forces

per unit mass. Separating the total stress force into $\nabla \boldsymbol{P}$ and $\nabla \cdot \mathbf{T}$ terms, where $\boldsymbol{\nabla}\mathbf{P}$ is the pressure gradient and $\boldsymbol{\nabla} \cdot \mathbf{T}$ the shear stress tensor then equation (4-1) becomes the general form of the Navier–Stokes equation, which can be written as:

$$\frac{D\vec{v}}{Dt} = -\frac{\nabla \boldsymbol{p}}{\rho} - \frac{\nabla . \boldsymbol{T}}{\rho} + \boldsymbol{g} \qquad 4\text{-}2$$

Where, only gravity **(g)** has been accounted as the body force.

Changing the total derivative into $\frac{D\vec{v}}{Dt} = \frac{\partial \vec{v}}{\partial t} + \vec{v}.\nabla\vec{v}$ the full mathematical model derived from mass and momentum conservation on with the z-axis parallel to the gravity is given as:

$$\nabla \vec{v} = 0 \qquad 4\text{-}3$$

$$\rho\left(\frac{\partial \vec{v}}{\partial t} + \vec{v}\,.\ \nabla\vec{v}\right) = -\nabla \boldsymbol{p} - \nabla . \boldsymbol{T} + \rho \boldsymbol{g} \qquad 4\text{-}4$$

For real world landslides, the vertical scale is usually much smaller than the horizontal scale and the above fully three dimensional mathematical equations can be integrated along the vertical axis to derive the depth-averaged governing equations. For a one-dimensional problem, the resulting governing equations are given as:

$$\frac{\partial h}{\partial t} + \frac{\partial h\vec{v}_x}{\partial x} = 0 \qquad 4\text{-}5$$

$$\rho\left(\frac{\partial h\vec{v}_x}{\partial x} + \frac{\partial h\vec{v}_x{}^2}{\partial x} +\right) = -\frac{\partial \sigma_{xx} h}{\partial x} - \sigma_{xx}\frac{\partial z}{\partial x}\Big]_{bed} + \sigma_{zx}]_{bed} \qquad 4\text{-}6$$

$$\sigma_{\ zz}]_{bed} = \rho g_z h + \frac{D\vec{v}_z}{Dt} \qquad 4\text{-}7$$

Where h is depth subscript 'bed' denotes the stresses at the bed (i.e. the earth surface on which the landslides move), the bar denotes that the variable is averaged along the depth. From Eq. (4-6) and Eq. (4-7), as suggested by Savage and Hutter (Savage & Hutter, 1989).

4.3 Constitutive models

The mathematical equations described in the above sections cannot be used due to the stress and strain tensor is still unknown. Therefore, constitutive or rheological models relating the stress and strain tensors are needed. The position of each particle from the initiation area to the next position was determined after estimation of the balance between the gravitational force, the bottom shear stress and the hydraulic pressure gradient. Hence, the depth-integrated balance equation of shallow water equation can be written as follows (Pastor et al. 2014):

$$\frac{D\bar{\boldsymbol{v}}}{Dt} = \boldsymbol{g}\,\frac{\partial(H_o + h)y}{\partial x} + \frac{1}{\rho h}\frac{\partial(h\bar{\boldsymbol{\sigma}}^*)}{\partial x} - \frac{\boldsymbol{\tau}_b}{\rho h} \qquad 4\text{-}8$$

Where $\bar{\boldsymbol{v}}$ is the depth-averaged flow velocity of soil column, H_0 and h are the base ground and water surface heights, respectively, $\bar{\boldsymbol{\sigma}}^*$ is the depth-averaged deviatoric stress, $\boldsymbol{\tau}_b$ is the bottom shear stress.

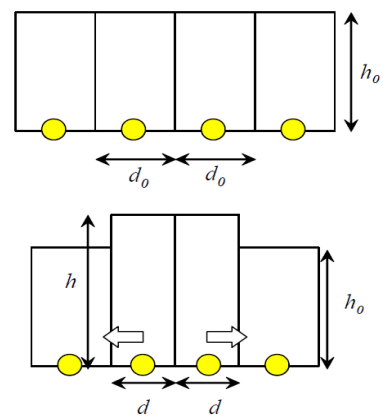

Figure 22 scheme of the hydraulic pressure.

Regarding the first term on the right hand side of Eq. (4-3), $(\partial H_0 / \partial \boldsymbol{x})$ is the base ground gradient computed from the DEM data. The hydraulic gradient $(\partial h / \partial \boldsymbol{x})$ is related to the pressure gradient as $\partial p / \partial \boldsymbol{x} = -\rho g(\partial h / \partial \boldsymbol{x})$ and stands for the force exerted per unit area on a surface of the channel due to a column of water at a given height. In open-channel flow it is used to determine whether a flow reach had gain or lost energy through the travel paths. In this study it is determined by the interaction between the neighboring particles as shown by Figure 22 It is computed by the summation of the particle-wise interaction with the neighboring particles as follows:

$$\frac{\partial \boldsymbol{P}}{\partial x} = -\rho g\frac{\partial h}{\partial x} = \rho g V_o \sum \frac{12}{\pi R^4}\frac{\boldsymbol{x_j}-\boldsymbol{x_i}}{r}\left|r - r_{eff}\right| \qquad 4\text{-}9 \qquad\qquad r = \left\|\boldsymbol{x_j}-\boldsymbol{x_i}\right\| \qquad 4\text{-}10$$

Where r_{eff} is the effective radius. This equation is derived by the quadratic smoothing function $W(r) = 6(r - r_{eff})^2 / \pi r_{eff}{}^4$ often used in SPH formulation. Since Eq. (4-10) is a linear function of particle distance r, hence it is easy to ensure the computational stability. As for the second term in eq. (4-3), we neglected the term of $\bar{\boldsymbol{\sigma}}^*$ for simplicity.

The third term in eq. (3-3), $\boldsymbol{\tau}_b$ for viscous fluid is usually computed from Manning's formula $\bar{v} = (R^{2/3} I^{1/2})/n$ combined with the equation of steady uniform flow $gI = \tau_b / \rho h$ and assuming the hydraulic radius $R = h$ as follows:

$$\boldsymbol{\tau}_b = \left(\rho g \frac{n^2}{R^{1/3}} \bar{v}^2 \right) \frac{\bar{\boldsymbol{v}}}{\|\bar{\boldsymbol{v}}\|} \qquad \text{4-11}$$

Where, $I = \partial H_0 / \partial x$ is the gradient of the base ground, and n is the Manning's roughness coefficient. The values of Manning roughness coefficient n shows a variety in the roughness of the wetted perimeter of a channel, deposition of solid particles and presence of obstructions. The values also controls the yield strength at a given channel.

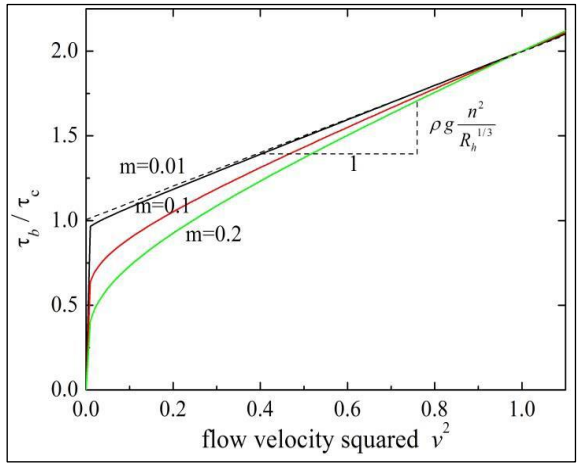

Figure 23 material response of a Bingham like fluid under a simple shear flow.

For soil-water mixture flow in this study, we adopt Bingham-like model (as shown in Figure 23) with the critical slope gradient, θ_{cr} controls the critical shear stress value required to be exceeded before any shear occurs:

$$\boldsymbol{\tau}_b = \left(\tau_{cr} \|\bar{\boldsymbol{v}}\|^m + \rho g \frac{n^2}{R^{1/3}} \|\bar{\boldsymbol{v}}\|^2 \right) \frac{\bar{\boldsymbol{v}}}{\|\bar{\boldsymbol{v}}\|} \qquad \textit{4-12}$$

$$\tau_{cr} = \rho g R \tan\theta_{cr} \qquad \textit{4-13}$$

Where m is a parameter for smoothing Bingham model, and $m = 0.01$ is adopted in this study.

4.4 Material parameters of the constitutive model

The mechanism of a slope failure and properties of the flows are complex events. Such events consists movement of a mixture of water and solid particles. Lots of rheological parameters are required to describe such a phenomenon (Sosio et al 2007). These parameters can be grouped into two categories: terrain feature and flow property parameters. The terrain feature parameters represents mainly the gradient the slopes that can be obtained from the DTM of the study area.

The gradient of the slope angle are often used as a parameter for identification of the slope failure initiation areas (Dai and Lee 2002) for the reason that the steeper the slope, the more the risk of the slope failure due to the higher shear induced by gravity. Columns of slopes with similar values to the slope angle referred as failure slope angle (θ_f) were used to locate the slope failure area. Selections of failure slope angles were made from the steepest existing slope gradients on the DTM of the area and we search for exact value of the slope unit depending on the slope failure situation of the actual event.

The deposition angel (θ_{cr}) controls the locations of the depositions funs. Flows may travel up to the termination of the flow channels and flood plains or natural or manmade obstructions might halt the flows in the middle of the canals. Deposition angles greater than 0 degree is used to represent such obstruction objects. Previous disaster surveys show that the deposition angle of debris flow ranges from 3 degrees to 15 degrees depending on the material and water contents (Hangr et al. 1984, VanDine 1985, Takahashi and Das 1992). Therefore, we can roughly evaluate these parameters even though there is no direct data for the material in the regions of interest.
In the most of the available table of the manning's coefficient values, the minimum value is 0.025 and the maximum value is 0.20. *Table 1* shows the typical values of n for various environments.

Table 1 Manning's roughness coefficients for common materials. (Adopted from www.engineeringtoolbox.com/mannings-roughness)

surface Materials	Earth channels				Flood plains			
	cobbles	weedy	gravelly	clean	farmland	Light brush	Heavy brush	trees
Manning's (n)	0.035	0.030	0.025	0.022	0.035	0.050	0.075	0.15

5 Validation of the model using case study areas in Japan

How to calibrate the rheological parameters required to describe the mechanism of a slope failure and properties of the flows used in the numerical models had been a challenge in the past two decades. The question is that, how do we validate the input parameter values and use them in several wide area slope disaster risk evaluations?

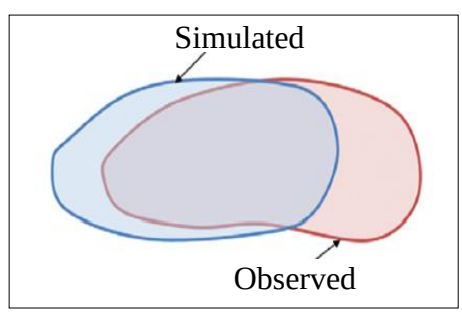

Figure 24 calibration method proposed by Galas et al. (2007)

According to the opinion of this author, this is needs to be a research focus for scientists and practitioners in this area of studies.

A simple calibration method (Figure 24) proposed by Galas et al (2007) was based on maximization of the ration of intersection (purple area) and union (blue + red +purple areas) of simulated and observed inundation areas. A perfect fit would correspond to a ratio of 1 (McDougall 2016).

Table 2 modified version of calibration of parameters using ratio between intersection and union of simulated and observed affected area

$\beta = \frac{a}{a+b}$ $\alpha = \frac{a+d}{a+b+c+d}$		**Simulation**	
		Unsafe	safe
Observation	unsafe	a	b
	safe	c	d

A modified version of this this method (Table 2) was employed to compare between the observed and predicted initiation area using visible scarps from satellite images for the case study in Ethiopia (the Debre Sina landslide area) where a relatedly extensive extent deep seated failure of slopes occurred.

The comparison was made using indices (β and α) to estimate the the ratios beween the simulated and observed safe and (unsafe) failure area separately. Another alternative approach is to calibrate the input parameter values based on a physical properties of the material using values directly measured in the field works or in a laboratory experimentations (Iverson and David 2014). This approach is appropriate to assess the velocity of real landslides. However it requires a complex constitutive relationships with quite enormous input parameters and it needs use of material sampling and testing procedures that incur a significant challenge to be applicable in areas in which detailed field works are difficult to do in the areas of every landslide occurrences. Moreover, for a wide-area risk evaluation of landslide hazards, it is not a sophisticated and accurate constitutive models that are desired, rather a primitive ones with the smallest number of material parameters that can be easily identified will benefit a lot.

We employed an alternative approach, which has been adopted in the majority of previous studies, to base on selected numerical parameter on calibrated values obtained through numerical analysis of past landslides. The calibration was done on the comparison of the agreement between the simulation and observation on the basis of identifying the initiation and deposition fan of each

surge of the debris flow in the study area. This approach is appelicable for a model with unsophisticated rheological parametrs but adequately capablity of simulating the bulk behaviour of inundation and the distribution of deposits, which is the main goal in a wide-area risk evaluations. In some cases, this approach may also have convenience and cost effectiveness in practice because specialized material testing is not required (McDougall 2016).

Moreover, models that are calibrated in one case study area can also be potentially well-suited to another area with a similar geotechnical conditions. There are several ranges of simple rheological models that can be used for this purpose. In these models calibration is done by comparing the simulation results with observations through adjusting the parameter values by trial-and-error to achieve a satisfactory match in terms of the simulated runout distance, deposit distribution, and velocities (Hungr 1995). Such an approach will be typically simple when the model has few adjustable parameters that dominate different characteristics of the simulation and can therefore be adjusted relatively independently of each other.

Depth integrated particle method model has only two material parameters: The deposition angel (θ_{cr}) which governs the slope angle on which material begins to deposit and the Manning's coefficient (n) that can be calibrated to achieve a satisfactory visual match with the observed inundated area. In the following sections we will demonstrate the calibration of these material parameters of model using well documented events in selected case study areas in Japan.

5.1 Case study 1: Calibration of the material parameters for the shallow landslide affected area around Hofu city, in Japan

A calibration of the material parameters of the numerical was done using a case study area considered in the section 3.2.2 but here, using a wider region of the affected area which includes the deposition fan of the main surges down up to the final places as shown in the Figure 25. The geology of the area is characterized by granodiorites and the vegetation cover of these areas is mainly Japanese red pine with ferns densely cover in some parts of the areas (Yamashita et al 2017).

We prepare 5 meter mesh size DTM from data obtained at 1m interval using airborne survey. A natural neighborhood algorithm interpolation technique in Grass GIS environment was employed to obtain elevation values at 5 meter intervals. A wide area extending 2.85 kilometers east-west and 2.5 kilometers north south directions was considered to make the numerical method

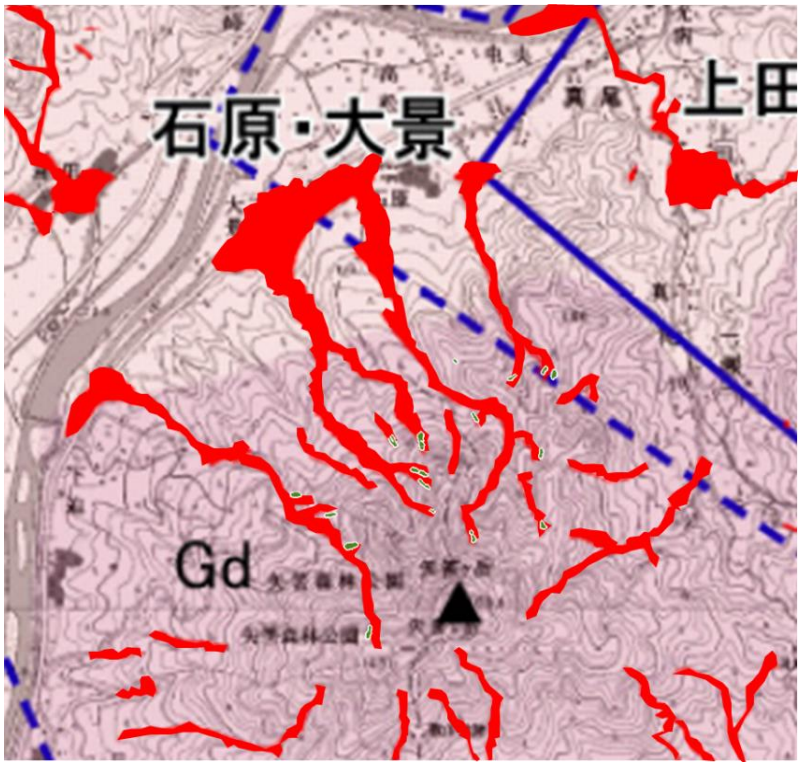

Figure 25 soil movement distribution map (red polygons) from (Wakatsuki et al 2010) overlaid with shallow landslides identified by (Yamashita et al 2017) (in green polygons) around Hofu city.

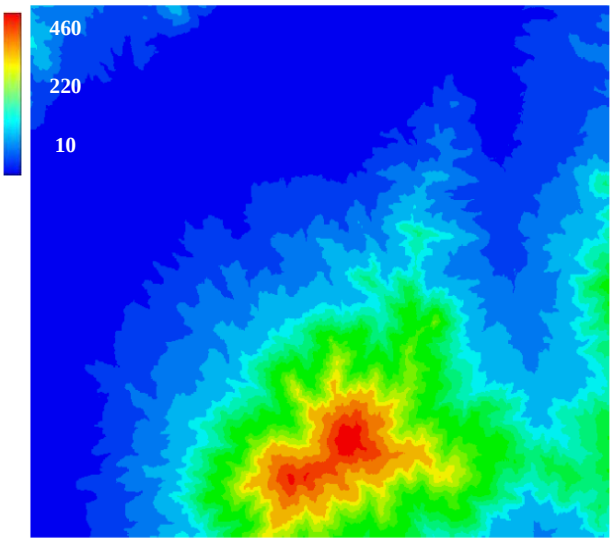

Figure 26 digital terrain model of shallow landslide affected area after interpolation to 5m mesh from 1m interval data obtained through airborne survey.

investigations. We apply a natural neighbor algorithm on 1m airborne survey sources to find elevation values at 5m meter intervals.

Figure 26 shows the DTM of the area. The map shows morphological trends with high elevation around 460m in the southern peripheries and decreases down to about 10m above sea level in the northern side.

The accuracy of the match in both the scale and location of the soil movement and the DTM map was verified by comparing the slope and the contour map of the DTM with the soil movement distribution map as shown in the Figure 27. These maps helps to look at morphological features such as drainage channels at high resolution level which helps to verify the precision of the location and size of area before making the comparisons to calibrate the material parameters.

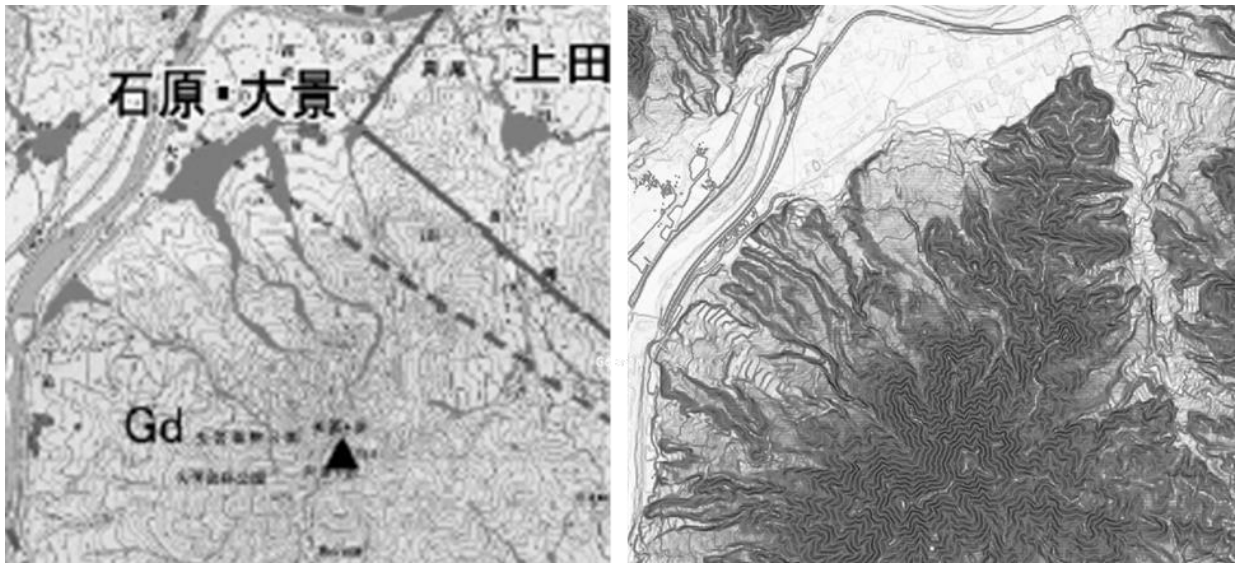

Figure 27 comparison of identified morphological features in the soil movement distribution map (left) in the slope and contour map of the DTM used in the simulation result (right).

5.1.1 Estimation of the critical slope gradient for dry and saturated soil in the study area.

Before making the prediction of slope failure location we made evaluation of the stability condition of the area using the available records. The critical slope gradient of natural and saturated soil was estimated using a simplified version 1D slope formula as shown in equation 5-1 and 5-2 using a scheme shown in Figure 28.

$$Fs = \frac{c+\gamma_{t1}h_1 \cos\theta \tan\varphi}{\gamma_{t1}h_1 \sin\theta} \qquad \text{Unsaturated} \qquad 5\text{-}1$$

$$Fs = \frac{c'+(\gamma_{t2}-\gamma_w)h_2 \cos\theta \tan\varphi'}{\gamma_{t2}h_2 \sin\theta} \qquad \text{Saturated} \qquad 5\text{-}2$$

where, θ is the slope angle, h_1 and h_2 are the failure depth and the depth of ground water ($h_1 < h_2$), respectively, γ_{t1} and γ_{t2} are the unsaturated and saturated bulk density of the surface soil, γ_w =1.0 (g/cm^3) is the unit weight of water, c' and φ are the cohesion and the internal friction angle of surface soil, respectively, in terms of effective stress.

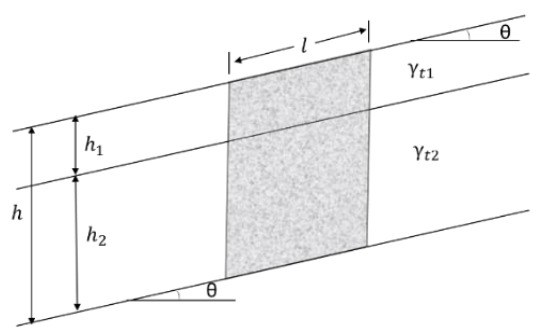

Figure 28 scheme of simplified 1D slope stability safety factor assessment.

Using the data describing in Yamashita et al 2017 (soil particle density =2.66 (g/cm^3), internal friction angle of natural and saturated soil, φ =46.7° and 44.5°, cohesion of natural and saturated soil , c' =8.31 (kPa) , c' =4.55 (kPa), dry and saturated unit volume weight, γ_{t1}=12.53 (kN/m^3) and 17.62 (kN/m^3), unit volume weight of water, γ_w =9.8 (kN/m^3) and the void ratio=1.08. Assuming h =*5.0(m)*, the slope inclination corresponding to is θ_f=36.29 (deg.) for h_1=0(m) (fully saturated), and θ_f=59.57 (deg.) (fully unsaturated). However, in the DSM obtained from data using airborne survey, the ratio of the number of meshes whose slope angle is more than 49.57(deg.) was found to be less than 0.1%.

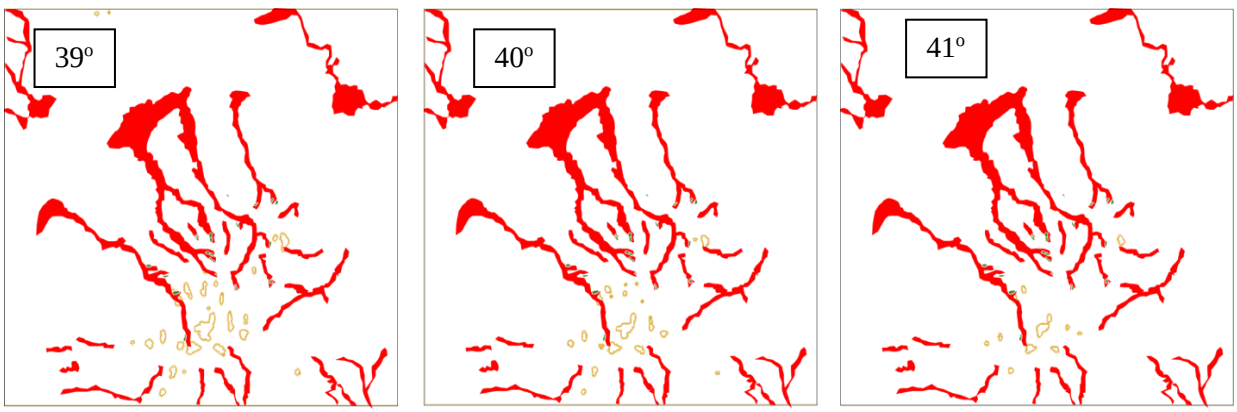

Figure 29 subjective visual comparison between predicted slope failure only by slope angle (outlined by dark yellow) and the initiation area of each surge obtained from the combination of the maps obtained by (Wakatsuki et al 2010 and Yamashita et al 2017)

Figure 29 shows the location of meshes whose slope angle θ_f exceeds (39, 40 and 41 degree) in yellowish gray. The correspondence between predicted failure slope only by slope angle (dark yellow area) and the initiation area of each surge from the combination of the two sources are not very good, possibly because of the effect of heterogeneous groundwater paths and /or heterogeneity of geomaterials.

5.1.2 Simulating surface flows of a uniformly distributed particles over the entire ranges of the region for the Hofu case study area

Before the calibration of the material parameters of the numerical model, we made a simulation the flows of a uniformly distributed raindrops in 10 mesh size intervals all over the study area. Figure 30 shows the distribution of the number of particles passing in the respective location of the study area using a threshold value of 5 number of meshes. Gray shades indicate greater number

of raindrops passing in that location which can be interpreted as a greater potential for soil saturation or a passage of stream channel in that area. Yellowish gray polygons show location of meshes whose slope angle exceeds 40 degree. It can be seen that all the stream channels identified as having a greater potential of soil saturation were not inundated by the debris flow event. But all the debris flow affected derange channels coincide with identified stream channels by the simulation result.

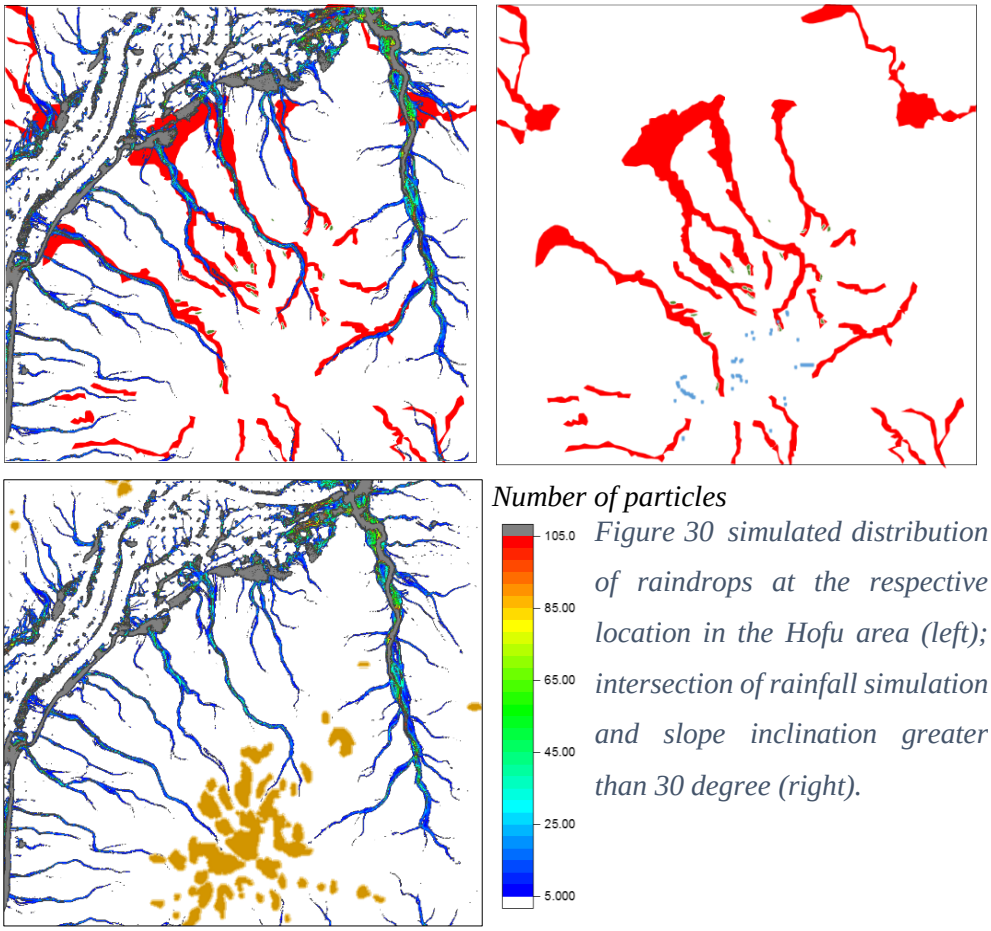

Figure 30 simulated distribution of raindrops at the respective location in the Hofu area (left); intersection of rainfall simulation and slope inclination greater than 30 degree (right).

It can be seen that the simulation result showed a similar sinuosity of the streams and pattern of deposition fan with the actual affected area obtained by interpretation of aerial photographs and those shallow landslides identified by Yamashita et al 2017.

A strong correspondence can be seen also between this simulation results with the deposition fan of the main debris flows surges in the study area. However the correspondence between this simulations results with the shallow landslide affected area identified by Yamashita et al (outlined by green polygon) and the initial slope failure area identified by slope inclination of 40 degree are not very good.

The precipitation simulation result also show a difference between the eastern and western part in that there were some stream channels of the eastern side in which a debris flow inundations were not observed compared to the northwestern and western side of the study area. This can be an indication of the difference in the material properties of the soil mass in the western and eastern side of the study area.

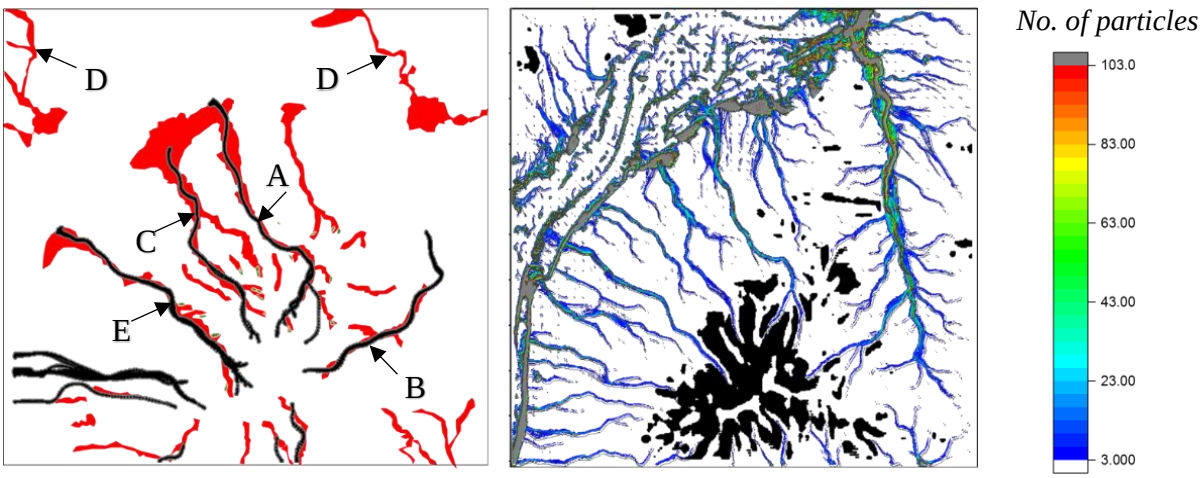

Figure 31 simulated damaged area in black using initial slope failure area obtained by intersection of the rainfall simulation with threshold value 3 particles and slope failure angle of 30 degree. Using model run with the Manning's coefficient, n=0.04, critical deposition angle, $\theta_{cr} = 5^o$

Figure 31 shows the simulation result in black and the actual damaged area in red in the left side of the figure using the initial slope failure area obtained by intersection of the rainfall simulation with threshold value 3 particles and slope failure angle of 30 degree shown in the right side the figure. The comparison of the initial slope failure area obtained from Yamashita et al 2017 shown in green polygons and the result found using the intersection of the rainfall simulation and the slope failure angle did not exactly match. However it can be seen that the simulation result had an appropriate initial slope failure area for debris flow surges marked by A, B and C as well as E. We made a detail comparison of the initial slope failure area of these surges using several slope failure angles in order to calibrate the material parameters of the numerical model.

5.1.3 Calibration of the material parameters of the model

Before the calibration the flow parameters of the initial slope failure area is required to be identified. However a user defined assignment of the initial slope failure locations becomes

difficult due to the debris flow event involved quite large number of surges. Therefore, delineation of initial slope failure area was done using critical slope failure angle. We made a sensitivity analysis using some critical slope failure angle values shown in the Figure 32 and Figure 33.

Similar to the results found from the precipitation simulations it can be seen from the two figures mention above that a critical failure angle of 40 and 41 degree were able to make a good replications for main debris flow surges and interments for the debris flow surges marked by A and B. But these predictions of the slope failure estimations incur extra area for the debris flow surge marked by E.

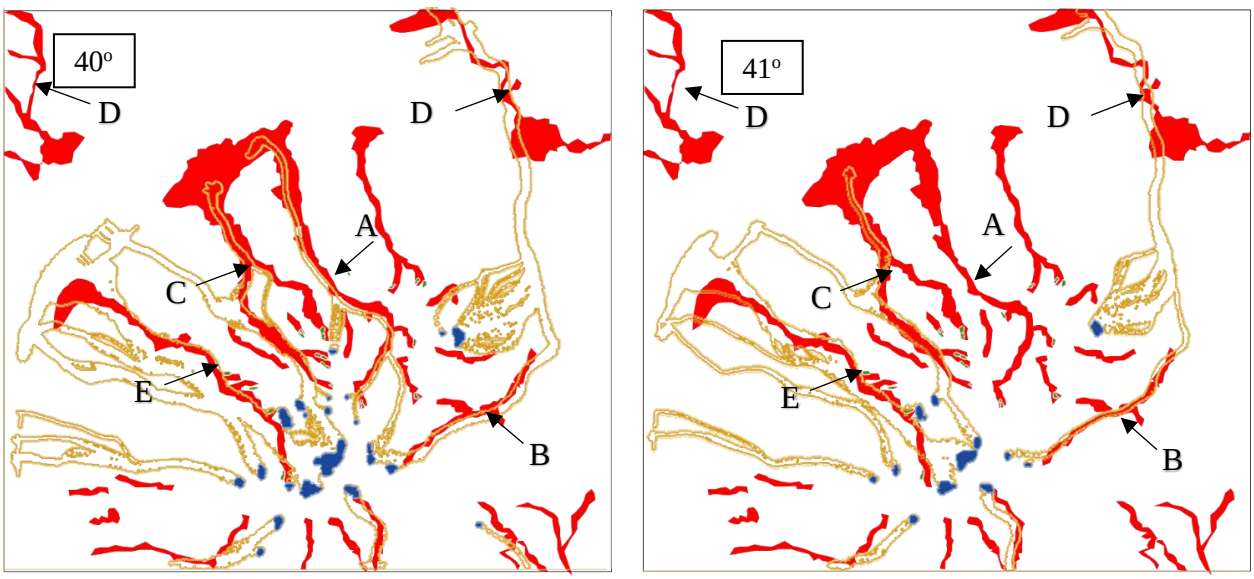

Figure 32 simulated inundation area (in dark yellow) and initial slope failure area (in blue-black) for ($\theta_f = 40$ and 41 deg.).

Whereas the initial slope failure area predicted by a critical failure angles of 42 and 43 degree was found to match the initiation of the surges of the actual debris flow event for the debris flow surge marked by E. However, these prediction were unable to reproduce the all the initiation area of the surges of the debris flow event for surges marked by A and B. Therefore, we divide the calibration of the material parameters (n and θ_{cr}) for the study area into two parts, separately. We use the initiation area predicted using slope inclination value of 40 degree for A and B and 42 degree for E.

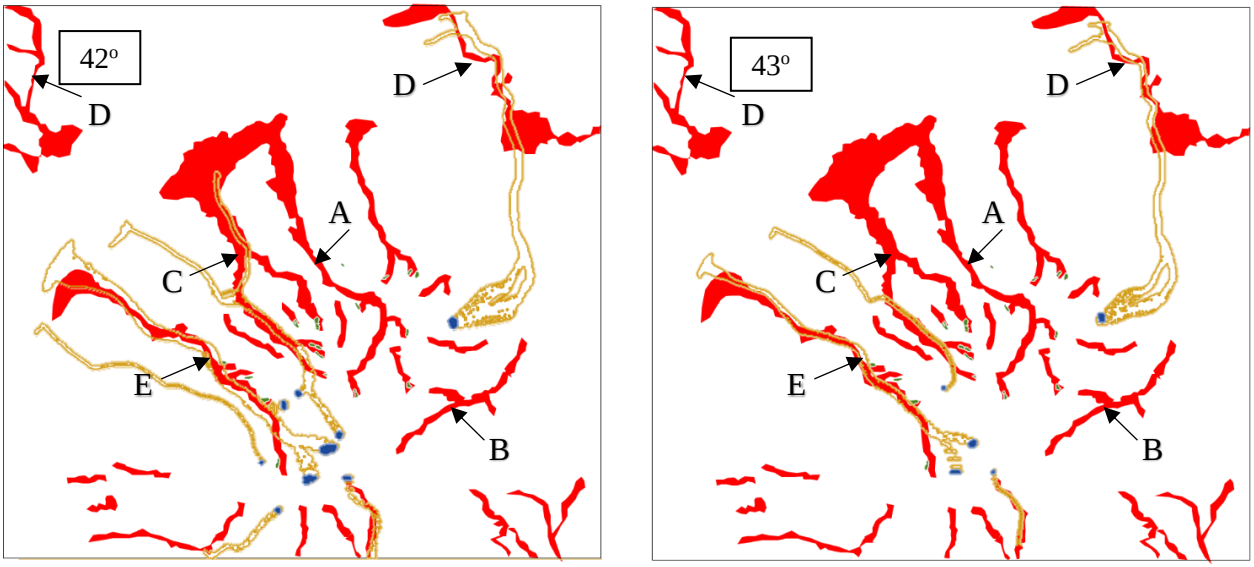

Figure 33 simulated inundation area (in dark yellow) and initial slope failure area (in blue-black) for ($\theta_f = 42$ and 43 deg.).

Our focus of the calibration is based a visual comparison of the main external aspects of landslide behavior such as how far do they travel and how wide do the flow spread in the deposition fan. Here, the landslide mass is treated as an "equivalent fluid" and the debris flow material of each surge is assumed to be governed by simple constitutive relationships with a limited number of adjustable parameters (Hungr 1995). Though this approach is subjective, it is simple to implement when the model contains few adjustable parameters that dominate different characteristics of the simulation which can be adjusted relatively independently of each other. Such a visual comparison approach tends to require more interpretations using a series of model calibration runs.

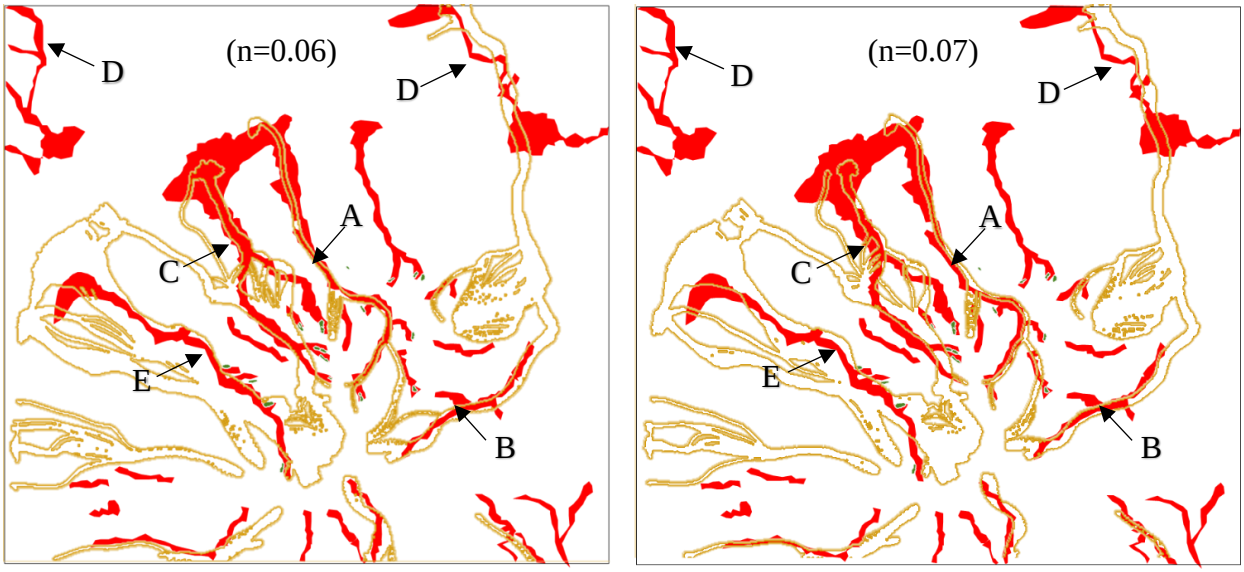

Figure 34 subjective visual comparison of the sensitivity to the Manning's value (n) of the simulation result using comparison between the simulated and observed inundation area for (n=0.06 and 0.07 and θ_{cr}= 0.5 deg.). A critical slope angle value of 40 degree was used to predict the initiation area in the western part the study area.

First we made calibration of the Manning's coefficient (n) value for debris flow surges marked by A and B in the Figure 34 shown above. For these two debris flow surges the initiation area of slope failure area was predicted relatively correctly using slope inclination angle of 40 degree. Moreover, both the initial slope failure and final deposition of these debris flow lays in the study area.

For the cases other two main surges (marked as C and D), it can be seen that, the predicted flow of in the flow path marked as C comes from the initiation area match larger than actual slope failure area identified by both debris movement distribution map (Watatsuki et al 2010) and (Yamashita et al 2017). As to the debris flow surges marked by D (in both eastern and western side of the study area) it can be seen from the Figure 35 that the initiation area of these flows happens to be out the study area considered for the numerical method analysis. It can be seen also that the deposition fan of the smaller debris flow surges in the southern peripheries of the study area remains to be out the of the study area considered for the numerical analyses.

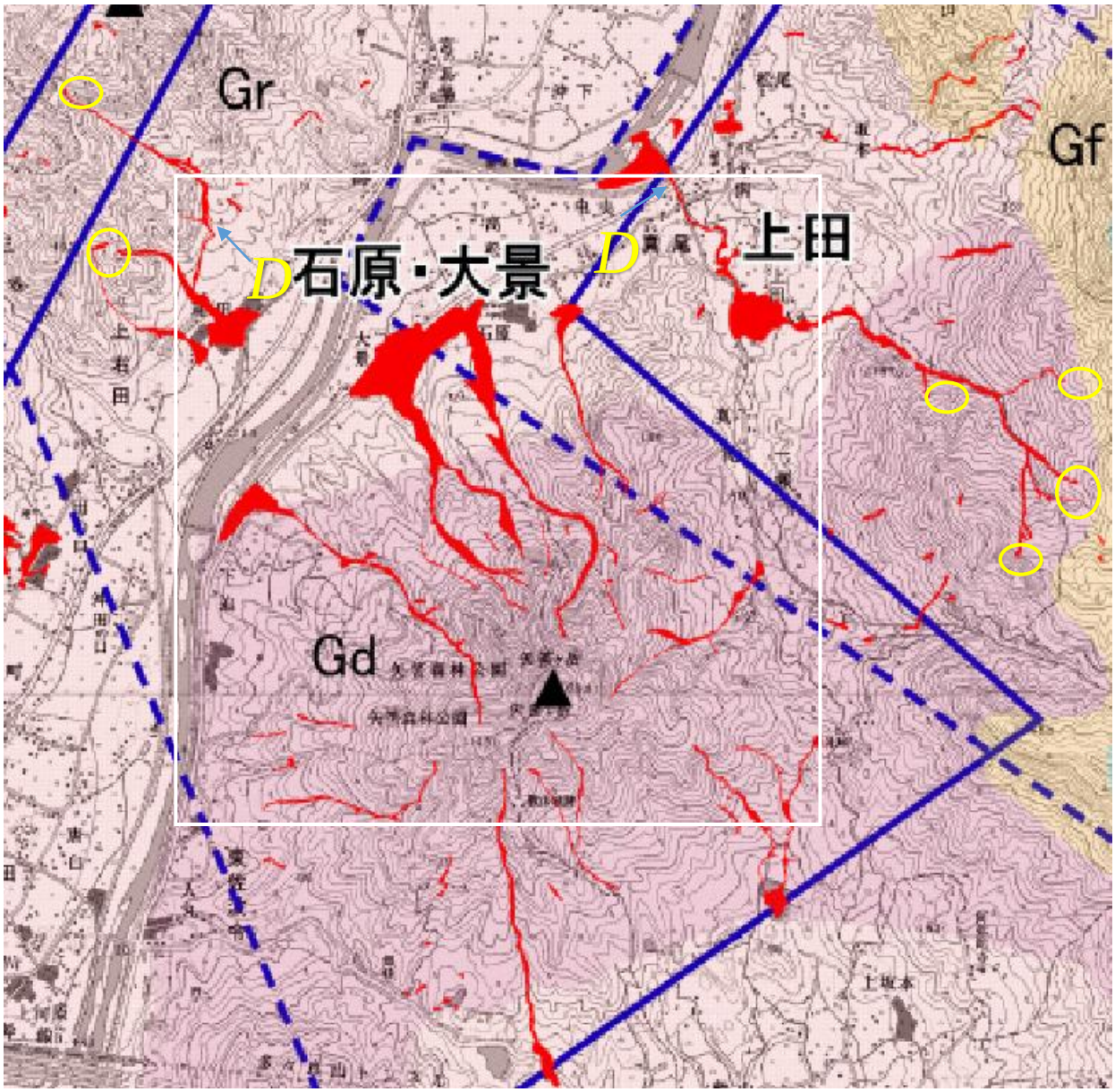

Figure 35 initial slope failure areas of the debris flow surges marked by D obtained from the soil movement distribution map. The area considered for the numerical method analysis is outline by white polygon.

The travel path and width in the deposition fan predicted (shown in Figure 34 above) by (n=0.06 and 0.07 and θcr = 0.5) for the debris flow surge marked A can be seen to be narrower both in the initiation area and the deposition fans. Whereas for the case of the surge marked by B it can be seen that the predicted result is similar to the actual event identified by the researchers mentioned in the previous sections. Therefore, this simulation produces much narrower (lateral) width for the case of the surge A and wider width for surge B. It can be seen that the model results are sensitive

to both the initial mass discharge and the resistive characteristics of each flow channel (characterized here by selection of θ_f and n values). This effect appears to be depend on the site-specific field topography (Rickenmann et al 2006). In order to see the sensitivity of the value n, we also consider lower n values (0.03) and greater (0.08) than the values mentioned above shown in Figure 36 below.

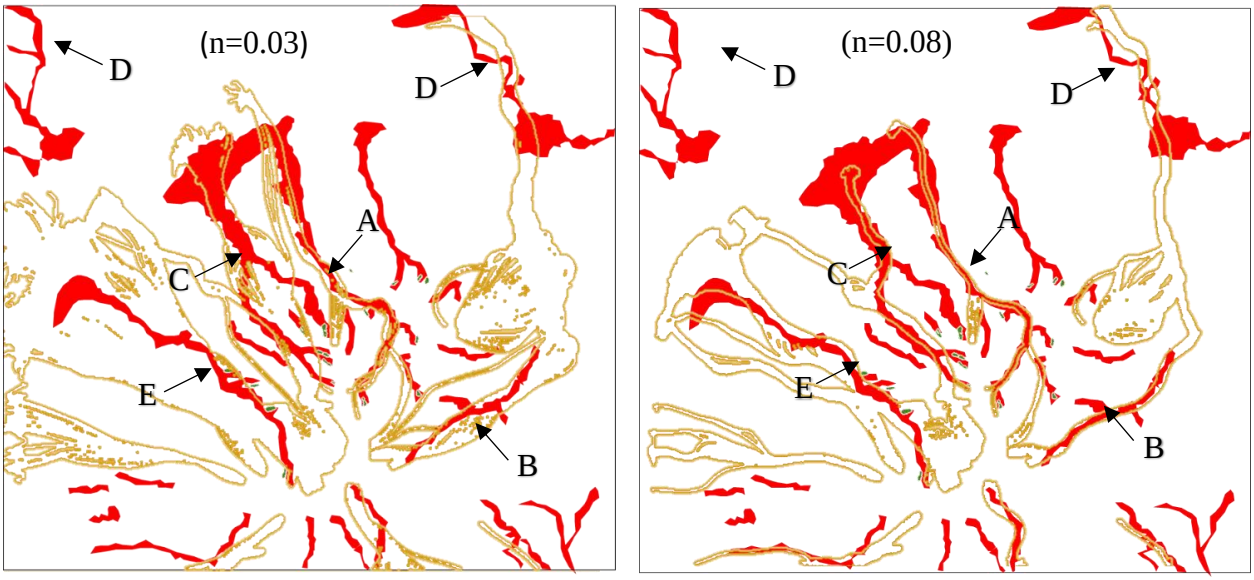

Figure 36 comparison between simulated and observed inundation in the western part of the study area for (n=0.03 and 0.08 and θ_{cr}= 0.5 deg.).

The model results obtained using n value of 0.03 showed much wider (lateral) width for the case of both the surges A and B. whereas results obtained using n value of 0.08 showed much narrower width for the case of surges. Considering the comparison made using these two main surges of the debris flow in the western parts of the study area, it can be said that n values in the range between 0.04 and 0.07 can be selected to be fitting for the area. As to the flow surge marked by E, it can be seen that for n values mentioned above, the predicted results match bigger lateral width compared to the actual affected area. This due to the predicted initiation area was match larger than actual slope failure area identified by both debris movement distribution map (Watatsuki et al 2010) and (Yamashita et al 2017). Therefore, for this surge we made a separate analysis using the initiation area predicted by using slope inclination value 42 degree.

Figure 37 show the result of simulated inundated area using n values 0.06 and 0.07 and critical failure deposition angle of 42 and 0.5 degree for debris flow surges marked by E. For this main surge in this part of the study area it can be seen that, the predicted flow obtained using n value of 0.06 showed a bit wider but the result obtained using n value of 0.07 show a similar width with the actual event identified by the researcher mentioned in the previous sections (both soil movement distribution map (Watatsuki et al 2010) and (Yamashita et al 2017).In this figure (Figure 37) it is visible to seen that the extra longer flow travel in the prediction for the flow surge marked B is due to an extra initiation area in the middle of the study area (outlined by black polygon).

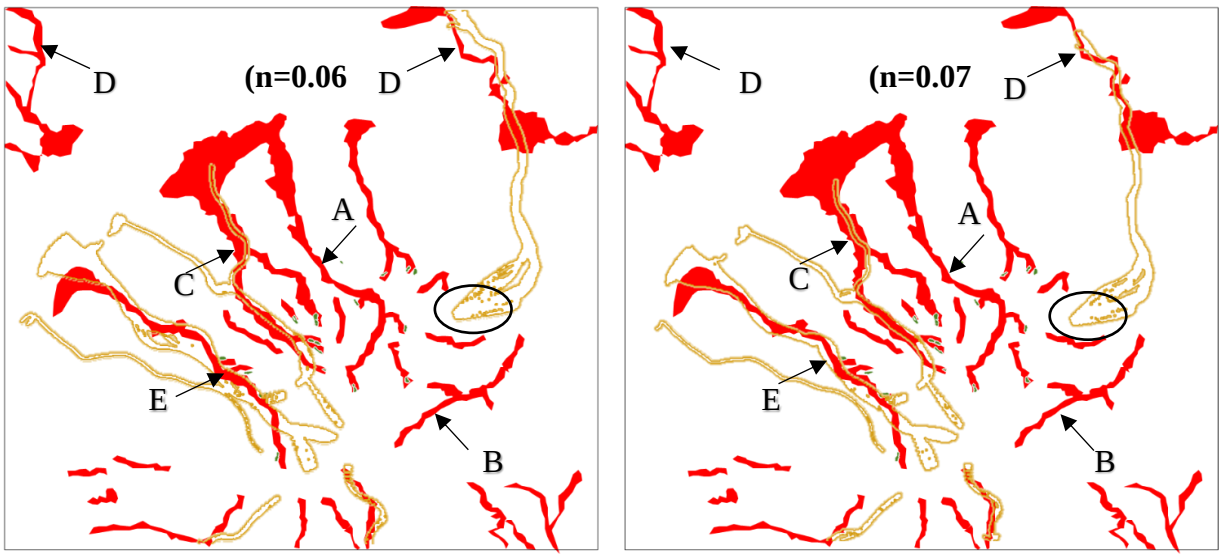

Figure 37 sensitivity of the result for Manning's (n) through comparison between the simulated and the actual inundation area for (n=0.06 and 0.07 and θ_{cr}= 0.5 deg.

In this eastern part, we made also a comparison between simulation and observation using lower n values (0.03) and greater (0.08) than the values mentioned above shown in below to make a complete sensitivity analyses. In this figure (Figure 38), similar to the discussions made above, the model results obtained using n value of 0.05 showed much wider (lateral) width compared to the actual even. Whereas results obtained using n value of 0.08 showed much narrower width for the case of this surge. It can be noticed that, the simulation results obtained using n values (from 0.05 to 0.08) was in the acceptable range. The range n values (i.e. between 0.05 and 0.08) becomes smaller compared to then values (between 0.03 and 0.08) as the number of surges considered becomes smaller and smaller. From this it can be once again noticed that the simulation results are sensitive to both the initial mass discharge and the resistive characteristics of each flow channel (characterized here by selection of θ_f and n values).

It can be also seen that that for all results obtained using n values in the range between 0.03 and 0.08 the simulation results can be seen visibility to be longer compared to the actual observed places. The critical deposition angle (θ_{cr}) parameter control the area of deposition fan, for overland flow in the Bingham fluid model we used. And this value was kept constant to be 0.05 in all the simulations shown above. The following sections show the analysis of the model results using varying values of critical deposition angle (θ_{cr}).

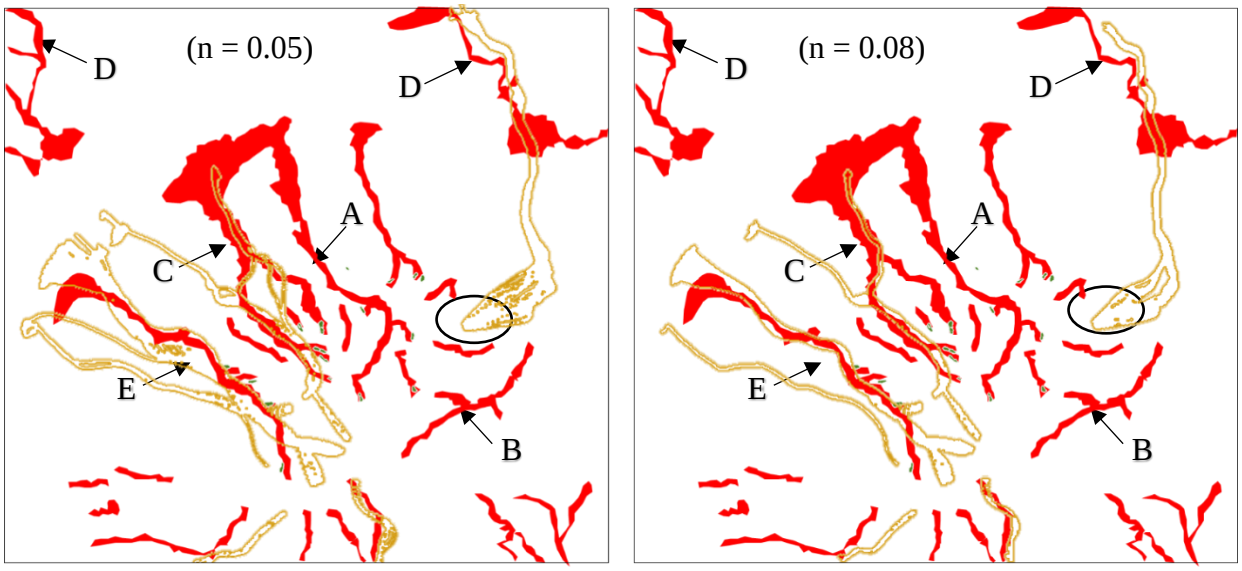

Figure 38 comparison between the simulated and the actual inundation in the eastern side of area for (n=0.05 and 0.08 and θ_{cr}= 0.5 deg.)

Figure 39 shows the comparison between the simulated and the actual inundation area for (n=0.06 and θ_{cr}= 0.5 and 1.5 deg.). It can be seen that the difference is not only in the location the deposition area but also the lateral width of the flows both in the initiation and deposition area (as indicted by the black polygons) happens to vary considerably. Indeed, it can be seen from the formulation of the Bingham fluid as a constitutive model that these two material parameters have dependence on each other. Hence both parameters (n and θ_{cr}) need to be adjusted simultaneously to achieve a satisfactory visual match between the observed and simulated results.

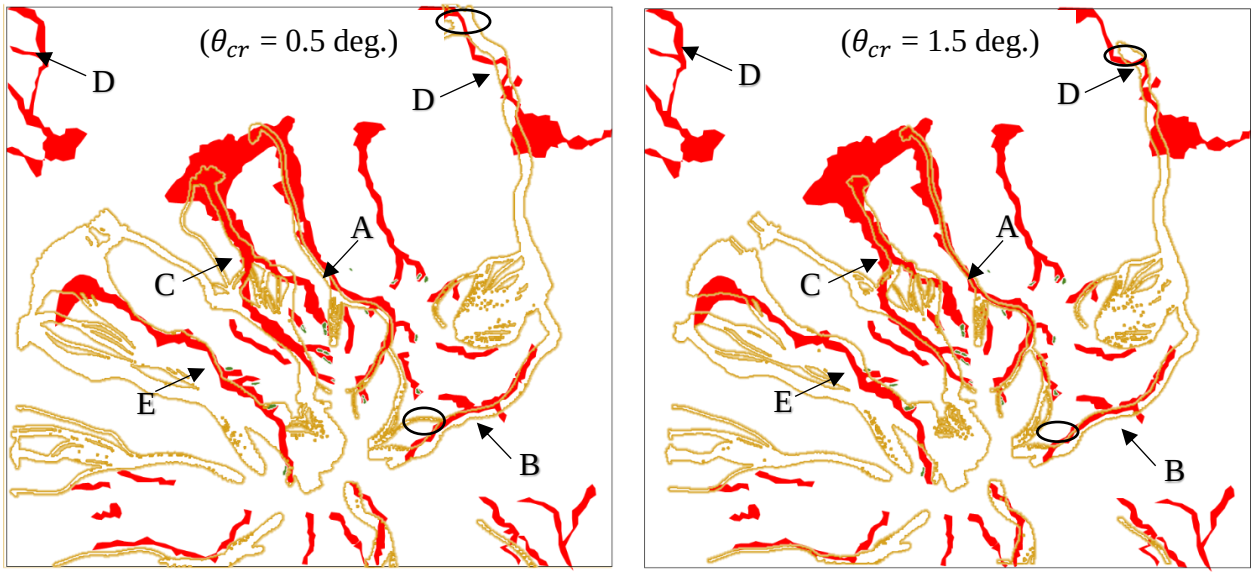

Figure 39 sensitivity of the result for critical deposition angle (θ_{cr}) via comparison of simulated and the actual inundation area for (n=0.06 and θ_{cr}= 0.5 and 1.5 deg.) A critical slope failure angle θ_f = 40 degree was used to predicted initial slope failure area for the western part of the study area.

However, a separate analysis of each parameters made so far helped as to determine the ranges values for each parameters distinctly. After knowing the ranges of each separate parameter values then we made analysis by varying the two parameters simultaneously to search for the acceptable ranges of the values that fit for the study area.

Figure 40 shows a comparison simulated and observed inundated area using the ranges the two parameters considered to be acceptable to best fit for the study area. At the lower bound value $\theta_{cr} = 0.05$ and using $n = 0.05$, we can see that the simulated result quite acceptable for the surge marked as A but for the surge marked by B the result showed an extra prediction. At the upper bound value $\theta_{cr} = 7$ and using $n = 0.07$, we can see that the simulated result is quite acceptable for the surge marked as B but for the surge marked by A the result showed shorter prediction. Therefore, it can be concluded that, the values in between these two lower and upper bounds can be used for the western part of the study area.

For the eastern side of the study area, concerning to the surge marked as E, Figure 41 show the result of simulated inundated area using the lower and upper n values 0.05 and 0.08 and θ_{cr} value of 0.5, 4 and 7 degree. For this main surge in this part of the study area it can be seen that, the predicted flow obtained using n value of 0.05 and $\theta_{cr} = 0.5$ showed a bit longer and wider but

the result obtained using n value of 0.05 $\theta_{cr} = 7\ deg$ showed wider but shorter than the observed inundated area. The result obtained using n value of 0.08 and $\theta_{cr} = 0.5$ showed a bit longer and wider but the result obtained using n value of 0.05 $\theta_{cr} = 4\ deg$ showed similar width and length with the actual event. Therefore, for the eastern side of the study area, it can be seen that a better upper and lower bound can be (n, θ_{cr}) = (0.05 to 0.08, 0.5 to 4 deg.) that fits to this area

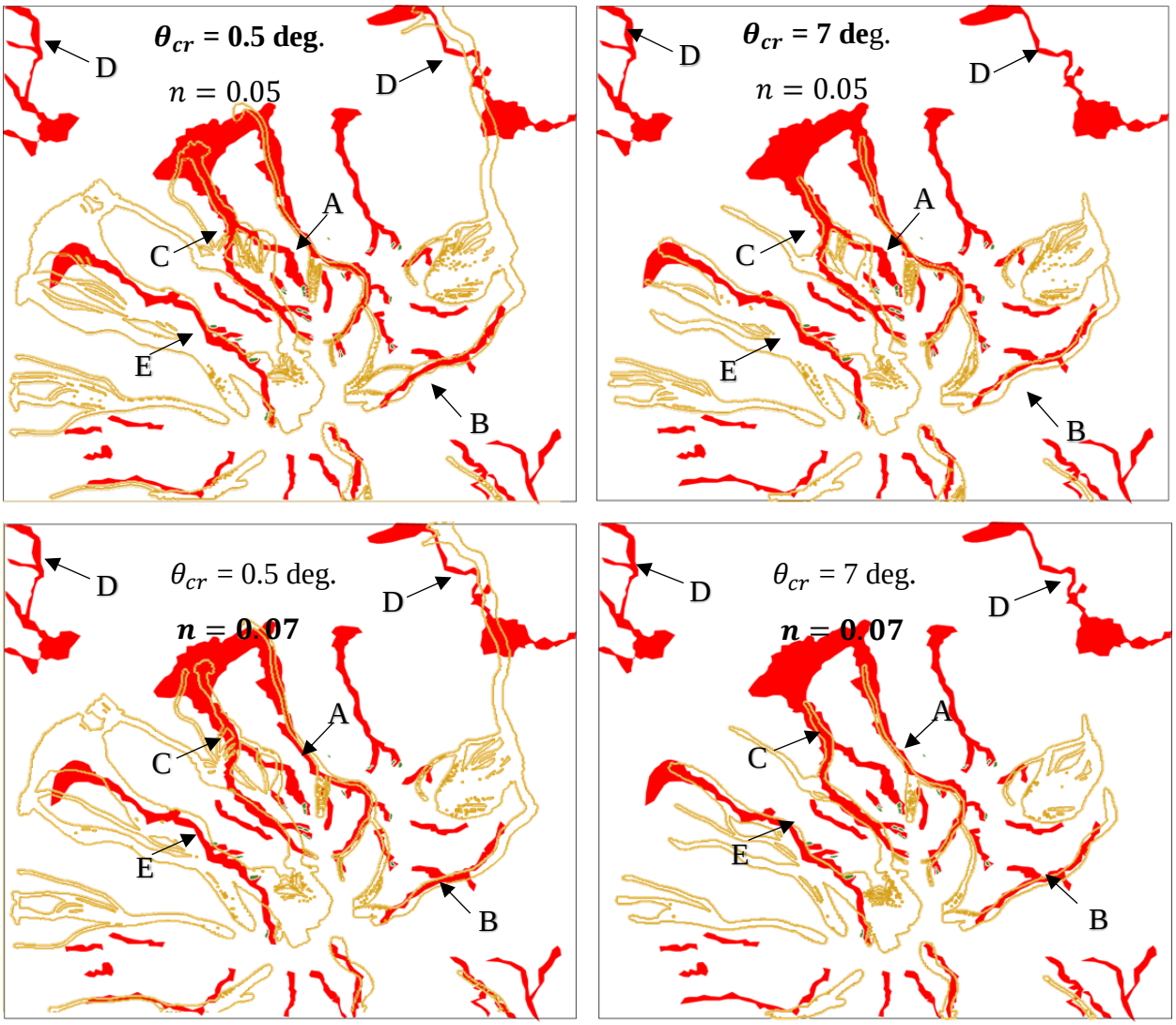

Figure 40 comparison of simulated and observed inundations using acceptable lower bound value of n (0.05) and upper bound value (0.07) together with upper and lower bound value of θ_{cr} (0.5 and 7 deg.)

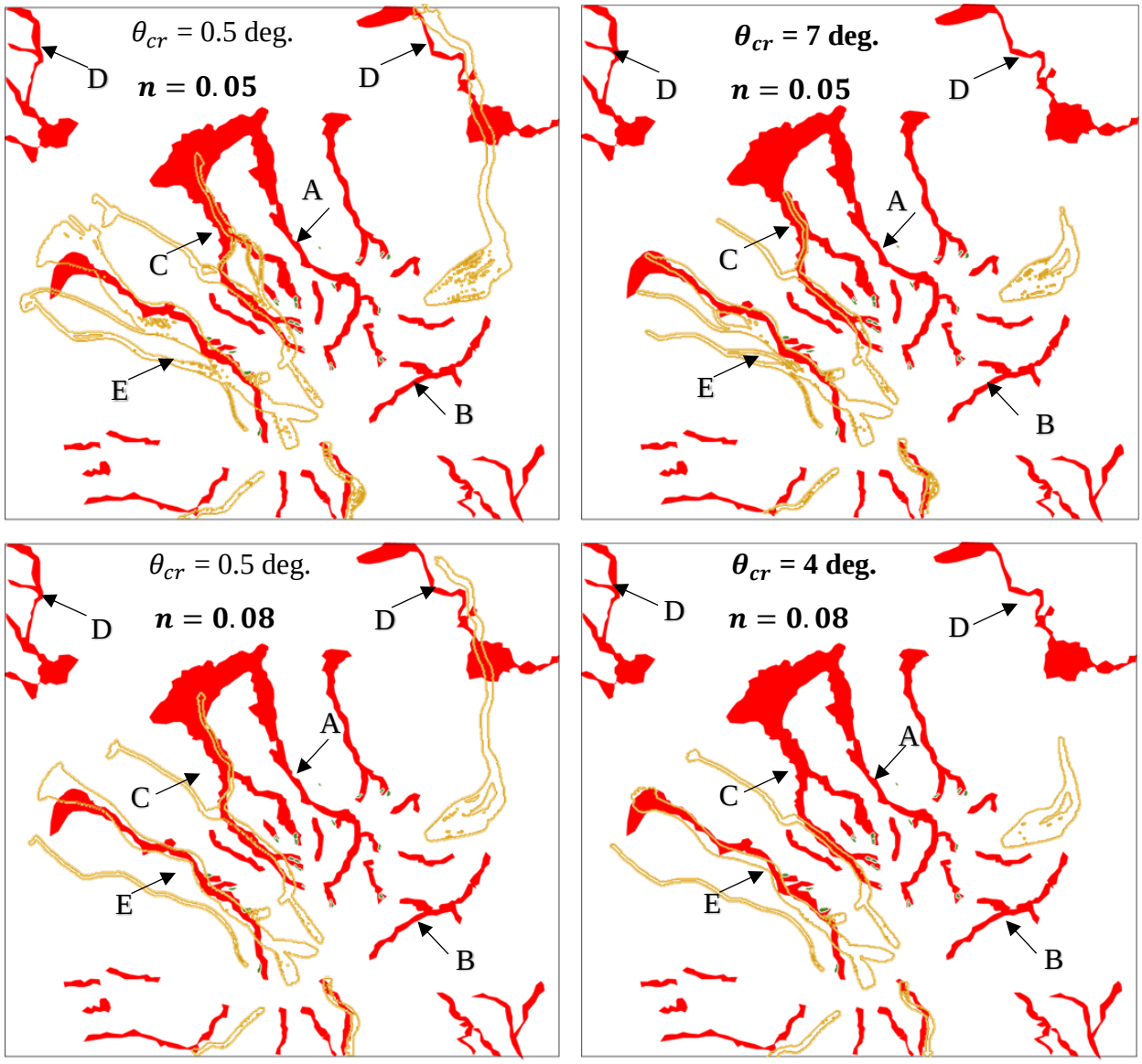

Figure 41 simulated inundated area using the lower and upper n values 0.05 and 0.08 and θ_{cr} value of 0.5 and 4 degree for eastern and 7 degree for the western side of the study area.

5.2 Case study 2: Calibration of the material parameters for debris flow affected area in Kumamoto prefecture, japan

We also make an investigation using another case study area a well-documented landslide event that occurred on July 19-20, 2003 in Hougawauchi area nearby Minamata city, Kumamoto prefecture (Figure 42) (Iwao 2003, Taniguchi 2003, Nakazawa et al. 2003, and Wang et al. 2006).

The main slope failure occurred in the middle reaches of Atsumari ravine, and the volume of the landslide mass is approximately 50,000 to 100,000 cubic meters (Taniguchi 2003).

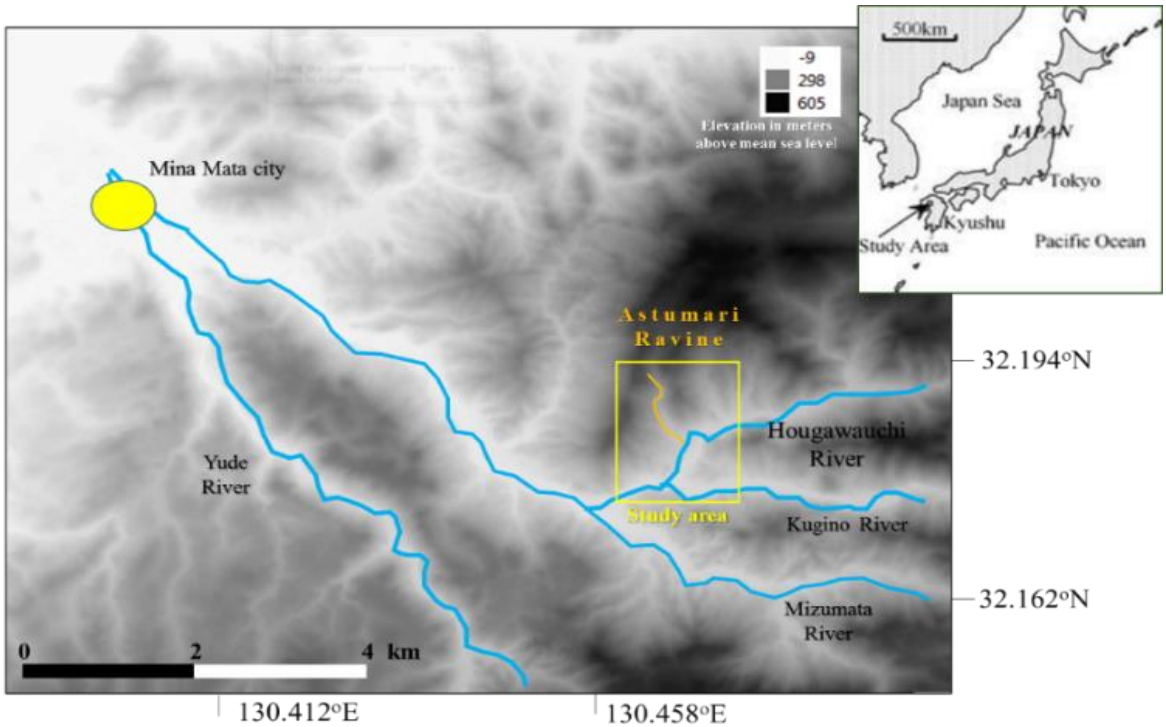

Figure 42 location map of case study area in Kumamoto prefecture in Japan.

The landslide triggered a debris flow, and it flew down about 1500 meters up to the junction with Hougawauchi river (Point B in Figure 43), and the flow velocity estimated from the difference between the inner and outer trace at the curved sections is ranging from 2.9 to 23.5 m/s (Mizuno et al. 2003). In addition, (Nakazawa et al. 2003) reported that the final debris flow deposition was observed from Point B to point A (whose elevation is 140 above sea level) as shown in Figure 43.

5.2.1 Estimation of the critical slope gradient of dry and saturated soil for the debris flow affected area in Kumamoto prefecture

Before making the prediction of slope failure location we made evaluation of the stability condition of the area using the available records. There are several classical ways to evaluate the slope stability. The simplest way is to use the 1D slope formula to compute the safety factor shown in equation (5-3).

$$F_s = \frac{C'/g + \lfloor \rho_1 h_1 + (\rho_{sat} - \rho_w)(h - h_1)\cos\theta \rfloor \tan\emptyset'}{\left(\rho_t h_1 + \rho_{sat}(h - h_1)\right)\sin\theta} \qquad 5\text{-}3$$

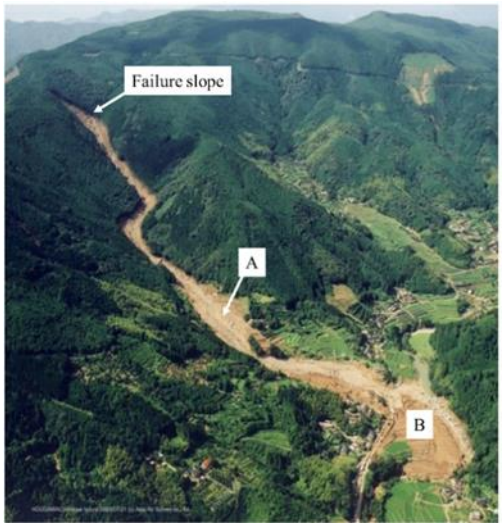

Figure 43 photo of the Kumamoto debris avalanche. Source: Asia Air Survey Co.

where θ is the slope angle, h and h_1 are the failure depth and the depth of ground water ($h_1 < h$), respectively, ρ_t and ρ_{sat} are the unsaturated and saturated bulk density of the surface soil, ρ_w (=1.0 (g/cm^3)) is the unit weight of water, and c' and ϕ' are the cohesion and the internal friction angle of surface soil, respectively, in terms of effective stress.

Another way to compute the safety factor is to use the method of slices such as Fellenius method, Bishop Method, etc. Wang et al. (2006) assumed the elliptic sliding surface and applied a couple of methods of slices into the above-mentioned Kumamoto landslide, and obtained the material parameters; c=20 (kN/m2) and ϕ=26 (deg.).

Using the data describing in Taniguchi (2006) (soil particle density ρ_s=2.6(g/cm^3), ρ_t=1.5(g/cm^3), porosity n=0.596), we can compute $\rho_{sat} = (1-n)\rho_s + n\rho_w$=1.65(g/cm^3). Assuming h =5.0(m), the slope inclination corresponding to $F_S = 1$ is θ_f =24.9(deg.) for h_1 =0(m) (fully saturated), and θ_f =49.5(deg.) (fully unsaturated). However, in the DTM obtained from the data of ALOS 30-m freely available source (Figure 44), the ratio of the number of meshes whose slope angle is more than 49.5(deg.) is less than 0.1%.

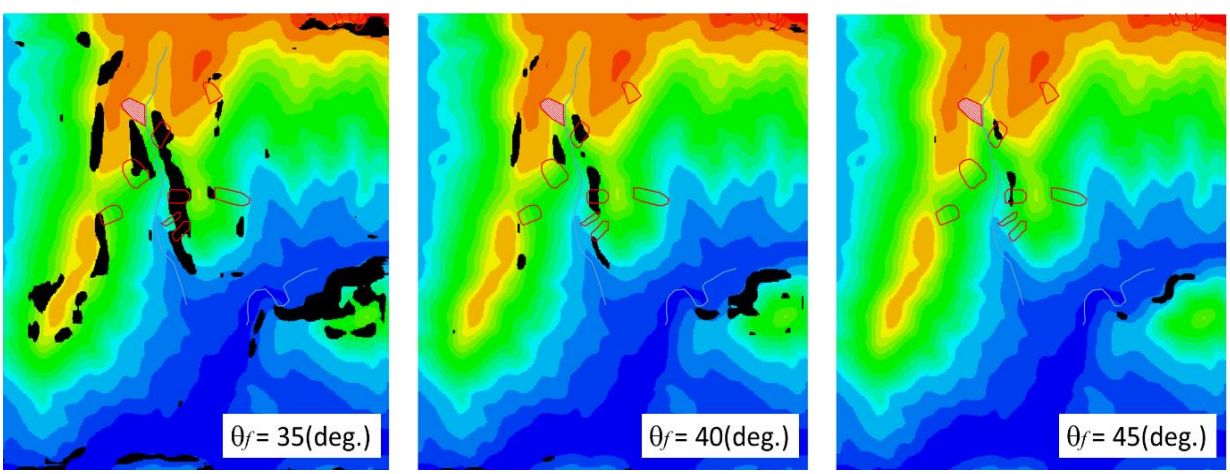

Figure 44 visual comparison between the predicted failure slope only by slope angle (black area) and the potential failure slopes based on 3D limit equilibrium model (red closed curves) (Wang et al. 2006).

Figure 44 shows the location of meshes whose slope angle θ_f exceeds (35, 40 and 45 degree) in black. The figure also shows the potentially dangerous slopes estimated by Wang et al. (2006) using the above-mentioned elliptic sliding surface method (in red).

The correspondence between them are not very good, which indicates the assumption of failure mode influences the prediction. Moreover, both predictions cannot cover the actual slope failure (hatched area in red in Figure 44, possibly because of the effect of heterogeneous groundwater paths and /or heterogeneity of geomaterials.

5.2.2 Simulating surface flows of a uniformly distributed particles over the entire ranges of the region for the Kumamoto case study area

We made also a similar simulation of flows of uniformly distributed raindrops in the Komamoto area. Figure 45 shows the distribution of the number of particles passing in the respective location of the study area.

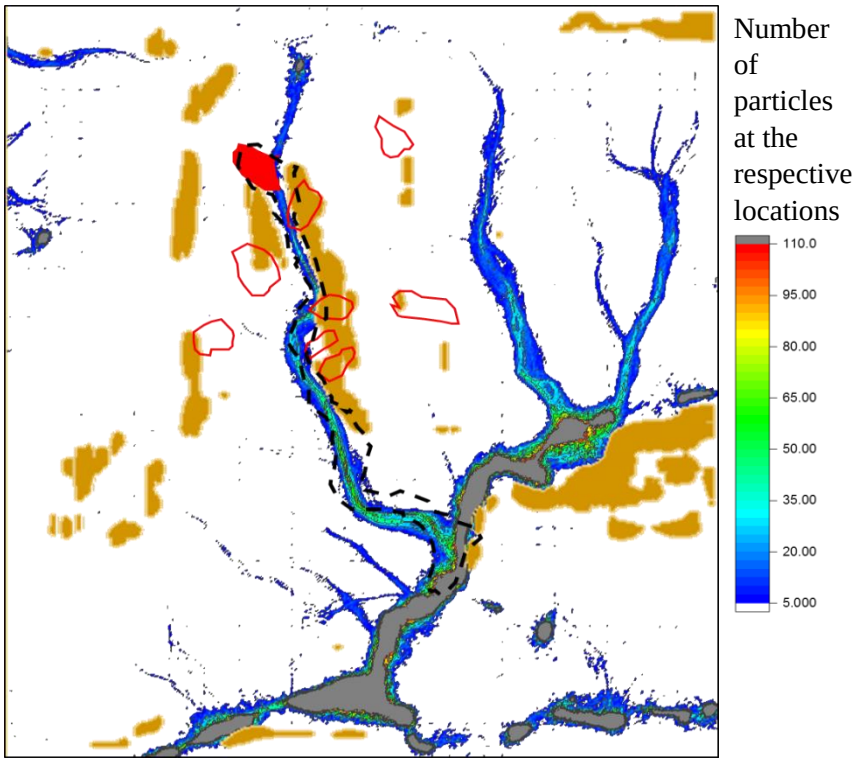

Figure 45 simulated distribution of raindrops passing at the respective locations in the Komamoto area.

Gray shades indicate greater number of raindrops in that location, yellowish color polygons show location of meshes whose slope angle θ_f exceeds 35 degree and the hatched area in red show the actual slope failure area while area outlined by broken black lines show the debris flow affected area.

Apart from the major drainage channels, a relatively higher number of particles can be seen in the middle of the initial slope failure area of the debris flow event. And the final deposition area can be seen corresponding to a higher accumulation of raindrops.

A large portion of the location of meshes whose slope angle θ_f exceeds 35 degree and the western side of the debris flow affected area can be seen covered by the larger number of simulated raindrops. This may possibly indicate a failure of slopes accompanied by a strong river bank erosion along the indicated drainage channels which had contributed the volume debris mass at the deposition places.

5.2.3 Calibration of the material parameters of the model for Kumamoto debris flow area

In order to calibrate the material parameters n and θ_{cr} for this case study area, we made gain a visual comparison of simulation results with observations and adjust the parameter values by trial-and-error until a satisfactory match is achieved in terms of the simulating the travel distance, the deposit distributions, and the velocities (Hungr 1995). The key outputs of the model, namely the flow direction and the path width can be adjusted using material parameters n and θ_{cr} after we assign the initial slope failure location (McDougall 2016).

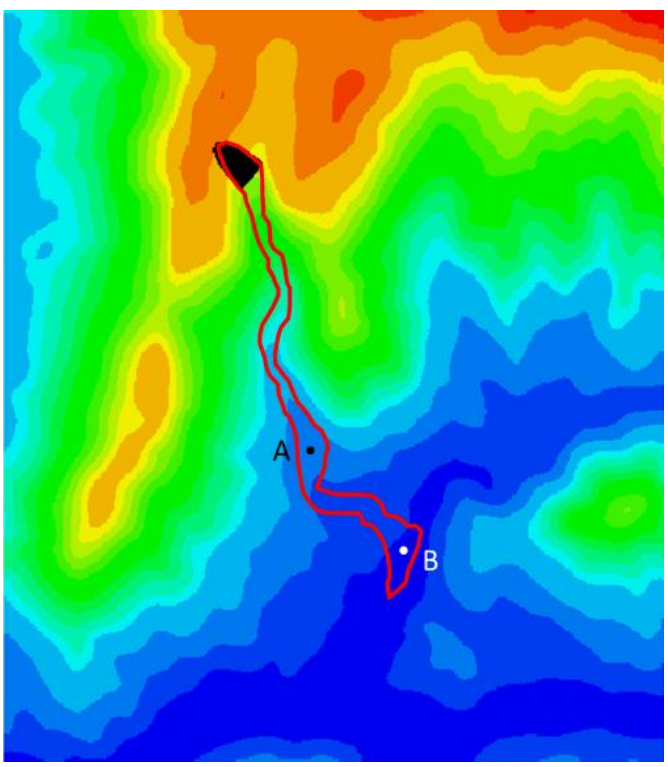

Figure 46 digital terrain model of the study area. Using data from ALOS 30m sources and after smoothening.

In this the Kumamoto debris flow case the even involves a single surge with the main slope failure as shown in black region in Figure 46. The maximum failure depth was reported as 15 to 20 m (Taniguchi 2003), but considering the failure area (170 m long and 100 wide) and the landslide mass volume estimation, we set the equal depth of 5 m.

Figure 46 shows an ALOS free DTM of 2150 by 2350 meters that we used in the following simulations. The degree decimal values were first changed in to meter

values using projection of WGS84 zone 52. Elevation values range from 540 meters above mean sea level in the northern part of the study area down to around 60 meters in the lowland area in the south and southeastern periphery. The DTM data was modified by the smoothing process as described in Section 3 and interpolated to make 5m mesh. The figure also shows Points A and B in Figure 43 and the observed affected area by red lines (Nakazawa et al. 2003).

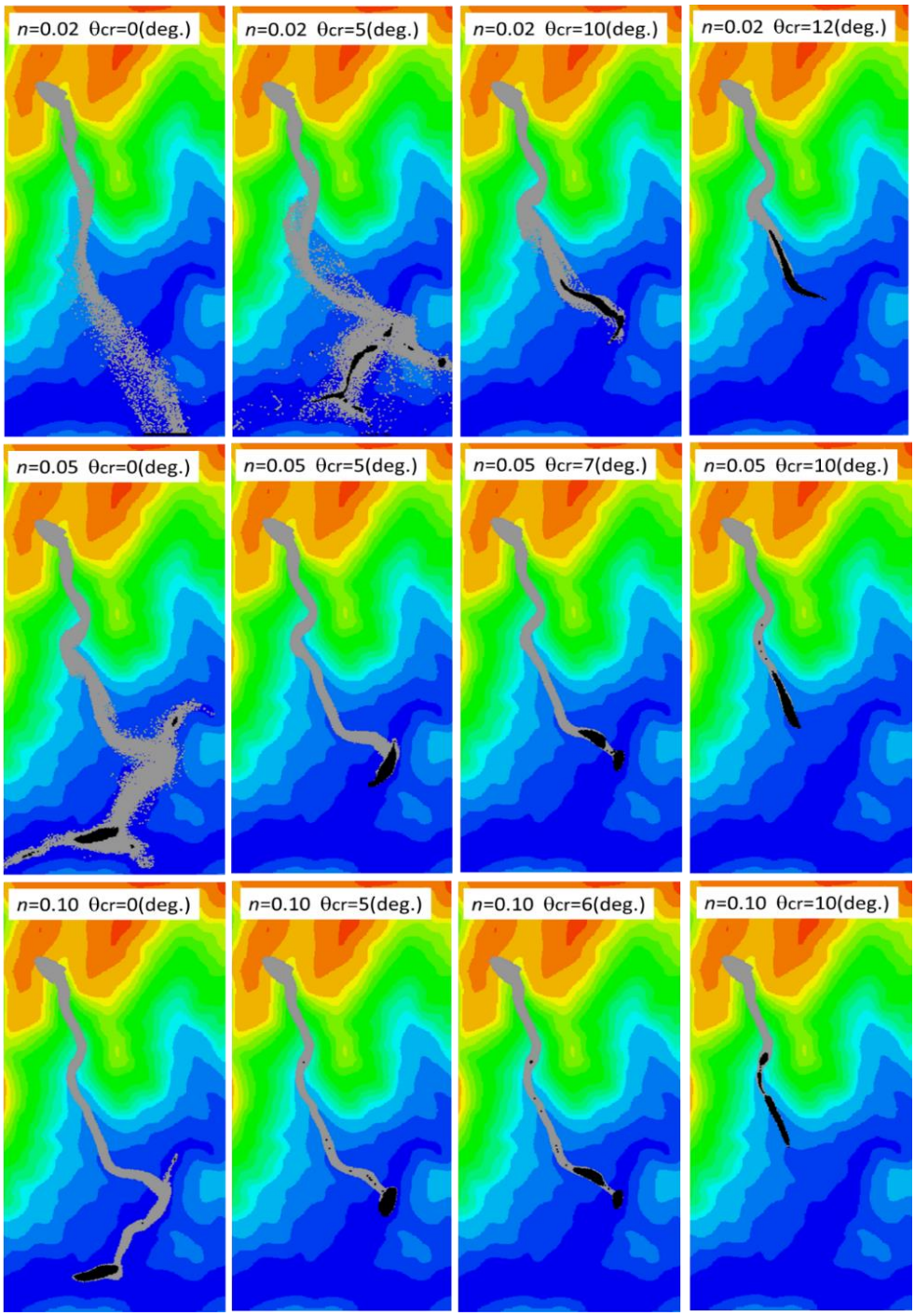

Figure 47 simulated inundation area (in grey) and final deposition area (in black) for various (n and θ_{cr}).

Figure 47 shows the simulated inundated area in grey and the final deposition area in black for various set of (n, θ_{cr}). As a general trend, the inundated area becomes smaller and narrower as n and θ_{cr} increase. Considering the fact that the actual debris flow stopped at around Point B, their maximum and minimum values can be identified.

Then, if we compare the simulated inundated area with the actual one in Figure 48 it turns out that the case for smaller n (smaller bottom shear stress) leads to an excess flow acceleration and results in the too much deviation from the path of valley bottom in the upper stream. On the other hand, in the downstream at around Point A in Figure 47, the simulated inundated width is narrower than the observed one for larger n.

Moreover, looking at Figure 49 which shows the time history of the maximum velocity of the flowing mass, it can be seen that the maximum velocity for the case of n=0.02 is too large compared to the evaluation by Mizuno et al. (2003) described above.

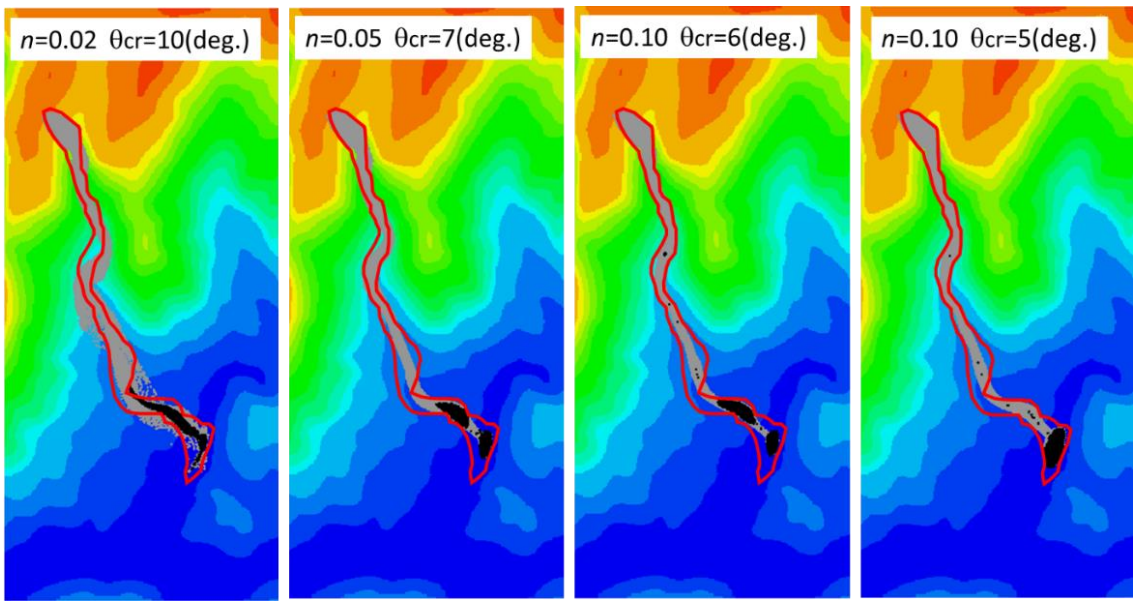

Figure 48 comparison between simulated (in grey) and the actual (in red) inundation area for different set of (n and θ_{cr}).

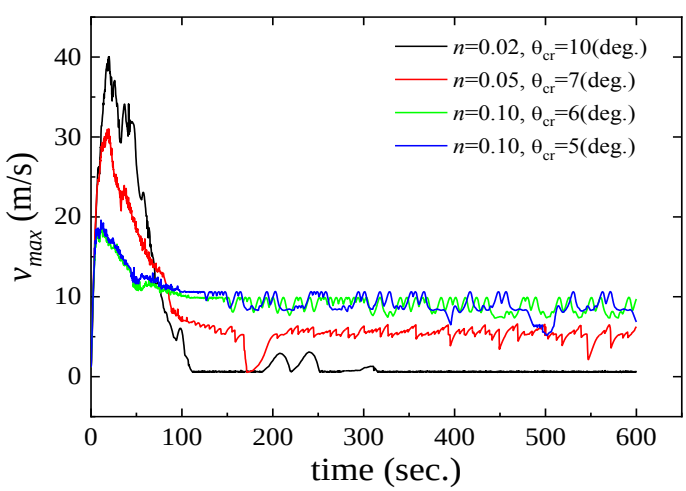

Figure 49 time history of the maximum velocity of the flowing mass for different set of (n and θ_{cr}).

Consequently, the most appropriate values are (n, θ_{cr}) = (0.05 to 0.10, 5 to 7 deg.) if we adopt a single set of values throughout the simulation. However, recalling Table 1, the Manning's coefficient differs in different ground surface materials, and it may be reasonable to set a larger value in the upstream and a smaller value in the downstream based on the aerial photo information such as in Figure 43. It should be also noted that increase in flowing mass due to valley bottom erosion (which was reported in Nakazawa et al. 2003 but not included in the present study) and additional water supply at the junction point with Hougawauchi river may contribute to the increase in the observed final deposition area at around Point B.

5.3 Summary of the calibration of the material parameters of the model

There are several approaches calibrating the material parameters of numerical models. We used a calibration technique based on a visual comparison of the main external aspects of landslide behavior such as how far do the flows travel and how wide ruins the flow spreading and the deposition fan. Though this approach is subjective, it is simple to implement when the model contains few adjustable parameters that dominate different characteristics of the simulation which can be adjusted relatively independently of each other. Such a visual comparison approach tends to require more interpretations using a large number of model calibration runs.

Depth integrated particle model provides an advantage of selecting the material parameters of the model based on a calibration made through applications into several case study areas affected by previous landslide events. Such a calibration approach is carried out routinely in geotechnical practice with limit equilibrium slope stability analyses (e.g., back-analyzing a failed slope to help constrain shear strength values) (Mcdougall 2016). A modified version of calibration of parameters using ratio between intersection and union of simulated and observed affected area was also employed in a selected the case study area in Ethiopia (the Debre Sina landslide area).

The calibration technique based on the main external aspects of landslide behavior requires making careful interpretations of a large number of simulation results. Even for a model that contain only two parameters with some four or 5 ranges discreet value (as the case in here), it needs to consider simulation results with a total number equivalent to the permutation of these numbers which turns to be a tedious task. And hence it is apparent that a lengthy period of calibration is likely required (Dai et al 2002). However, after the parameters are calibrated, it provides advantage of applying

the model to evaluate wide area slope disaster risk, in particular where the geologic record of past events is insufficient.

The initial slope failure area need to be determined in advance in order to calibrate the flow parameters (n and θ_{cr}). This is due to the flow inundation results are sensitive to the initial mass discharges of the debris flow. Estimation of a potential initial slope failure hazard area using 3D slopes stability analysis was done using historic landslide for the Kumamoto debris flow affected area (Wang et al 2006). A 1D slope stability analysis was applied here to estimate the critical failure slope gradient values of the dry and saturated soils in both Hofu and Kumamoto landslide affected areas.

However, the locations of mesh values in the respective critical slope gradients for dry soil (60 degree for Hofu case) and (49.5 degree for Kumamoto case) were less that 1 percent in both of the DTM, obtained from high resolution airborne survey (for Hofu case) and from feely available data source (ALOS 30m mesh) (Kumamoto case). Moreover, for the Kumamoto case study area, the slope failure location identified by using slope inclination and the potentially dangerous slopes estimated by Wang et al. (2006) using elliptic sliding surface method was not in agreement with the actual slope failure area.

Simulations of flows of uniformly distributed raindrops were made for the Hofu and Komamoto area. In both case of the study area a large number simulated raindrops were accumulated in the final deposition fan of the debris flow affected area. A strong correspondence between both in the sinuosity and pattern of depositions were seen between the simulated large number of raindrops and the path of the debris flows in both study areas. The result had also shown a difference between the eastern and western part side of correspondence between simulated raindrop distributions in the Hofu area.

Therefore we employ a user defined assignment of the initial slope failure area, for a debris flow involving a single surge (the Kumamoto area). However, due to the inconvenience of user defined assignment for a debris flow with multiple number of surges (Hofu case), we use a critical slope failure angle, θ_f to locate these places. From the sensitivity analysis between the initiation area obtained using some slope inclination and the actual slope failure area, it was able to select 40 and 42 degree for the western and eastern side respectively, to locate the initial slope failure zone in this area.

Using the user defined initial slope failure zone we made comparison of simulated and observed inundated area using various (n and θ_{cr}). In general it was seen that the case for smaller n (smaller bottom shear stress) leads to an excess flow acceleration and results in the too much deviation from the path of valley bottom in the upper stream. On the other hand, in the downstream deposition fan, the simulated inundated width is narrower than the observed one for larger n. Using a comparison at time history of the maximum velocity of the flowing mass with the evaluation by Mizuno et al. (2003) and looking at table 1, lower and upper bound value of (n and θ_{cr}) for was estimated to be in the range (0.05 to 0.10, 5 to 7 deg.) for the debris flow affected area in the Kumamoto prefecture. However looking at Table 1, the Manning's coefficient differs in different ground surface materials, and it can be recommended to set a larger value in the upstream and a smaller value in the downstream based on the information obtained aerial photo.

Due to the problem of too much initial volume of discharge predicted using only slope inclination values, we considered only certain main surges (marked as A and B) in the western side and a debris flow surge marked as E in the eastern of the study area. Looking the model results obtained using n value of 0.03 to be much wider (lateral) width for the case of both the surges A and B using n value of 0.08 to be much narrower width for the case of surges it was able to set the lower and upper bound for n value to be in these two values. However, it was seen that the variation of the simulation result using these two parameters was not independent of each other. Generally, a range values between (0.05 to 0.08, 0.5 to 7 deg.) was estimated to be fitting for the western part of the study area. And a range values between (0.05 to 0.08, 0.5 to 4 deg.) was estimated to be fitting for the eastern side of the study area.

Table 3 summary of the upper and lower bound values of calibrated material parameter

Case study area	$\boldsymbol{n}$		$\boldsymbol{\theta_{cr}}$ **(degree)**	
	Lower	upper	Lower	Upper
Hofu area	0.05	0.08	0.5	7 (4)
Kumamoto area	0.05	0.1	5	7

Calibration of the two material parameters, the Manning's coefficient, n and the critical slope angle for the deposition, θ_{cr} was demonstrated in the case study of both the Kumamoto debris flow

and Hofu shallow landslides. Table 3 recaps the upper and lower bound values of these parameter for the two case study area.

In both cases the lower value of n and the upper value $\theta_{cr}$was equivalent except the eastern side of Hofu case study area which as a 4 degree value. The upper value of n and the lower value of θ_{cr} showed some differences.

These difference arises due to the problem of predicting accurate initial volume of discharges. The prediction of initial slope failure is still a big issue to be improved. Nakata and Matsushima (2014) attempted a statistical analysis of landslide affected area which suggested the importance of considering the rain water catchment topography in relation to the saturation of soil as many others focused on (Burton and Bathurst 1998, Crosta and Frattini 2003). The difference in the terrain input data used in the two case study area has affected also the magnitude of the two material parameters as pointed out in section 3.2.2. Prediction of the flow-path and the deposition fan of the debris flows is found to be more reliable with airborne survey high resolution terrain source compared to a freely available global source. However, calibration of the model parameters using globally available terrain source with identical resolutions all over the world will resolve such differences.

The key issue here is to develop a method to obtain important material parameters from available GIS data such as maps that show the extent and distributions of the damages in the area. The availability of a model that can be integrated with a terrain model obtained from a global freely available sources make it essentially applicable all over slope disaster susceptible places for both experts and practitioners, while models that are commercially available tend to be expensive. Moreover the model results are found to be directly applicable into risk assessment calculations in order to be used as a visualization and communication tools.

In general, for those main debris flow surges in the eastern and western part of the study area (Hofu case), in which the initial slope failure were accurately identified to a certain degree, the predicted simulation results were able to reproduce the propagation and deposition fan in good agreement with observations made by previous researchers in these areas. A similar coincidence between observed and simulated results was also demonstrated using user defined initial slope failure zone (Kumamoto case).

The numerical method together with a digital elevation model constructed using a Grass GIs made it possible to study the behavior the debris flow situation in both areas, using an acceptable terrain model. The proposed DIPM (depth-integrated particle method) with a simple flow constitutive model, can be used for wide area risk evaluations to estimate the flow ranges and to define potentially hazardous areas of the deposition fans.

6 Application of the model to evaluate wide area slope disaster risk in Ethiopia

6.1 Risk evaluation of the Debre Sina slope disaster area

6.1.1 Introductions

In Ethiopia, the hilly and mountainous terrains of the highlands are frequently affected by rainfall-induced landslides of different types and sizes causing loss of human lives, failure of engineering structures, damage on agricultural lands and on the natural environment (Woldearegay 2013). Furthermore, the area between the highland and Ethiopian Main Rift (EMR) system is vulnerable to landslides due to earthquake tremors associated with the Afar Triangle.

The study area lies at about 190 km northeast from Addis Ababa Figure 50. It is one of the areas located in the high seismic zone, with relatively high annual rainfall. It is characterized by gentle to steep slope gradients, dense drainage system & deep river cut and gully erosion, with elevation range of 1,368 to 3,100 m above the sea level. The area includes a wide length of 4000m north-south and 6000m east-west distance. The middle and lower parts are densely populated and intensely cultivated. East facing steps of flat terraces and cliffs are commonly attributed to the

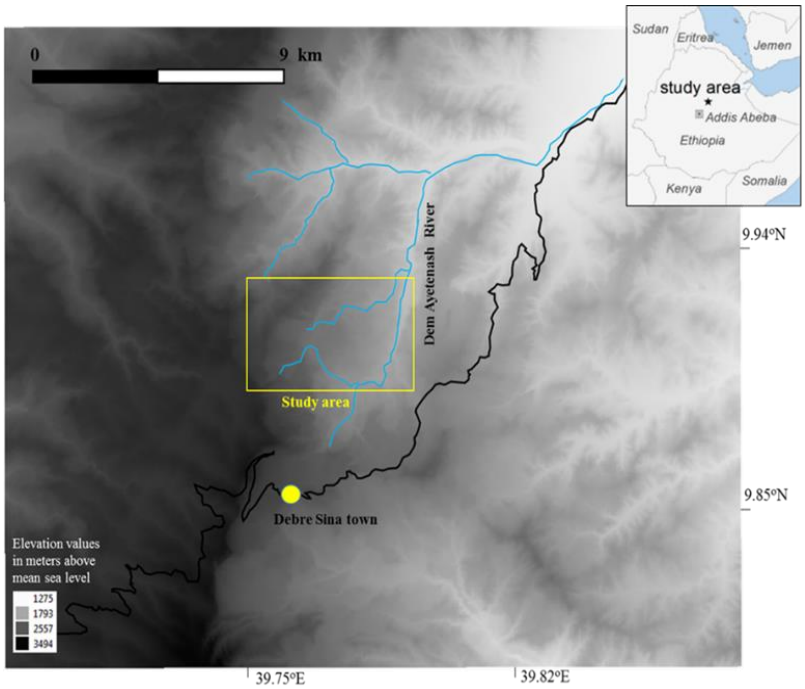

Figure 50 location map of Debre Sina landslide area.

rift margin faults (Abebe et al 2010).

This landslide event has been studied by several researchers including (Abay and Giulio 2012) who mapped susceptibility zones, investigated rainfall distributions, labeled basic geological location settings and pointed out earthquake situations around the Afar Triangle as the probable main triggering factor. Geophysical and hydro-geological researches were also made by (Alemayehu et al 2012). The Afar Triangle is a diffusive extensional region marking a triple junction, where three plates named as the African, the Indian and the Arabian plate meet. It is prone to significant level of seismic hazard due to the presence of the active regional tectonic and volcanic activities (Kropáˇcek et al 2015).

Figure 51 shows the satellite image of the study area. The event caused losses of over 900 hectares of arable lands, displacement of more than 4,049 peoples, destruction of more than 1,200 dwelling local houses and over 75% crop harvesting failure specifically in the localities named Yezaba (Woldearegay 2013). The prevalence of landslide hazards in this area could certainly have major role in aggravating the food insecurity problem of the country as most people living here are farmers who are dependent on subsistent agriculture.

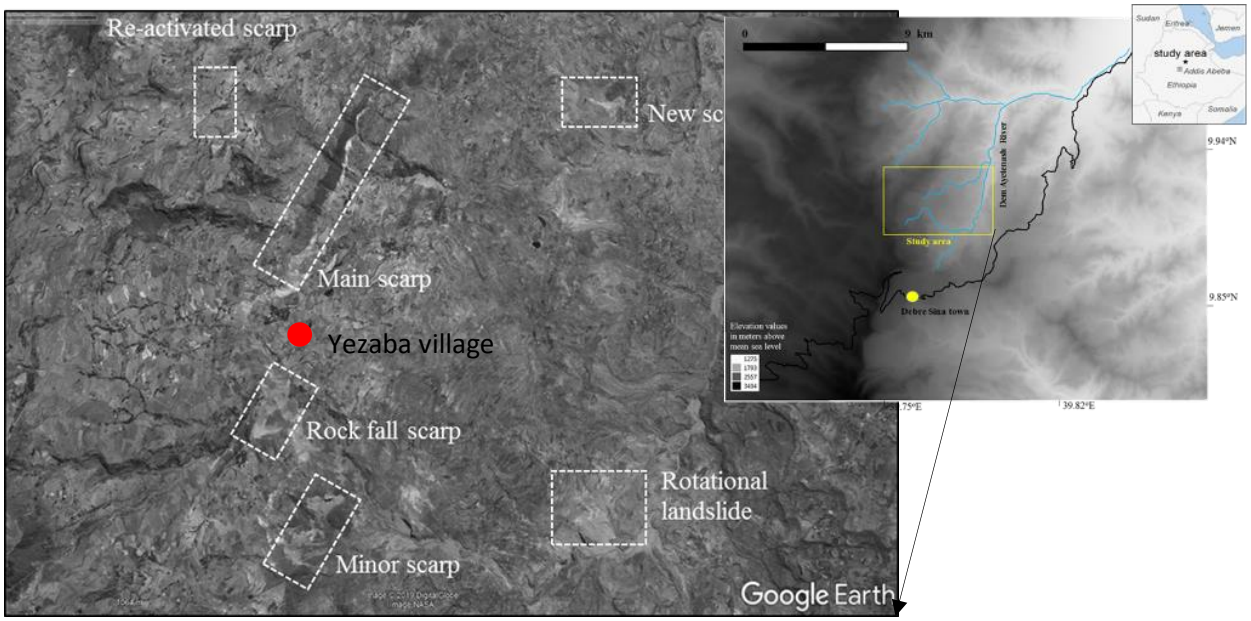

Figure 51 satellite image of the study area taken in the year 2007.

The image shows a main scar termed as here main scarp in the hillside along the northwestern periphery of the study of area. Another kind of slope failure termed as rock fall occurred in adjacent

area in the south western flank. Minor scarp, rotational landslide scarp, the new and re-activated scarp were identified from this image.

The date and year of the of landslide occurrence have been in controversies. Several views concerning the dating of the major events can be found in literature. The incidence of the primary phenomenon was dated to around August 2005 according to (Woldearegay 2008), but (Hagos 2012) argues to be around September of the same year. The major sliding event was dated as 13–14 September 2005 by the report of Action by Churches released in 2006. Due to the high elevation gradient in the study area the climate in the upper part is considerably colder and wetter. The landslide area is drained by the Dem Aytemashi River towards the north and later to the east towards the Awash River. The drainage pattern of the basin probably follows tectonic presetting

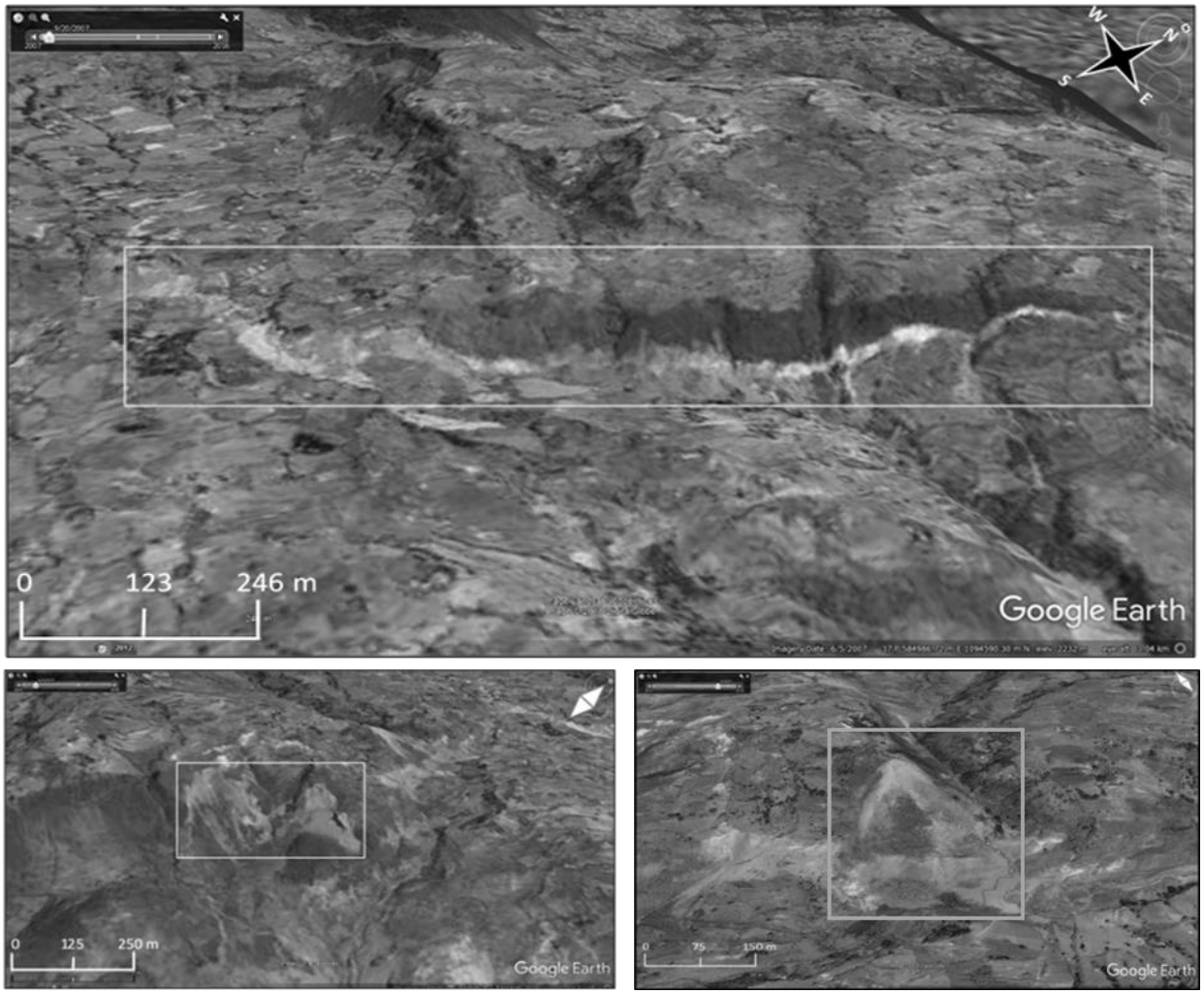

Figure 52 close up look at the primary slope failure areas.

Figure 52 shows enhanced snap shot of a satellite image around the Main (above), the minor scarp (below-left side) and the rock fall scarp (below-right side). In the Major carp area, an active scarp is displayed by whitish color bordered from above by an old scarp now covered by shrubs .It is characterized by deep-seated failure of large column of slope materials with depth up to 200m and length of nearly 1200 meters north east south west directions matching with the predominant direction of discontinuity (faults and lineaments) orientation that aligns WSW-ENE (NW-SE).

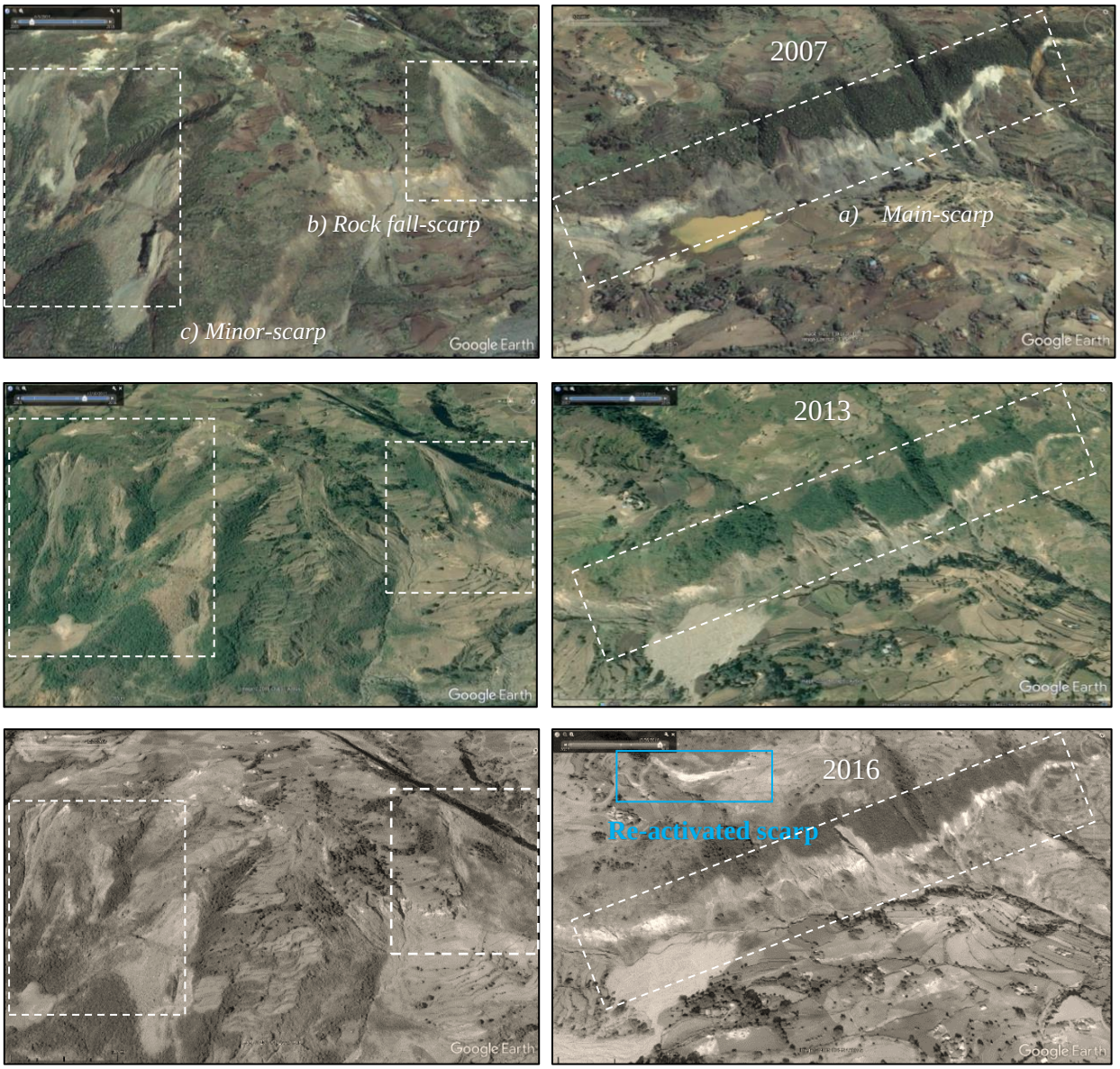

Figure 53 satellite images of the year 2007, 2013 and 2016 around the primary scarp area.

Figure 53 shows the images taken in the year 2007, 2013 and 2016 which indicate the processes of recovery. Through the development of time the scarps became covered by vegetation. It can be

seen also that the impact in the main scarp area do not well recover till now. Moreover, a new small area scarp can be seen above the old main scarp area. This probably shows the condition of a recurrent slope failure event in the study area.

When a slope fails, it is usually not possible to pinpoint a single cause that acted alone and resulted in instability (Duncan et al 2014). A single precipitation event listed in previous paragraphs as the daily maximum rainfall is unlikely to trigger a slope failure of such a large extent. It is pointed out by (Jan Kropatec et al 2015) that the sliding events were caused by a combination of geologic and tectonic predispositions together with external factors such as long-term water saturation and/or

Figure 54 lithological setting of the Debre Sina landslide area.

Figure 54 shows the lithological setting of the Debre Sina landslide modified from (Hagos 2012) and (Woldearegay 2013). The western part of the study area mainly contains basaltic composition of rocks forming a vertical cliffs and ridges trending in the N-S direction and some E-W offsets. Northwestern part of these ridges is formed by deeply weathered volcanic rock surrounded by unconsolidated colluvium material (Kropatec et al 2015). Alluvial deposits dominantly lie at the middle part of the catchment where there is relatively flat topography and following the river beds and river banks. It can be seen that the major, minor and the rock fall scarps lay in the alteration zones between the basaltic and fractured trachyte rock types.

Apart from the considerations of fracturing and layering, basaltic rocks remain to have higher strength compared to the sedimentary deposits. The state of layering and weathering vary associated with the type of different rock units. The layering and fracturing at the contact zone of separate lithological units can cause instability of slopes. In the main area of the slope failure zone,

the vertical/sub-vertical joints and tensional fractures create a promising situation for rainwater filtrations (Hagos 2012) which diminish the strength of the slope column materials and aggravate the damaging impact of the landslide event.

After slope failures flows slides down the slopes along the drainage channels and flood plains. Figure 55 shows the drainage networks obtained from the topographic map of the study area obtained from Ethiopian Mapping Agency (EMA). It can be seen that flow streams originate from the western side mountain ridges and flows down to a larger river channel in the eastern side the study area, named as Dem Ayetemashy.

Figure 55 topographic map of Debre Sina landslide affected area

Under dangerous flooding conditions it is estimated that all the drainage channels remains inundated by the debris flows. Hence the path and the location of these river channels can be used to evaluate the accuracy of the predictions of a numerical results.

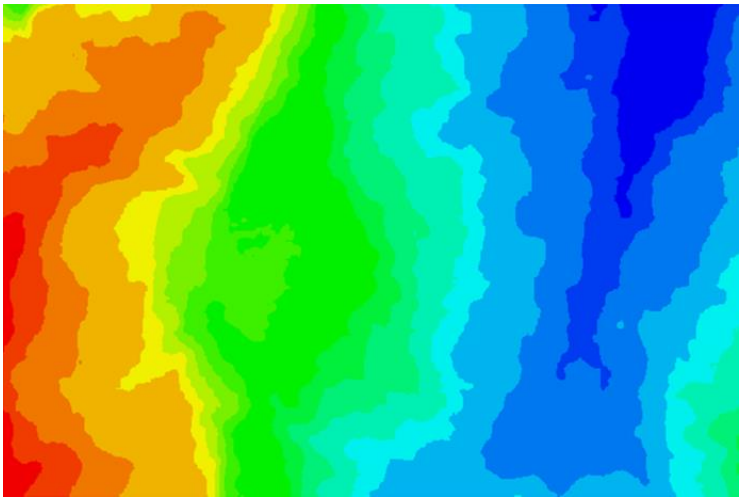
Figure 56 digital terrain model of the study area. Using data from ALOS 30m sources. After interpolation into 10-m mesh size.

Figure 56 shows digital terrain model of the study area obtained from ALOS 30m freely available source after interpolating and smoothening into a 10 meter mesh size intervals. The map shows morphological trends with high elevation around 2900m in the western peripheries and decreases down to about 1600m above sea level in the western side. Extra high values are shown in the southwestern side and lesser low values are spread in the northeast border of the area. Medium elevation values are

widely distributed in between these regions around the middle of the study area and in its most southeastern peripheries.

6.1.2 Delineation of the initial slope disaster area

The angle of internal friction, ϕ was estimated to be from 23 to 42 degrees, and the cohesion, c, value of 0.02 was estimated by a safety factor analysis made using 25 soil samples collected in the area, by (Hagos 2012). However, other required data including the unsaturated and saturated bulk

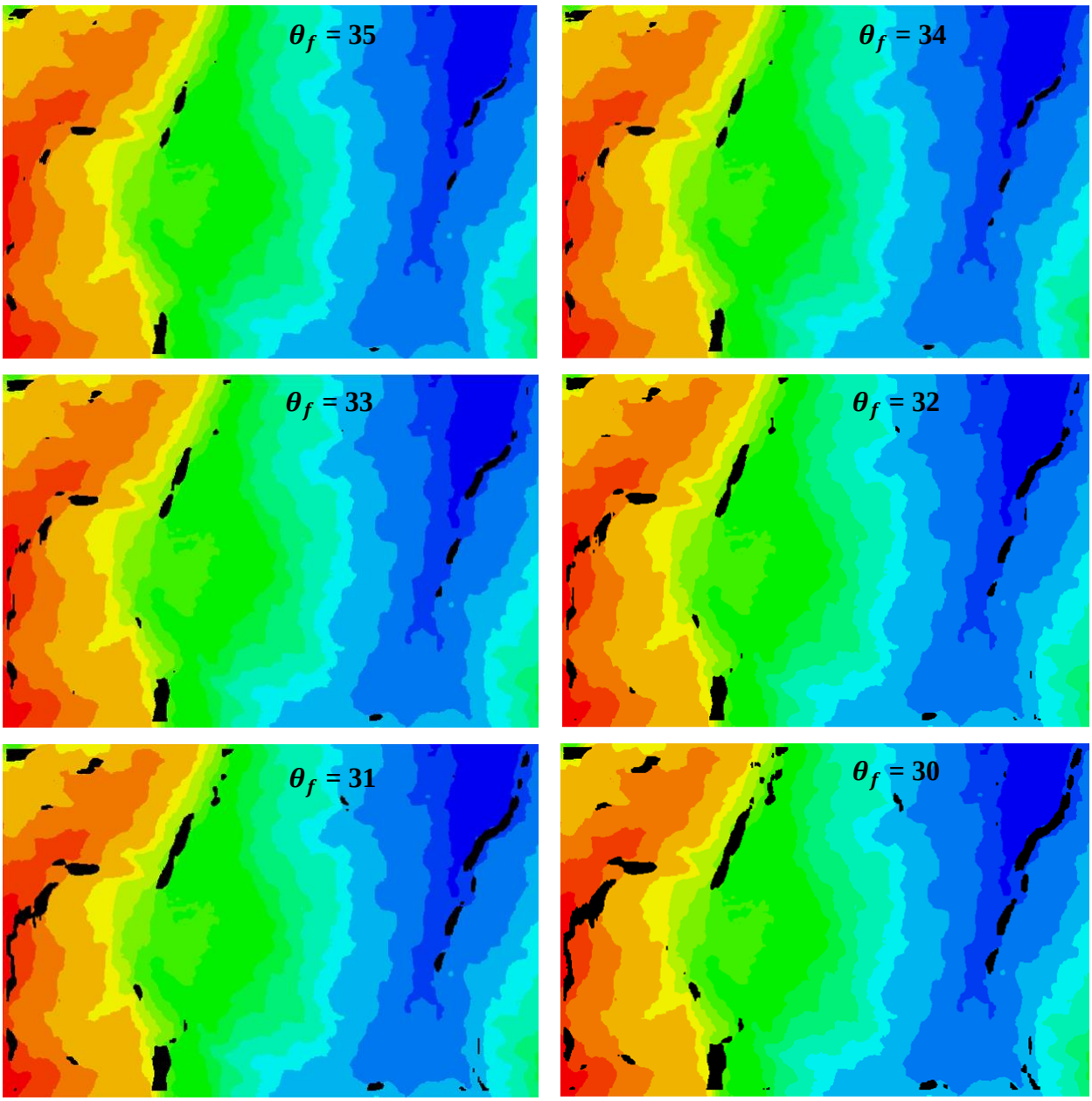

Figure 57 initial slope failure area predicted only by slope angle using θ_f from 30 to 35 degree.

density of the soil mass as well as porosity n of the surface soil was not available to compute the slope angle corresponding the safety factor value of $F_s = 1$.

Therefore, we use a critical slope failure angle θ_f,, value from 30 to 35 degree to predict the initiation area. Figure 57 shows columns of slopes identified by a given slope failure angle from 30 to 35 degree. Slope failure angle of 35 degree represents also entire ranges of values above this magnitude. The steepest slope gradient value was 35 degree. Few ranges of columns of slopes are shown both on the hill side in the western and nearly the central places in the study area; and around the lower altitude area in the eastern peripheries. Relatively wide columns of slope appear in the western side of the area around the medium elevation value places quite nearby to the center. Moreover, the majority of these slopes are concentrated in areas with high and medium elevation values.

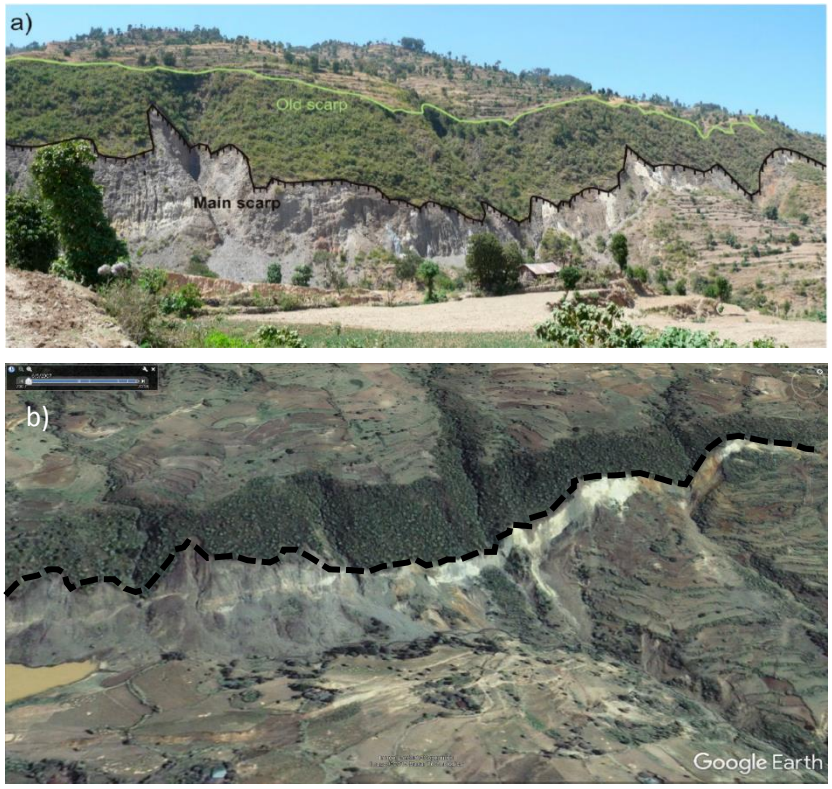

Figure 58 photo taken by (Kropáˇcek et al 2015); and b) a tilted view from year 2007 satellite imagery; around the main scarp area.

Figure 58 shows an association of the photo taken by (Kropáˇcek et al 2015) and a satellite image taken in 2007 around the main scarp area. And Figure 59 show a similar association between a photo and a satellite image for the case a rock fall event around same area.

Figure 59 photo taken by (Krthe opáˇcek et al 2015); and b) a tilted view from year 2007 satellite imagery; around the rock fall scarp area.

The effect of rock fall on the vegetation cover can be seen

visibly. The area formerly covered by grass and trees on the eroded cone shaped area at the upper part of the slope were eroded whereas a few amount of bushes in the middle of the slope still stay intact.

Figure 60 a panoramic view of the Debre Sina landslide area from east to west with displaced rock blocks with well-marked scarp line in the photo taken by (Kropáˇcek et al 2015). Figure 61 show a visible satellite image taken in the year 2007 which shows a clear out crop of a shear line in the middle of the study area quite similar to the panoramic view of the photo.

Figure 60 panoramic view of the Debre Sina landslide area from east to west with displaced rock.

Figure 61 visible shear line outcrop both in the central area (outline by dim red color line) and in the main slope disaster area (marked by black color line) visible on satellite image taken in 2007.

It can be seen from the similarity of the above pictures that satellite images can be used to obtain a satisfactory amount of information about the situations of landslide events, particularly for such a wide area slope disaster investigations. We used these satellite images to determine a threshold value of critical slope failure angle for the prediction of the initiation area.

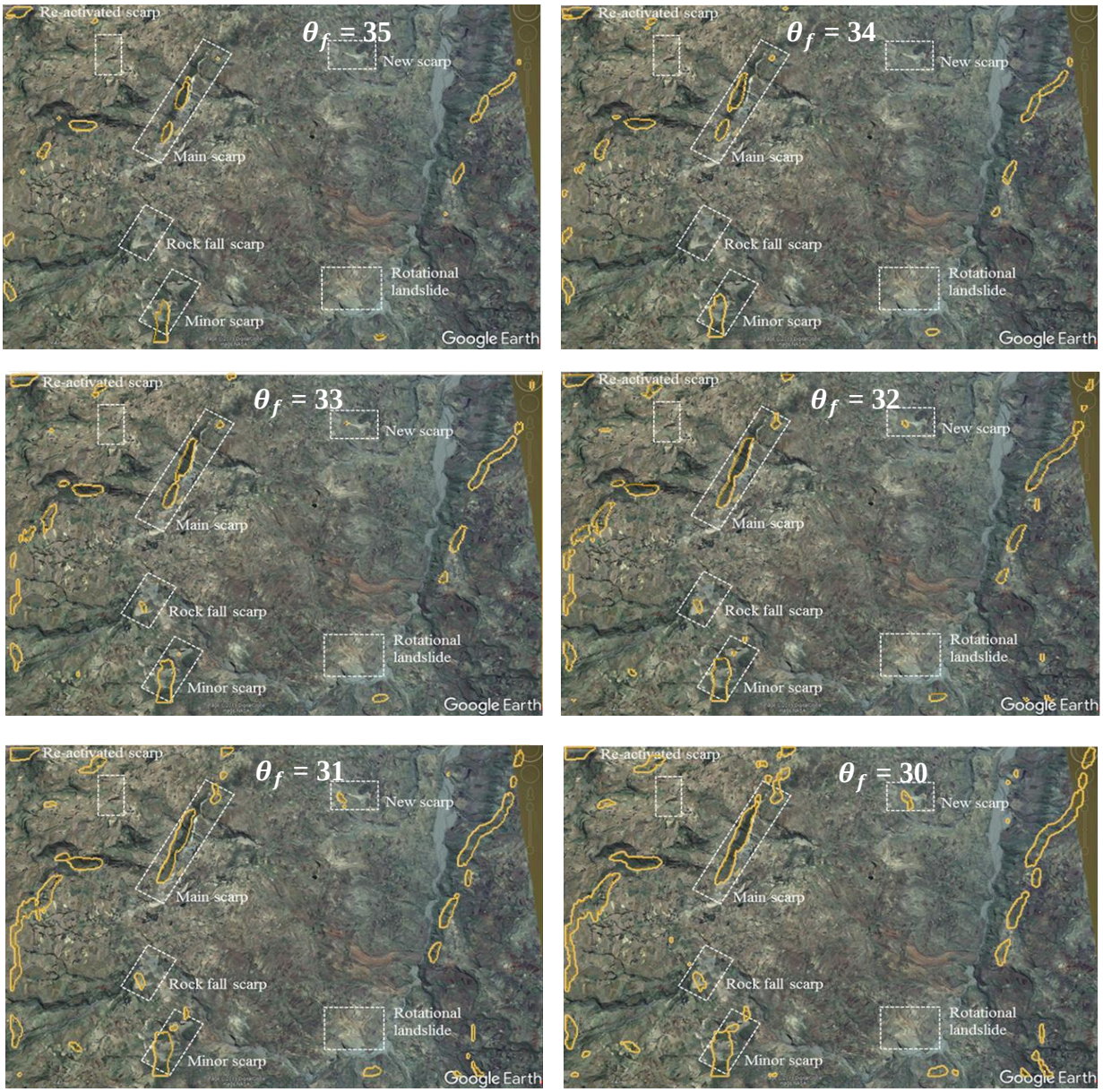

Figure 62 comparison of intersection between observed (outlined by broken white color polygons) and predicted only by slope angle (outlined by gray color solid polygons) of the initiation area.

Figure 62 shows a replication of the initial slope failure area predicted only by slope angle using θ_f from 30 to 35 degree on the satellite image of the study area. We made comparison of the

actual initial slope failure area and the predicted result in order to calibrate the parameter of the numerical model.

A calibration method similar to the one proposed by Galas et al (2007) was used for comparison. It is based on maximization of the ration of intersection between predicted (area outlined yellowish gray polygons) and observed (areas outlined broken white color lines) of area to select a threshold value the critical slope failure angle. Observed and initiation area was taken from the visible scarps of the satellite images.

We made a maximization of the ratio of intersection between the predicted failure area (a) and union (a + b) of the simulated and the observed inundation area represented by the index β. And the ratio of intersection predicted safe and failure area (a + d) and union of safe and failure (a + b + c + d) of simulated and observed inundation area represented by the index α. If the observed failure area (a + b) is predicted completely then 'a' becomes a zero value. Correspondingly, if the observed safe area (c + d) is predicted completely then 'c' becomes a null value.

Table 4 Indices' α and β values of the comparison between intersection of simulated and observed initial slope failure area.

visible scarps on the satellite image	Percentage value of intersection area between simulation and observation (β, α)					
	35º	**34º**	**33º**	**32º**	**31º**	**30º**
Major	42,85	54,86	76,92	92,94	96,92	97,88
Minor	43,52	62,67	69,68	73,67	76,65	82,76
Rock fall	0,50	0,50	51,53	64,63	64,67	64,64
New scarp	0,50	0,50	26,53	35,54	36,54	35,55

Table 4 shows the percentage values of intersection between the predicted and observed slope failure area using the definition give in Table 2 (shown here again to make convenient reference) and the percentage values of the indices described above.

The value β show the intersection of predicted failure area to the total observed slope failure area. And the ratio of α show the percentage prediction of total safe and failure area.

$\beta = \frac{a}{a+b}$ $\alpha = \frac{a+d}{a+b+c+d}$		**Simulation**	
		Unsafe	safe
Observation	unsafe	a	b
	safe	c	d

Figure 63 close up view of an overlap between simulated (in yellow) and observed (in broken white line polygons) around the minor scarp of the slope disaster even area. And Figure 64 close up view around the main scarp of the slope disaster event area.

It can be seen also from Table 4 that at the major and minor slope failure area, both α and β keep on maximizing until the slope gradient value of 32 degree. But after 32 degree the value of α starts to decrease. A similar trend of maximum intersection can be seen also for the rock fall event area.

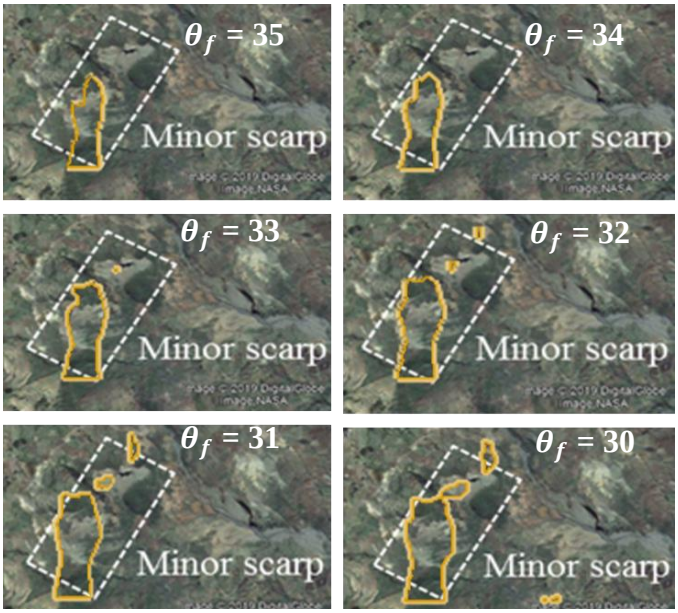

Figure 63 close up view of an overlap between simulated (in yellow) and observed (in broken white line polygons) around the minor scarp of the slope disaster even area.

Figure 65 show a replication of predicted slope failure overlaid by the geological map of the study area. It can be seen that the predicted slope disaster area align with the northeast-southwest alignment of the lithological setting of the study area. Therefore, using this threshold value of the slope gradient magnitude we can predict the other initiation areas (in the eastern and western peripheries of the study area) to be an initial slope failure zone of the

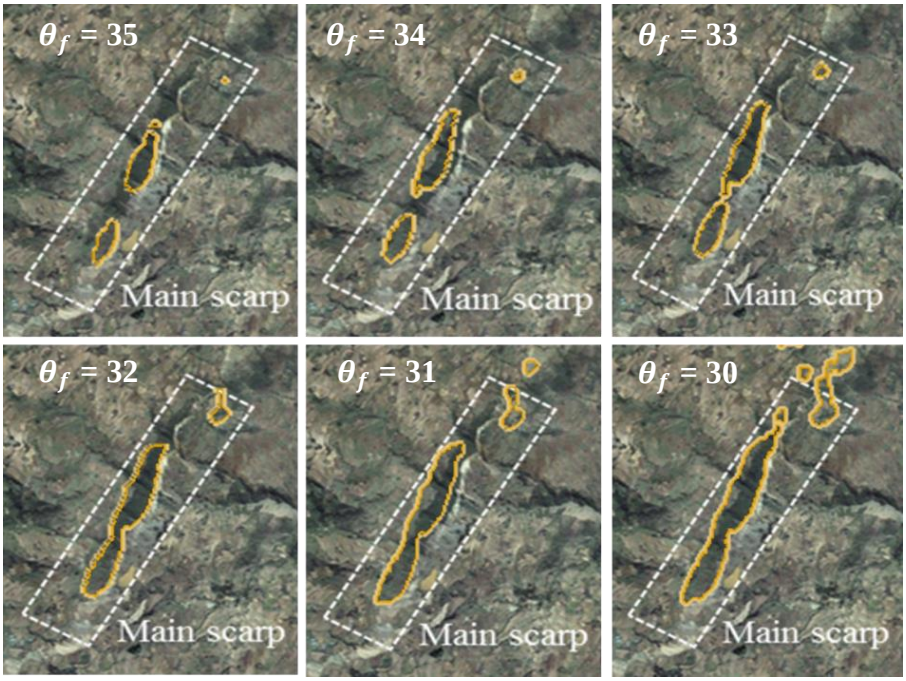

Figure 64 close up view of an overlap between simulated (in yellow) and observed (in broken white line polygons) around the main scarp of the slope disaster even area.

year 2005 landslide event though the images taken by the year 2007 satellite image did not show a clear scarps around these areas.

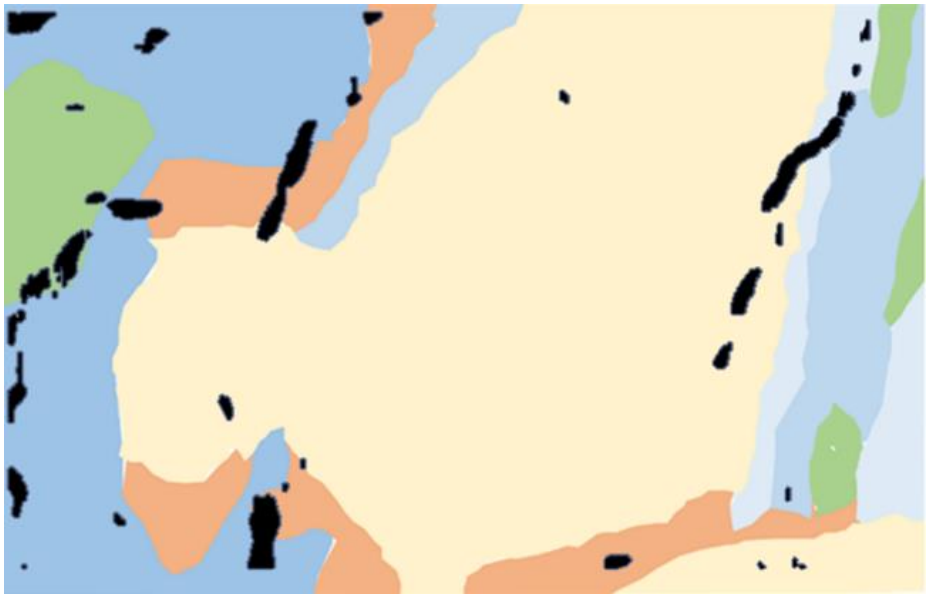

Figure 65 predicted initial slope failure area using $\theta_f = 32$ (outlined by black polygons) overlaid by the geological map of the study area.

6.1.3 Simulating surface flows of a uniformly distributed particles over the entire ranges of the region for the Kumamoto case study area

We made a simulation of flows of uniformly distributed raindrops in the Debre Sina area. Figure 62 simulated distribution of raindrops passing at the respective locations in the Debre Sina landslide area.

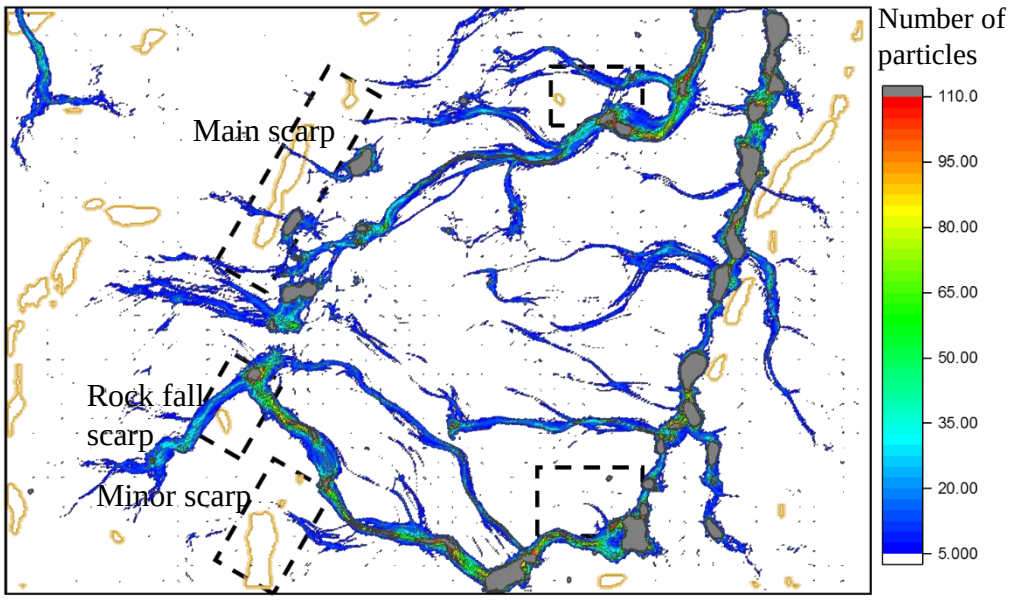

Figure 66 simulated distribution of raindrops passing at the respective locations in the Debre Sina landslide area.

Darker shades indicate greater number of raindrops passing in that location, yellowish gray polygons show location of meshes whose slope angle exceeds 32 degree and the area outlined by broken black line show the initial slope failure identified from the satellite images.

It can be seen that a large number of simulated raindrops coincide along the major drainage channels, and a relatively higher number of particles can be seen in the main and major initial slope failure area. And the final deposition area can be seen corresponding to a higher accumulation of simulated raindrops.

6.1.4 Evaluation of slope disaster risk in Debre Sina landslide area using calibrated values of material parameters

In the previous section we had demonstrated that the material parameters (n and θ_{cr}) in Bingham fluid models control the locations on which material decelerates and deposits. We calibrate the ranges of these values using visual comparison of the materials travel distance and deposition fans between the observed and simulated results in the selected cases studies in Japan. These calibrated values can be used to produce very good simulations of past events on a case-by-case basis, and many examples of successful case-specific landslide back-analyses have been documented (Loew et al 2012).

Models that are calibrated in one case study area can also be potentially well-suited to another area with a similar geotechnical conditions. We consider lower and upper bound limit values of these calibrated parameters to produce a simulations of past events in this area. The lower limit value $n = 0.05$ and an upper value of $n = 0.08$ are chosen to replicate the two extreme cases of the flows under these soil resistance parameters. And an upper limit value $\theta_{cr} = 7$ degree and a lower limit value of $\theta_{cr} = 0.5$ degree are chosen to predict the water contents of the events.

6.1.4.1 Simulated inundated area using $n = 0.08$ and (θ_{cr} =0.5 and 7 degree)

Figure 67 and Figure 68 shows the simulated inundated area shown in in blue obtaind with the parameters mentiond above overlapped in the satellite images. A lower and upper value the critical deposition angle, θ_{cr} represents a higher and lower water contents of the landslide mass respectively. And an upper limit value n describes larger bottom shear stress acting on the flowing soil-water mixture (Nakata 2016).

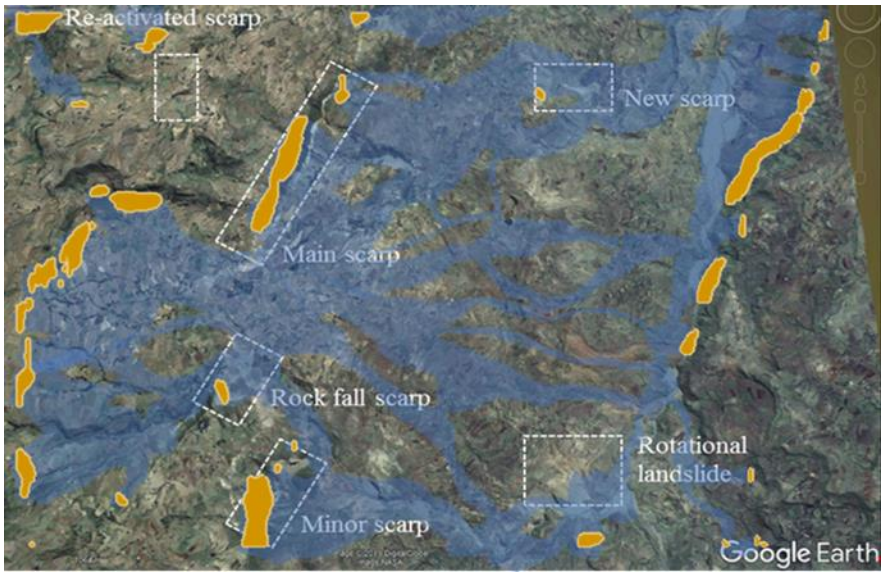

Figure 67 a replication of past slope disaster events in the Debre Sina area using calibrated parameters with upper limit value $n = 0.08$ and lower limit value θ_{cr}=0.5 degree.

Figure 67 and Figure 68 shows show a replication of the landslide event that occurred in the Debre Sina area under these lower and upper limit cases. The case for smaller θ_{cr} (highly fluidized soil mass) reproduces the event to be an excess flow which covers wide spread both in the initial slope failure area and the valley bottoms. On the other hand, the case for larger θ_{cr} reproduces a

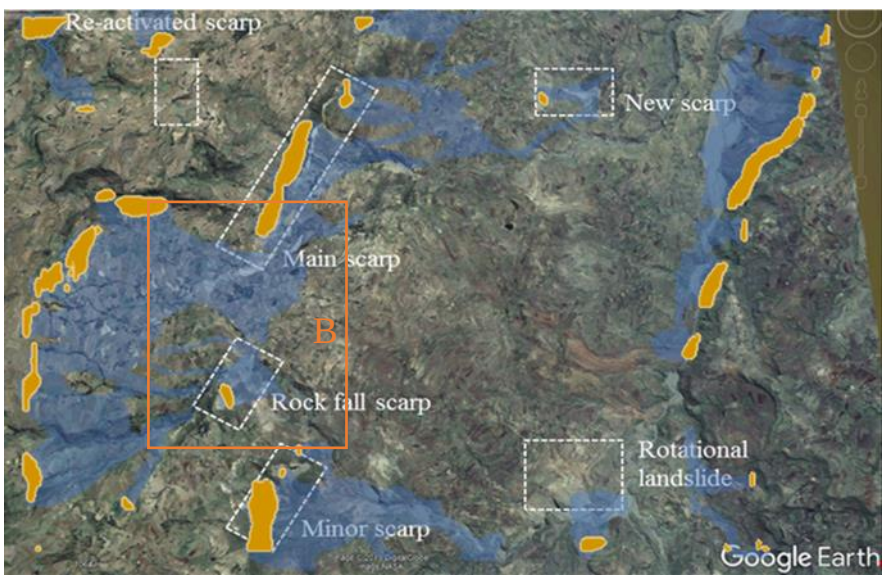

Figure 68 a replication of past slope disaster events in the Debre Sina area using calibrated parameters with upper limit value $n = 0.08$ and lower limit value θ_{cr} =7 degree.

deposition of debris flows with shorter runout distances both in the upper slope failure area and the lower river canals.

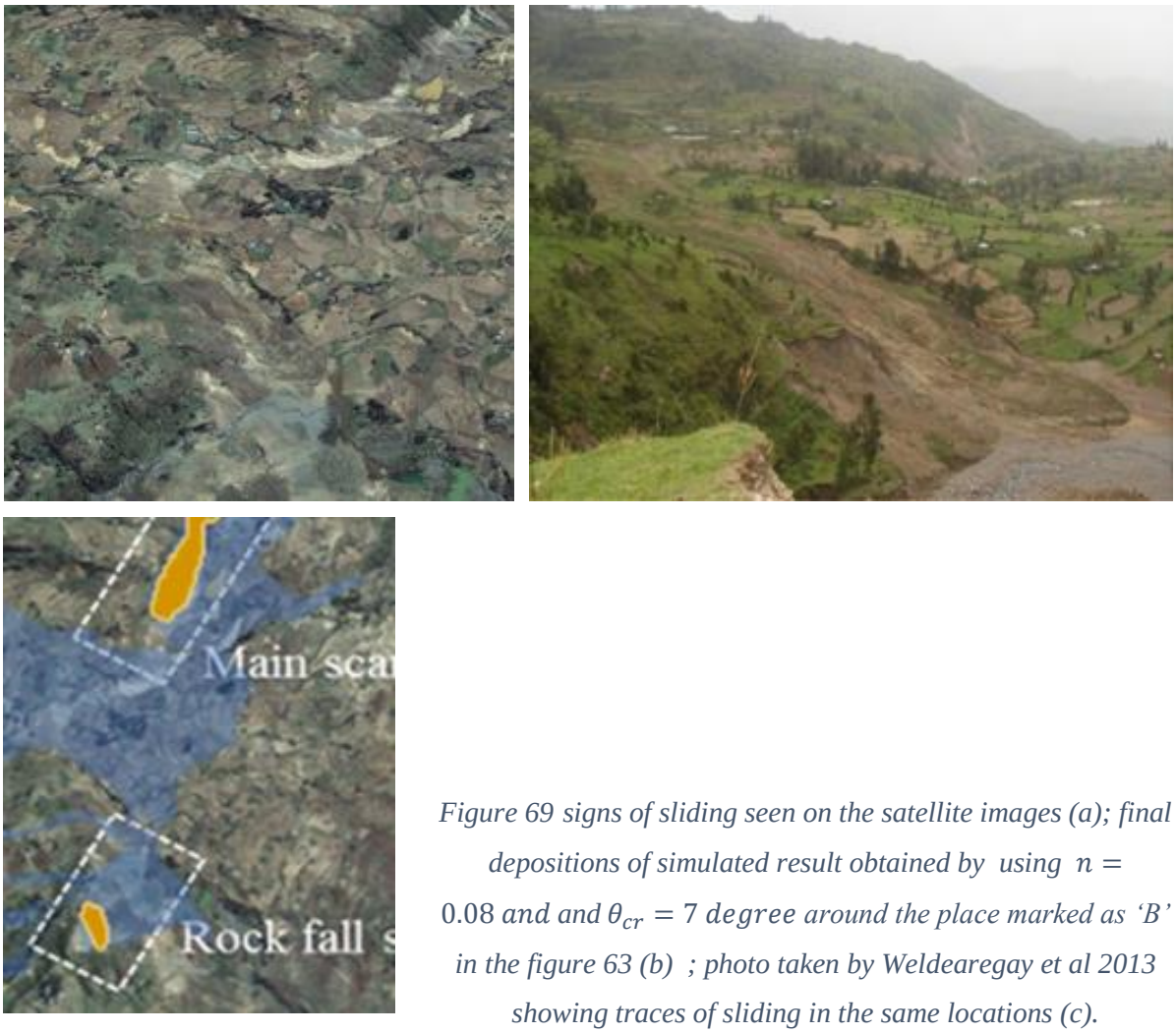

Figure 69 signs of sliding seen on the satellite images (a); final depositions of simulated result obtained by using $n = 0.08$ and and $\theta_{cr} = 7\ degree$ around the place marked as 'B' in the figure 63 (b) ; photo taken by Weldearegay et al 2013 showing traces of sliding in the same locations (c).

Figure 69 shows a satellite image and a photo taken by Weldearegay et al 2013. It can be seen that the replicated result around the place marked 'B' in dim red polygon and the observed results shown by the photo and the satellite images quite agree each other.

In both cases of the simulation results obtained by the calibrated parameters can be seen that the major and minor slope failure area well as the rock fall scarps was simulated to be under high slope disaster risks which agree with the actual event observed from the satellite images taken in the same year (2007). While the eastern side of the study area a deposition of debris mass can be seen along the drainage channel in reasonable agreement with satellite image.

6.1.4.2 Simulated inundated area using $n = 0.05$ and (θ_{cr}=0.5 nd 7 degree)

Figure 70 show a replication of the landslide event using calibrated parameters with a lower limit value of n together with lower and upper limit cases of θ_{cr}. Under the lower value $n = 0.05$, and lower value $\theta_{cr} = 0.5$ it can be seen the flows tend to be widely distributed in most of the study area. The flows also involve a larger number of surges and thus with high impact energy, and represent one of the most destructive cases. Lateral spreads usually happen on mild slopes or smooth terrain and commonly involve a horizontal displacement of the surface soils.

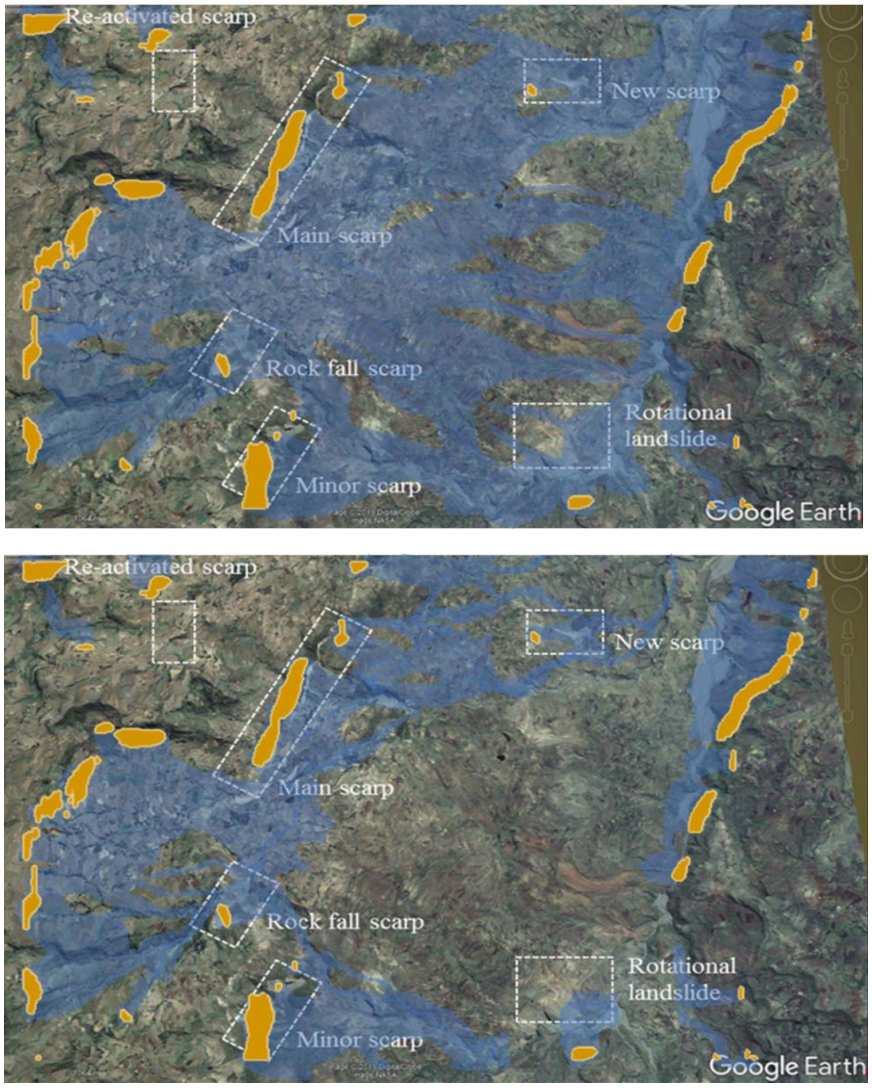

Figure 70 a replication of past slope disaster events in the Debre Sina area using calibrated parameters with upper limit value $n = 0.05$ and lower limit value θ_{cr} =0.5 and upper limit value θ_{cr} =7 degree

A recent debris sediments with larger boulder at the river floor shown in the Figure 71 by Hagos (2012) can used to verify the replicated results with larger number of surges.

On the other hand, the case for larger $\theta_{cr} = 7$ degree reproduces a deposition of debris flows with shorter runout distances both in the upper slope failure area and the lower river canals similar to the case with larger $n = 0.08$.

The several flow entrainments can be seen connecting to the main river channel that exist in the eastern side of the study area. Such an involvement of a movement of soil or rock mass combined with a general subsidence of the fractured mass of cohesive material will soften the underlying materials and make it liquefied (Varnes, 1996).

Figure 71 recent sediments of debris deposits at the river floor.

It was stated by (Hagos 2012) that the flows in this area involved also an incision effect on the stream canals and as a result a significant amount of crop lands were extensively eroded and collapsed, that ruined properties of several farmers and made them landless.

Figure 72 shows the photo taken by (Hagos 2012) which shows both major slope failure at the upper section and the final deposition places in the river channel at the lower section of the study area. According to same source the average aerial distance from the crown to the toe of the slope disaster event was estimated to be about 3km.

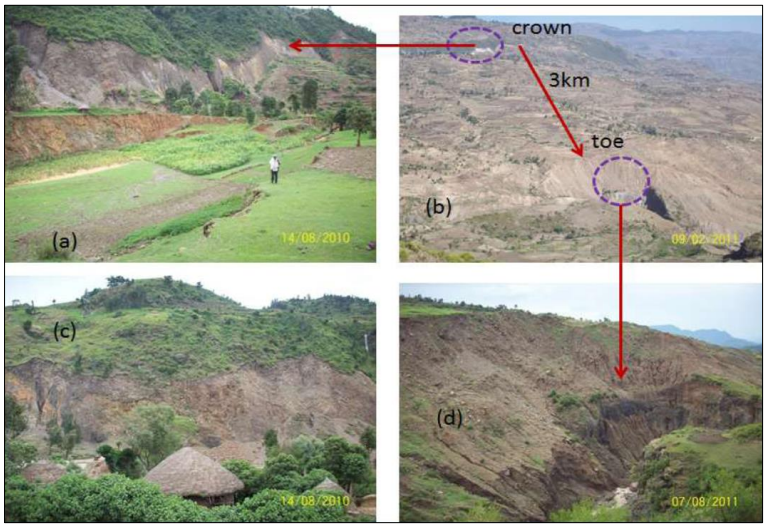

Figure 72 average aerial distance from the crown to the toe of the slope disaster event in the Debre Sina landslide area from the photo taken by (Hagos 2012).

6.1.5 Summary of the slope disaster risk evaluation in the Debre Sina area

The slope disaster event occurred in the area was large and wide to be clearly identified by the satellite images taken in the near date of the event. We used some pictures and panoramic photos

of the slope disaster event taken by previous researchers to evaluate images taken by the satellites. Identical morphological features were identified both in the pictures and in the satellite images.

We use these satellite images to make a calibration of the critical slope failure angle in order to identify the initial slope failure area. A similar approach proposed by Galas et al (2007) was adopted with addition of an index value to separately maximize between the intersection in the predicted and observed failure area and both failure and the safe area distinctly. It was found that the index values were maximum until a critical slope failure angle of 32 degree.

A relatively higher number of simulated raindrops were also found corresponding to the main and major initial slope failure area. We used this threshold value to predict the places in the eastern and western peripheries where no signs of sliding was seen on the satellite images taken in the year 2007. After estimating the initial slope failure area we used the calibrated material parameters of the model to replicate the past landslide event.

The replication of past landslide event was made using two extreme cases of the calibrated parameters, namely the lower bound values ($n = 0.05$ and $\theta_{cr} = 0.5\ deeree$) and upper limit values ($n = 0.08$ and $\theta_{cr} = 7\ degree$). The lower bound values replicated a simulation debris mass under highly fluidized condition thus the flows involved several number of surges which led to a high impact energy, that represent one of the most destructive cases. These replicated results were in agreement with the investigations made in the study area by previous researchers. In the case of upper bound values the simulation results reproduces a deposition of debris flows with shorter runout distances both in the upper slope failure area and the lower river canals.

The model can be used for both back analysis (simulation) of previous events and the forward-analysis (prediction or forecasting) of potential future events. The outcomes of the simulation results have revealed that the model reasonably reproduces the initial slope failure zone and the observed deposition area of the documented landslide event in the study area. Such an efforts will be helpful for prediction of possible future wide area slope disaster events in the neighboring areas. Although a significant achievement have been made in the calibration of the material parameters using a well-documented slope disaster event and in reproducing a past event using these calibrated parameters, several key challenges remain, including the problem with too much initial spreading and the challenge of accounting for sudden channel obstructions in the simulation of debris flows, and the sensitivity of models to topographic resolution and filtering methods (Mcdougall 2016).

6.2 Slope disaster risk evaluation of the Ankober rift margin area in Ethiopia

6.2.1 Introductions

Ankober area is located by the side of the eastern escarpment of the Ethiopian Rift Margin (EMR) at an elevation of about 2,465 meters and at a distance of 140 km northeast the capital city, Addis Ababa. The location of this area (outlined by white line polygon) is about 50 kilometers south of the Debre Sina landslide area (outlined by blue) (Figure 73). A similar seismicity in these areas were observed along the border faults of the escarpment where stress is believed to concentrate due to the lateral density and lithospheric thickness contrast between the adjacent plateau and the rift (Tiberi et al 2005). Several volcanic eruptions are also believed to be initiated in the nearby area due to the existence of one or two Paleogene mantle plumes underneath the thin crust in this area (Schilling et al 1992; Ebinger and Sleep 1998).

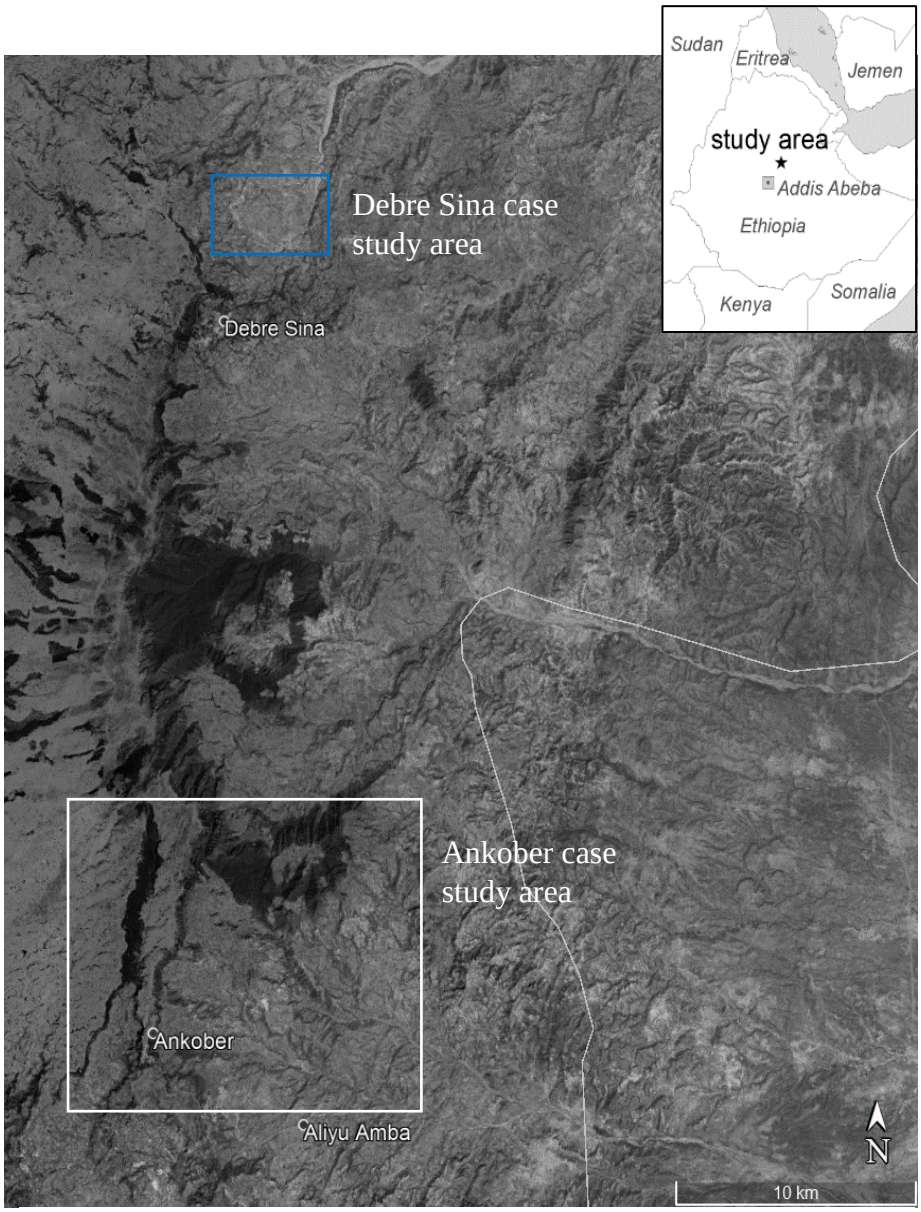

Figure 73 location map of slope disaster risk evaluation area around Ankober town in the EMR.

Under such circumstances, development of wide area slope disaster risk evaluation method is an urgent task. However, the essential difficulty is the lack of quantitative records of the previous landslide events. In-situ mechanical test records of the geomaterials are also rarely available. Therefore, an applicable evaluation method should contain the least number of parameters that can be roughly estimated without detailed material data.

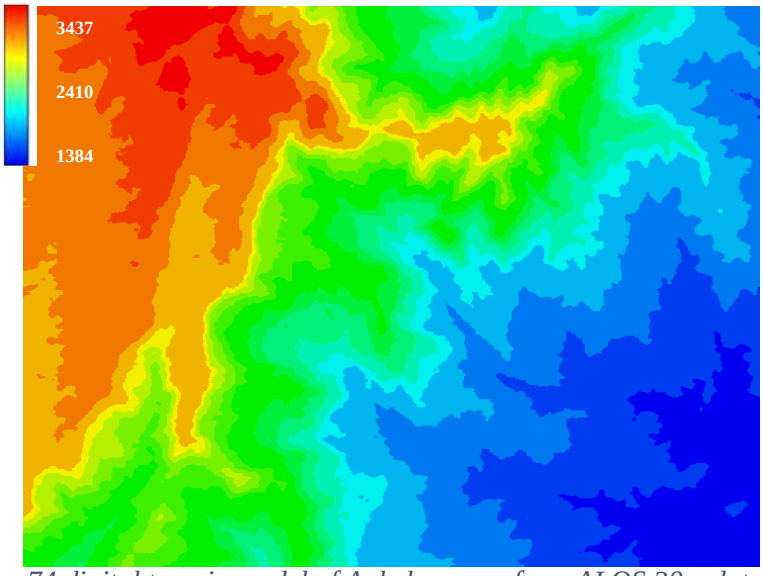

Figure 74 digital terrain model of Ankober area from ALOS 30m data source after smoothening and interpolation into 15m intervals.

A digital terrain model of the study area (Figure 74) was prepared from ALOS 30 meter mesh freely available data. Adjacent average smoothing was done by adding points along the path so that the model fits a smooth function along the points after interpolation into 15m intervals. We consider a wide area (outlined by white line polygon in the Figure 73) which comprises 16 by 14 kilometers of east-west and north-south distance, respectively. The map shows morphological trends with high elevation around 3400m in the western peripheries and decreases down to about 1400m above sea level in the eastern side. Extra high values are shown in the southwestern side and lesser low values are spread in the northeast border of the area. Medium elevation values are

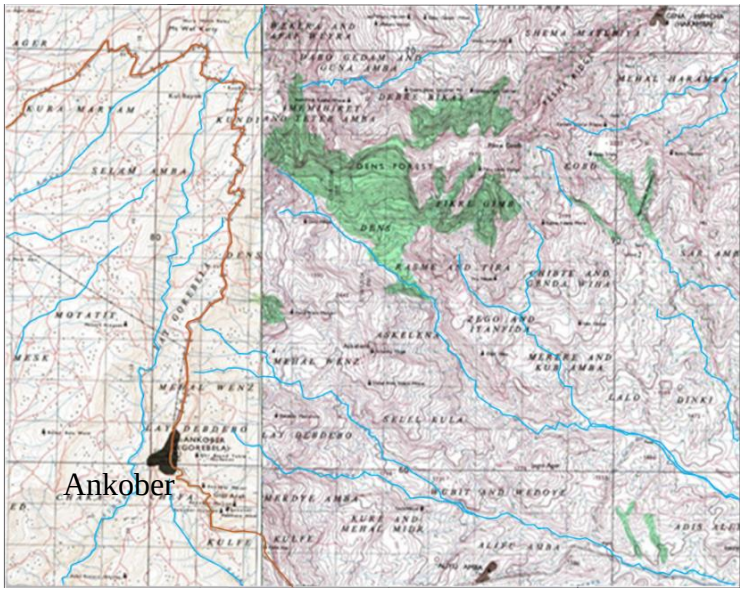

Figure 75 topographic map of Ankober area from Ethiopian Mapping Agency.

widely distributed in between these regions around the middle of the study area and in its most southeastern peripheries.

Figure 75 shows the 50, 000 scale topographic map of study area obtained from Ethiopian Mapping Agency. The map shows ground reliefs such as landforms and terrains, drainage channels as well as forest covered areas. We used the topographic map to identify the places that necessitates to be protected primarily such as villages, roads, and forest covered areas. In several cases occurrences, slope failure disasters causes surface erosion of the fertile soil covers and results in deforestations.

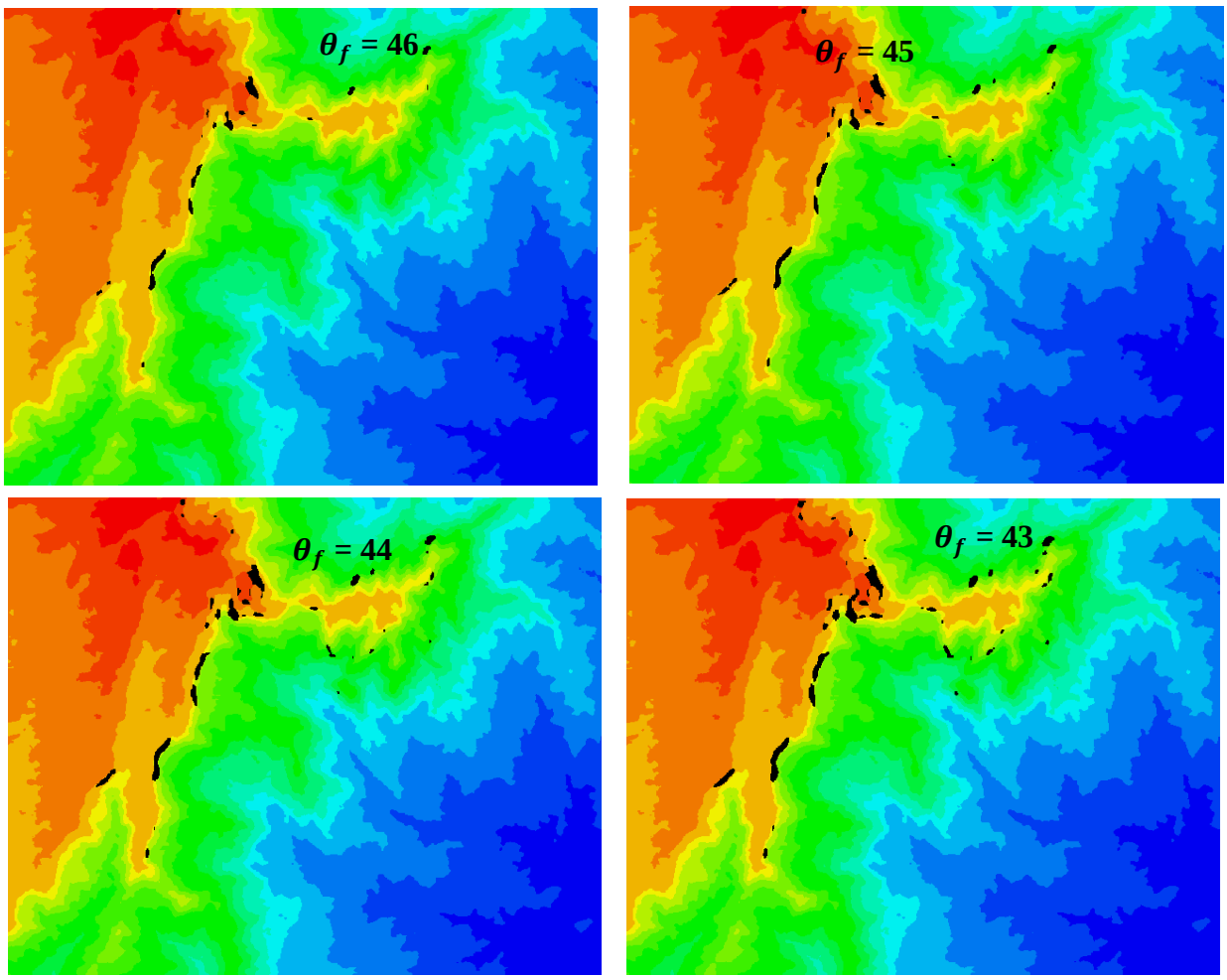

Figure 76 location map of initial slope failure area predicted only by slope angle using θ_f value from 43 to 46 degree.

6.2.2 Slope unit-based estimation of the initial slope failure area

The required data including the unsaturated and saturated bulk density of the soil mass as well as porosity n of the surface soil was not available to compute the slope angle corresponding the safety

factor value of $F_S = 1$.Therefore, we set a higher critical slope failure angle θ_f to predict the initiation area. This holds true because the most likely failure places happen in steep slopes.

Moreover, slope angle stands to be one of the most important factors controlling the stability of slopes (Ercanoglu and Candan 2002). It has been verified also that in many paces larger part of the area of severe destruction was on the steep slopes (Soeters and Van Westen 1996).

Figure 76 shows the locations of columns of slopes identified only by a given slope failure angle from 41 to 46 degree. Input data needed for wide area slope disaster risk evaluation includes

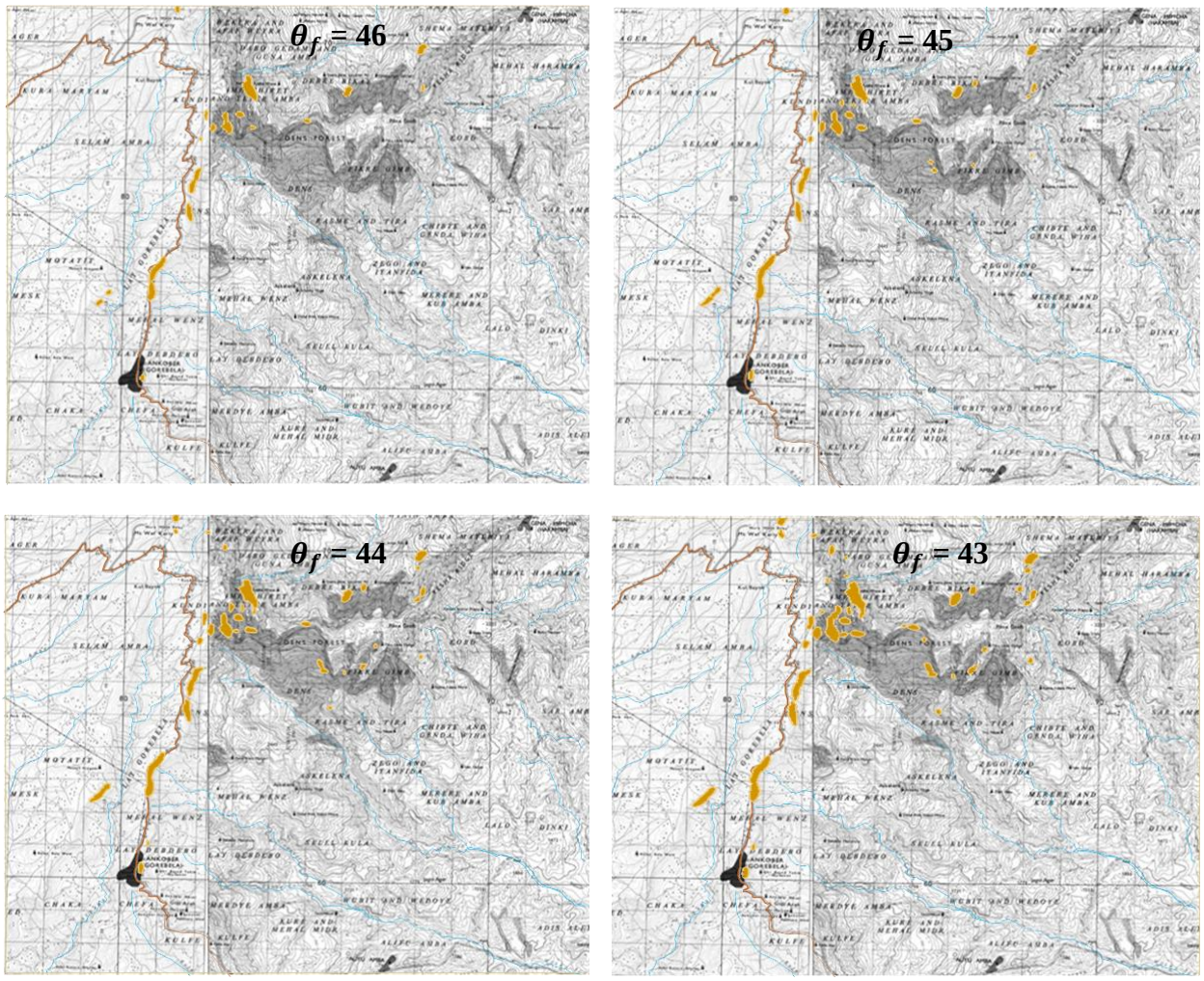

Figure 77 location map of dangerous slope failure area predicted only by slope angle (outlined by gray color solid polygons) overlaid with the topographic map of Ankober area.

topography, geology, in situ geotechnical tests as well as information about land use and hydrology. However it is only in an ideal case will all types of data be available. It can be seen that a large number columns of dangerous slopes are shown both on the hill side in the western and

nearly the central places in the study area; and around the lower altitude area in the eastern peripheries. Relatively wide columns of slope appear in the western side of the area around the medium elevation value places quite nearby to the center.

A most straightforward approach for wide area slope disaster zonation includes field surveys, aerial photo interpretations, and a data base of historical occurrences of landslides in the given area. We combined identified dangerous slope failure locations with the topographic map of the study area (Figure 77) so that it helps to make slope disaster zonation in this area. Such a vulnerability zonation is essential for disaster management and control in mountainous regions. The eastern and western side of Ankober town, the road that connects to the capital city and the forest cover area are found to be near the predicted dangerous slope failure zones.

6.2.3 Simulating surface flows of a uniformly distributed raindrops in the Ankober area

We made a simulation of flows of uniformly distributed raindrops in the Ankober area. Figure 78 shows the distribution of the number of particles passing in the respective location of the study area.

Darker shades indicate greater number of raindrops passing in that location, yellowish gray polygons show location of meshes whose slope angle θ_f exceeds 43 degree and blue lines show the drainage channels obtained from topographic map of the study area.

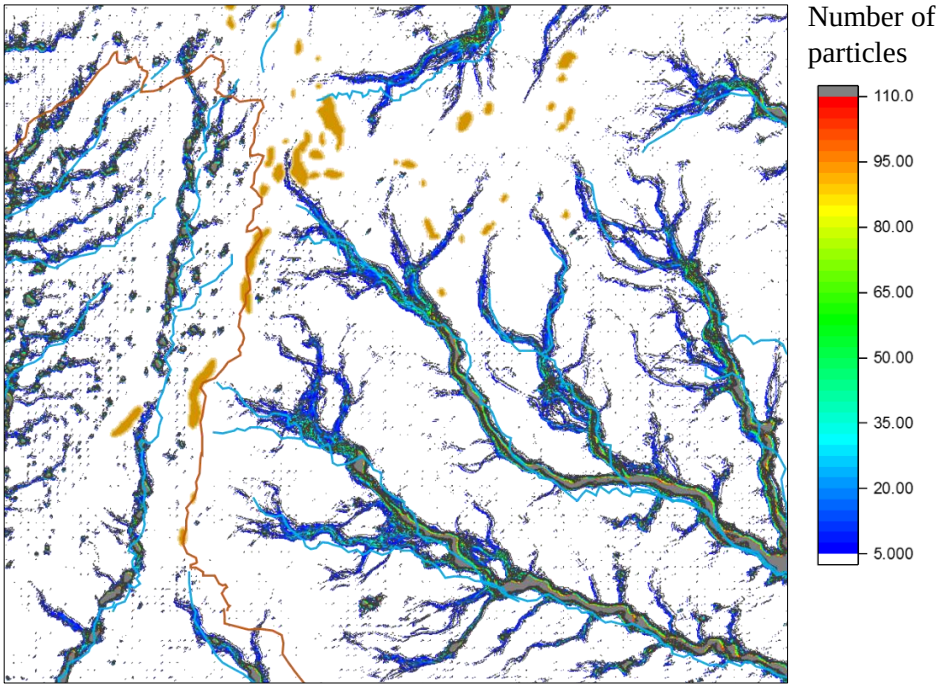

Figure 78 simulated distribution of raindrops passing at the respective locations in the Ankober rift margin area.

It can be seen that a large number of simulated raindrops along the major drainage channels. The concentration of the raindrops increases towards the eastern most sides of the study area which shows a bigger risk of debris flow deposition fan.

6.2.4 Evaluation slope disaster risk in Ankober area using calibrated values of the material parameters

From Figure 77 it can be seen that there are much steeper slopes found in this region than the previous case study area, which implies that the shear strength of the geo-materials in this area is higher in this area. Considering this condition, θ_f=45 (deg.) was set in the simulations. Flow spreading simulations were made using the two extreme cases of the calibrated parameters, namely the lower bound values (n=0.05 and θ_{cr}=0.5 degree) and upper limit values (n=0.08 and θ_{cr}=7 degree).

6.2.4.1 Simulated slope disaster inundated area using lower bound values ($n = 0.05$ and θ_{cr}=0.5 degree)

A lower bound values of the material parameters represents a higher water contents of the landslide mass and lower bottom shear stress acting on the flowing soil-water mixtures.

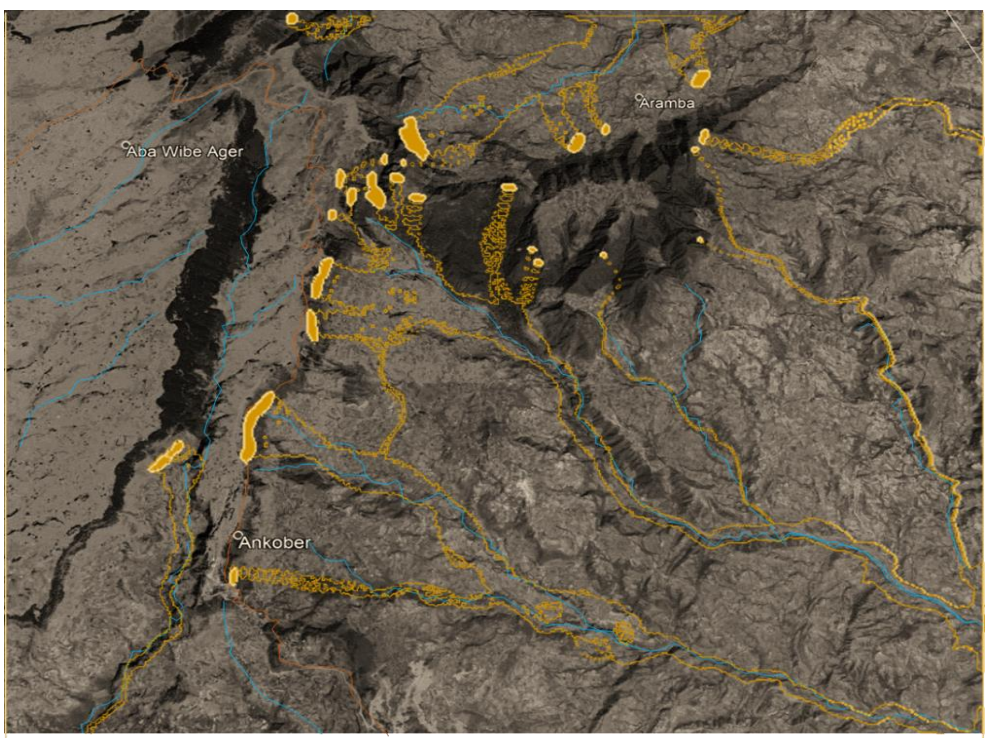

Figure 79 simulated slope disaster inundation (in yellowish color in the Ankober area using calibrated parameters with lower limit values $n = 0.05$ and $\theta_{cr} = 0.5$ degree overlaid in the satellite image of the study area.

Figure 79 show a simulated slope disaster

inundation in the Ankober area using calibrated parameters with a lower limit value of $n = 0.05$, and $\theta_{cr} = 0.5$ overlaid with the satellite image of the study area taken in the year 2019. The predicted imitation area are shown in solid fill yellowish color polygons. And the simulated flow inundations are shown in transparent yellowish color polygons.

The flow paths in downstream side agree well with the river system shown in Figure 75 while the upstream inundated areas are widely spread into residential area. It can be seen the flows remain widely distributed in most of the drainage channels in the eastern side of study area. The flows also involve a larger number of surges and thus with high impact energy, and represent one of the most destructive cases.

6.2.4.2 Simulated slope disaster inundated area using upper bound values ($n = 0.08$ and θ_{cr}=7 degree)

In practice an upper limit value n describes larger bottom shear stress acting on the flowing soil-water mixture and a higher bound values of the critical deposition angle represents a lower water contents of the landslide mass. Figure 80 show a simulated slope disaster inundation in the Ankober area

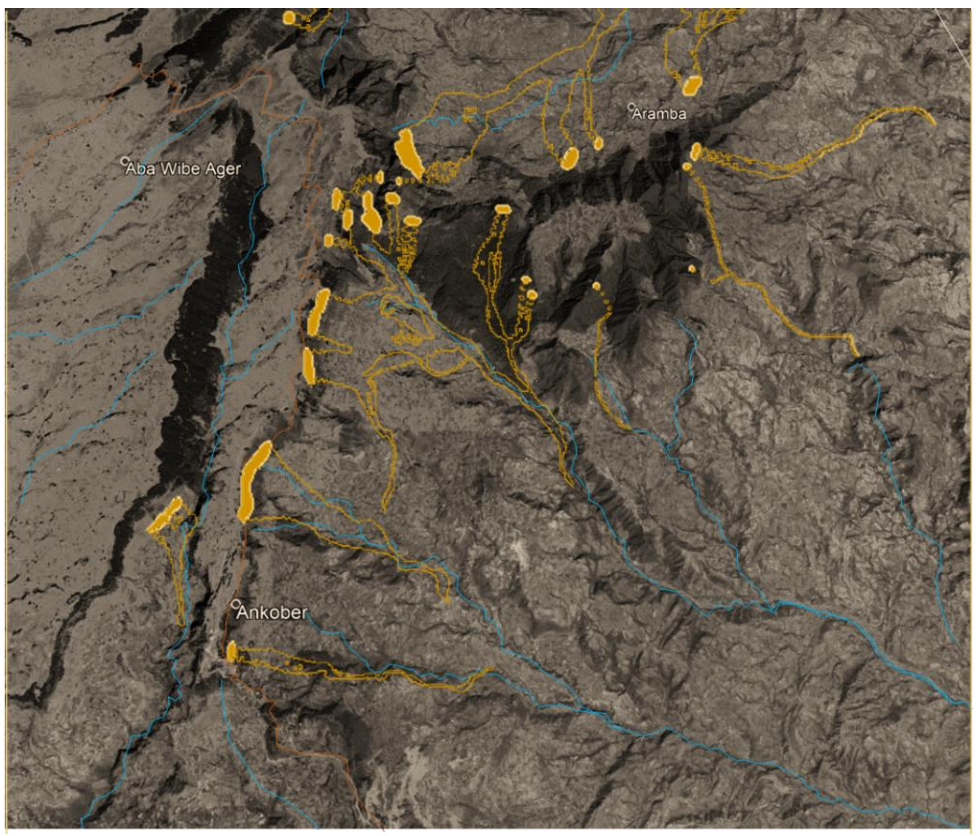

Figure 80 simulated slope disaster inundation (in yellowish color in the Ankober area using upper bound values of calibrated parameters $n = 0.08$ and $\theta_{cr} = 7\ degree$ overlaid in the satellite image of the study area.

using calibrated parameters with an upper limit value of $n = 0.08$, and $\theta_{cr} = 7$ overlaid with the satellite image of the study area taken in the year 2019. The predicted inundations area are shown in solid fill yellowish color polygons. And the simulated flow inundations are shown in transparent yellowish color polygons. In the case for larger values the calibrated parameters a deposition of debris flows with shorter runout distances both in the upper slope failure area.

In both cases of the simulation results obtained by the calibrated parameters lower and upper bound values, it can be seen that the identified places such as villages, roads, and forest covered area that necessitates to be protected primarily were simulated to be under high slope disaster risks.

Moreover, from the overlap of the simulated results and the satellite images it can be seen that the most possible debris flows occurrence could be in the flood plains covered with trees or heavy brush, who's Manning's coefficient *n* is about 0.1.

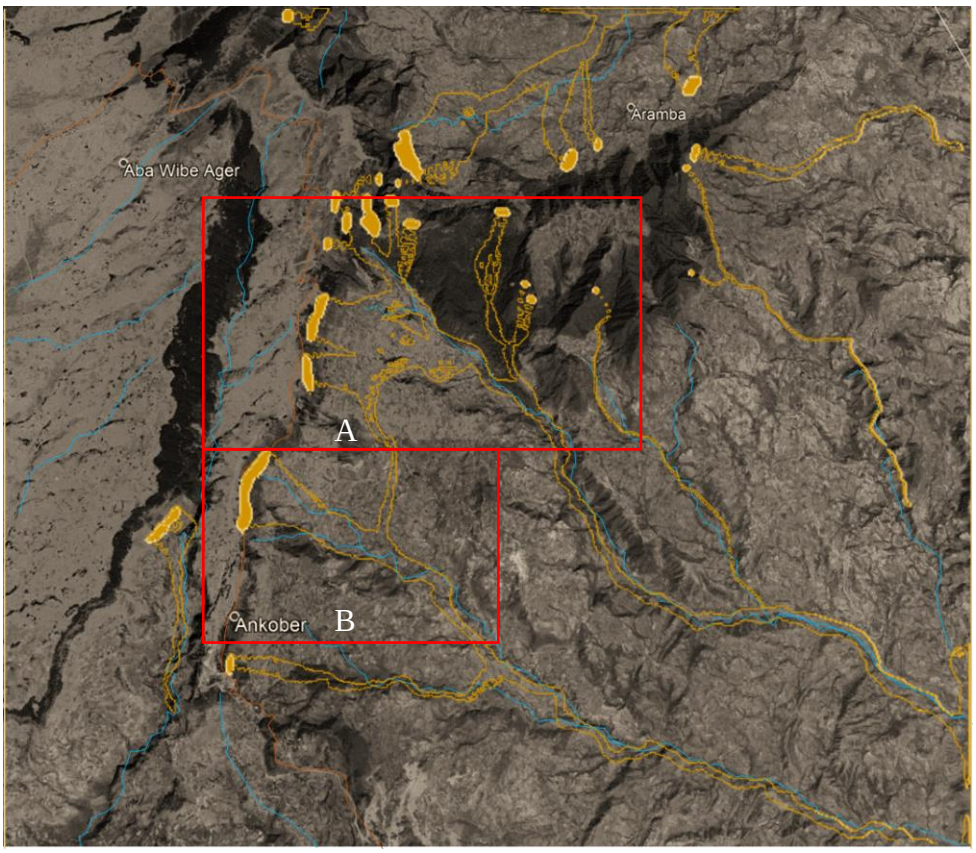

Figure 81 simulation of slope disaster event using Manning's coefficient n value 0.1 and θ_{cr}=0 (deg.) for a most dangerous case.

On the other hand, the critical angle for flow θ_{cr} depends highly on the water contents of the landslide mass, which is difficult to identify in advance. Therefore, we assume the most dangerous case and set to θ_{cr} =0 (deg.).

Figure 81 shows the simulation result obtained using these material parameters. The close-up views for areas A and B are shown in Figure 82, where simulated inundated areas are overlapped in the satellite images.

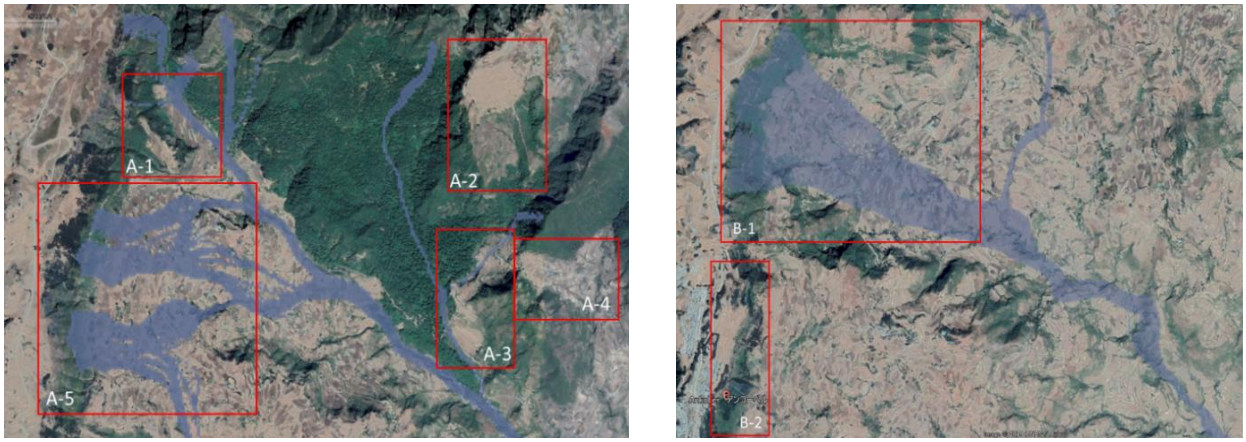

Figure 82 close-up views for areas A and B in Figure 81.

In area A, we can observe the traces of several previous landslides (A-1, A-2, A-3, A-4) from the satellite image. Since some of the simulated inundated areas cover such traces, which indicates that they are still potentially dangerous. On the other hand, area A-5 does not have such previous landslide traces, but the steep slope in the west part of the area has relatively high risk of landslides. Moreover, they may lead to wide inundated area as shown in the simulated one, which covers relatively large number of houses. The simulation in area B also suggests wide inundated area covering certain amount of houses (B-1). The area B also contains the town of Ankober town in the southwest part, but it is located in the highland and the inundation risk is not high. The major risk of the town may be the landslide at the east edge of the town (B-2).

Figure 83 shows the time history of the maximum and average flow velocity in the simulation.

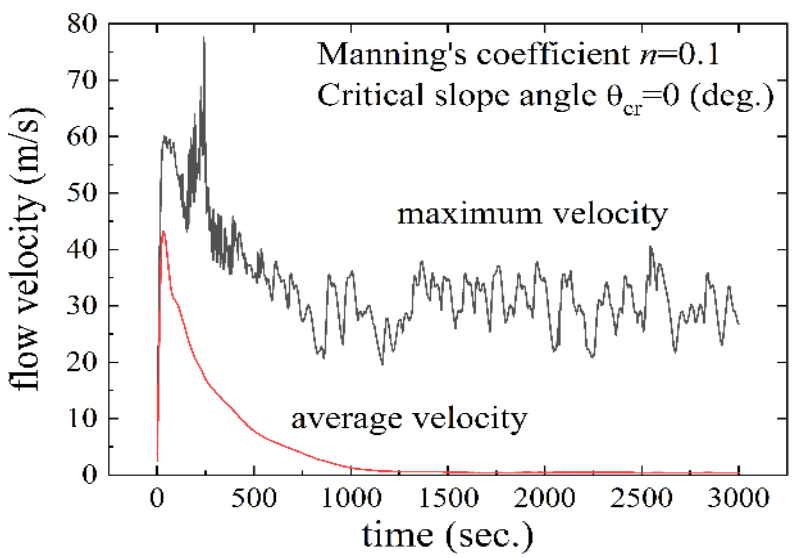

Figure 83 time history of the maximum and spatially averaged velocity of the flowing mass.

Since the angle of slope at failure is very steep more than 45 (deg.), the flow velocity at the initial stage is much higher than the previous areas. The average flow velocity goes to zero at around t=1000 (sec.), but some part of flow runs fast even after t=3000 (sec.) because the simulation adopted θ_{cr}=0 (deg.) (with zero yield stress). Such cases are common when the debris materials flow through gullies with comparatively quick changes from steep to shallow topographies. The mean velocity of the predicted flow was found to be quite large value compared to the mean velocities of common debris flows under a channel gradients varying from about 40° in the starting zones to about 3° in the deposition zone (Hutter et al 1994).

6.2.5 Summary of the slope disaster risk evaluation in the Ankober area

Ankober area is located at the edge of the eastern side of the EMR closer to the Debre Sina landslide area. It is characterized by similar seismicity and geological characteristics. Both the Ankober and the Debre Sina area are near to the Afar Triangle where several old and recent volcanic eruptions are believed to exist due to existence of one or two Paleogene mantle plumes underneath the thin crust in this area (Schilling et al 1992; Ebinger and Sleep 1998). These conditions urge for a search for a wide area slope disaster evaluation methods.

A quantitative records of the past landslide events is not available in the Ankober area. Moreover, in-situ mechanical test records of the geomaterials are also rarely available. We used the topographic map of the study area together with the satellite images taken in the year 2019 to identify the places that necessitates to be protected primarily such as villages, roads, and forest covered areas. We identify also forest covered fertile areas that need to be most protected because slope failure disasters causes surface erosion of the fertile soil covers and results in deforestations in several cases.

Due to absence of the required data including the unsaturated and saturated bulk density of the soil mass as well as porosity n of the surface soil was not available to compute the slope angle corresponding the safety factor value of $F_s = 1$. Therefore, we set a higher critical slope failure angle θ_f to predict the initiation area. From the overlap of the predicted slope disaster area and the topographic map it was seen that the eastern and western side of Ankober town, the road that connects to the capital city and the forest cover area are found to be near the predicted dangerous slope failure zones.

Flow spreading simulations were made using the two extreme cases of the calibrated parameters, namely the lower bound values (n=0.05 and θ_{cr}=0.5 degree) and upper limit values (n=0.08 and θ_{cr}=7 degree). In both cases of the simulation results obtained by the calibrated parameters lower and upper bound values, it was seen that the identified places such as villages, roads, and forest covered area that demands to be protected primarily were simulated to be under high slope disaster risks. Moreover from the overlap of the simulated results and the satellite images, it was found that the most potential occurrence of a debris flows could be in the flood plains and the drainage channels covered with trees or heavy brush, whose Manning's coefficient *n* is about 0.1.

A most dangerous case of a flow was also assumed and θ_{cr} was set to a zero value. The results found using these material parameters showed a wide inundated area having a high value of velocity and it covers relatively large number of houses.

The predicted flow velocity at the initial stage was much higher than the previous case study areas due to a comparatively steep slope failure angle value more than 45 (deg.) occur in this area. The mean velocity of the predicted flow was found to be quite large value compared to the mean velocities of common debris flows under a channel gradients varying from about 40° in the starting zones to about 3° in the deposition zone (Hutter et al 1994). In general, the results suggest the necessity of a further investigations in this area.

7 Conclusions and recommendations

7.1 Conclusions

The need for evaluation of slope disaster risk is a crucial task in all places where the vulnerability to the condition of a slope disaster incidences exists. All over the world, slope disaster occurrences cause loss of lives and damages to properties and infrastructures especially in mountainous terrains. In the period between 2004 and 2016 alone 55, 997 people were killed in 4862 distinct non seismically triggered occurrences all over the world according to data collected by Froud et al 2018. The majority of these landslide events involved a single failure slopes having wide area spatial distributions with high areas of incidence in the cities.

The situation in Ethiopia is not different. In a recent occurrence alone, at least 41 people were killed due to a heavy rain triggered slope disaster event in a place called Kindo Didaye district on

May 2016. The situation is aggravated due to the existence of a wide area tectonically active rifting system (EMR) that cross the country from northeast to southwest. This severe condition of slope disaster risk necessitates a comprehensive and diversified methodology of forecasting and evaluating these problems.

Depth-integrated (or shallow water) formulation has been widely used in debris flow and river engineering simulations so far (Kalkwijk and De Vriend 1980, Hervouet 2007). Recently, this formulation has been applied into particle method (Pastor et al. 2009, 2014). A simplified version of this method called Depth Integrated Particle Method (DIPM) had been used by previous researchers in the division the Geotechnical laboratory under the department of the Energy and Mechanics Engineering of the University of Tsukuba. Nakata (2017) made a pioneering work on evaluation of wide-area landslide hazard using DIPM and GIS applying to two wide-areas as a case studies: the Nova Friburgo (6.72 km by 4.5 km) in Brazil and the Hofu (4.75 km by 2.50 km) in Japan. And a mixing model based on a two-step evaluation scheme was proposed together with DIPM by Zhang (2015) to quantitatively evaluate the debris flow hazards in Zhouqu and Wenchuan earthquake stricken areas. However, previous researchers did not includes a precipitation simulations which is essential to locate the water catchment area where most of the erosions and sediment processes occurs. This helps to identify a potential soil saturation area and thereby contributes in the delineation of the initial slope failure area and the maximum budding debris flow affected drainage channels.

The methodology implements a twofold strategy: first we assess a slope disaster risk in the given area by evaluation of the stability condition of the slopes using the available records. There are several classical ways to evaluate the stability of a slope and yet the subject is arguably the most complex and challenging sub-discipline in geotechnical engineering. We used a 1D slope formula to compute factor of safety (F_S) of a slope with the assumption that the critical slope failure angle can be roughly evaluated from the available record of the saturated and unsaturated bulk density and the depth of the ground water of the unstable mass under consideration.

Secondly, once a surface soil mass fails to be stable and starts to slide, usually it will be mixed up with masses of liquids and the flow behavior of the mixture is strongly influenced by its material properties such as size distribution of geological grains (from micron scale to meter scale), grain shape and crushability, water contents, etc. However, there are no universal constitutive laws

governing landslides that are straightforward to incorporate into numerical models (Pastor et al. 2012). Moreover, what is necessary for wide-area risk evaluation of landslide hazards is not a sophisticated and highly accurate constitutive models but rather primitive ones with the smallest number of material parameters that can be easily identified. Therefore, a simplifications of constitute models appears to be a reasonable approach towards a systematic application of simulating the deposition process of debris flows.

A simplification of a complex 3D problem into a 1D numerical model for unsteady flow called DAN (Dynamic ANalysis) was formulated for modelling post failures (Hungr 1995). However, the model can only be used for cases where the rheology is constant and known in advance due to the model basis on a generalized rheological kernel which needs to be calibrated for a particular landslide type. Another approach with a relatively detailed flow behavior based on depth-averaged model equations and an advanced numerical integration scheme making use grids which moves with the deforming pile was proposed by Koch et al (1994). However, the implementation an Finite Difference Method (FDM) for the numerical solutions suffer a restriction of limited ability to determine time series of complete contour plots of the evolving topographies.

Moreover, an FDM uses a topological square network of lines to construct the discretization of the PDE which is a potential bottleneck of the method when handling complex geometries in multiple dimensions. This issue motivated the use of an integral form of the Partial Differential Equations PDEs and subsequently the development of the finite element method (FEM) and finite volume Method (FVM) (Peiró et al 2005). However, in all the three methods, the problem spatial domain is discretized into meshes named as elements in FEM, grids in FDM and volumes in FVM. Such discretization of the spatial domain of the problem into meshes impose difficulties in handling problems related to mesh distortions. To surpass this problem mesh free methods have been implemented. Among them the longest established and has matured compared with other meshless methods is the smooth particle hydrodynamics (SPH). Unlike Eulerian approach (fixed frame of reference) SPH is a purely based on a Lagrangian approach (moving frame of reference) in which particles carry field variables and move with the material velocity. Due to its Lagrangian formulation SPH has advantages in handling a large deformation compared to other grid-based numerical methods. And its adaptive nature allows to handle complex geometries without any difficulties.

We have developed a simple depth-integrated particle method (DIPM) which is a simplification of an SPH. The model is based on depth-averaged shallow flow equations solved on a set particles obtained from the Digital Terrain Model (DTM) constructed using Grass GIS open source application software. The resultant forces acting on each particle is considered to be similar to the forces acting on the columns of soil in a limit equilibrium slope-stability analysis in which the gravity force and the hydraulic pressure are the driving forces and the resistance force to motion comes from the basal shear stress computed from Manning's formula combined with the equation of steady and uniform flow. The hydraulic pressure was determined by the interaction between the neighboring particles and thus it was affected by mesh size of a DTM used to acquire information about the topography of the area of interest.

Previous researchers in this field construct a DTM from stereo-photogrammetric method from images taken by the Panchromatic Remote-sensing Instrument for Stereo Mapping (PRISM) sensor onboard the Advanced Land Observation Satellites ALOS satellite (Nakata 2016 and Zhang 2019). Space-borne earth-observation sensors provide new perspectives in DTM generation for virtually any location on earth (Huggel et al 2008). In this study we construct a DTM from worldwide digital sources offered at 30-m and 12.5-m resolutions. The ALOS 30m was obtained from Japan Aerospace eXploration Agency (JAXA). A relatively smaller mesh size DTM at 12.5-m that has a higher resolution was obtained from ALOS-PALSAR (Phase Array type L-band Synthetic Aperture Radar) developed (Alaska Satellite Facility (ASF), 2015). ASF has produced products at both 12.5-m and 30-m resolutions. Another freely available DTM was also derived from Google earth application by extracting elevation values using free software called TCX converter.

ALOS 30-m was used for wide area slope disaster risk evaluations in the case study areas in Ethiopia after evaluating its accuracy by comparing with a 10-m resolution DTM constructed by stereo-photogrammetric method from images taken by ALOS. A frequency and contour lines distribution maps as well as a cross-sectional view at some selected profiles were used to compare the ALOS 30-m and google earth DTM with ALOS 10-m a commercially available DTM source. The resulted showed a similarity between the ALOS 30-m and ALOS 10-m DTMs. Particularly, the similarity of the cross sectional views at a longer length profiles showed the equivalence of the resolution of the DTM on regional level. However, at a closer view the cross-sectional profiles the ALOS 30-m DTM showed some local flat planes problems which was corrected by a simple

adjacent average smoothing by adding points along the path so that the model fits a smooth function along the points.

A similar comparison was made between the ALOS 30-m, ALOS 12.5-m and airborne survey 1-m DTM using a frequency and contour lines distribution maps as well as a cross-sectional view at some selected profiles and it was seen that the terrain correction made by Alaska Satellite Facility enhanced the resolution of the ALOS 12.5-m DTM.

We also made a comparison between the ALOS 12.5-m and airborne survey 1-m DTM its ability in reproducing actual events using the numerical models. The results of the model runs using the two DTMs was compared on the basis of identifying each surge of the debris flow and on the basis of an agreement in the depositional patterns with observations. The result of the model run with airborne survey DTM covers most of the flows with appropriate bending of the channel. Whereas in the case the result obtained with the run using freely available DTM the number of surges and the pattern of deposition considerable differ.

The comparison was made on a selected local area about 2 square kilometers and result showed that for such a local area investigations with short runout distance of a debris flow and a total area having less than a one and half kilometer length and width, the performance this DTM can be limited only to give an approximate overview about the area of inundation and can serve also as a first estimates of the areas potentially affected by mass flows. However, for a wide area incidents, with a deep-seated slope failure that usually happen in many places of Ethiopia, having several kilometers width and lengths, the DTM from ALOS 30-m after a correction of the local flatness and from ALOS 12.5-m without need of correction was found to be capable to be used in the evaluation of slope disaster risks using a calibrated material parameters.

There are several approaches to calibrate the material parameters of numerical models. We used a calibration technique based on a visual comparison of the main external aspects of landslide behavior such as how far do the debris flow travel and how wide do the flow spread in the deposition fan. Though this approach is subjective, it is simple to implement when the model contains few adjustable parameters that dominate different characteristics of the simulation results.

Depth integrated particle model provides an advantage of selecting the material parameters of the model based on a calibration made through applications into several case study areas affected by previous landslide events. Such a calibration approach is carried out routinely in geotechnical

practice with limit equilibrium slope stability analyses (e.g., back-analyzing a failed slope to help constrain shear strength values) (Mcdougall 2016).

The initial slope failure area need to be determined in advance in order to calibrate the flow parameters (n and θ_{cr}). This is due to the flow inundation results are sensitive to the initial mass discharges of the debris flow. Estimation of a potential initial slope failure hazard area using 3D slopes stability analysis was done using historic landslide for the Kumamoto debris flow affected area (Wang et al 2006). A 1D slope stability analysis was applied here to estimate the critical failure slope gradient values of the dry and saturated soils in both Hofu and Kumamoto landslide affected areas.

However, the locations of mesh values in the respective critical slope gradients for dry soil (49.57 degree for Hofu case) and (49.5 degree for Kumamoto case) were less that 1 percent in both of the DTM, obtained from high resolution airborne survey (for Hofu case) and from feely available data source (ALOS 30m mesh) (Kumamoto case). Moreover, for the Kumamoto case study area, the slope failure location identified by using slope inclination and the potentially dangerous slopes estimated by Wang et al. (2006) using elliptic sliding surface method was not in agreement with the actual slope failure area.

Simulations of flows of uniformly distributed raindrops were made for the Hofu and Komamoto area. In both case of the study area a large number simulated raindrops were accumulated in the final deposition fan of the debris flow affected area. A strong correspondence between both in the sinuosity and pattern of depositions were seen between the simulated large number of raindrops and the path of the debris flows in both study areas. The result had also shown a difference between the eastern and western part side of correspondence between simulated raindrop distributions in the Hofu area.

Therefore we employ a user defined assignment of the initial slope failure area, for a debris flow involving a single surge (the Kumamoto area). However, due to the inconvenience of user defined assignment for a debris flow with multiple number of surges (Hofu case), we use a critical slope failure angle, θ_f to locate these places. From the sensitivity analysis between the initiation area obtained using some slope inclination and the actual slope failure area, it was able to select 40 and 42 degree for the western and eastern side respectively, to locate the initial slope failure zone in this area.

For the Komamoto case study area it was seen that the case for smaller n (smaller bottom shear stress) leads to an excess flow acceleration and results in the too much deviation from the path of valley bottom in the upper stream. On the other hand, in the downstream deposition fan, the simulated inundated width is narrower than the observed one for larger n. Using a comparison at time history of the maximum velocity of the flowing mass with the evaluation by Mizuno et al. (2003) and looking at Table 1, a lower and upper bound value of (n and θ_{cr}) was estimated to be in the range (0.05 to 0.10, 5 to 7 deg.) for the debris flow affected area in the Kumamoto prefecture. However looking at Table 1, the Manning's coefficient differs in different ground surface materials, and it can be recommended to set a larger value in the upstream and a smaller value in the downstream based on information obtained from the aerial photo.

Due to the problem of too much initial volume of discharge predicted using only slope inclination values, we considered only certain main surges in the western eastern side of the study area in the Hofu case. Looking the model results obtained using n value of 0.03 to be much wider (lateral) width for the case of both the surges and looking n value of 0.08 to be much narrower width for the case of these surges it was able to set the lower and upper bound for n value to be in these two values. However, it was seen that the variation of the simulation result using these two parameters was not independent of each other. Generally, a range values between (0.05 to 0.08, 0.5 to 7 deg.) was estimated to be fitting for the western part of the study area. And a range values between (0.05 to 0.08, 0.5 to 4 deg.) was estimated to be fitting for the eastern side of the study area.

Calibration of the two material parameters, namely the Manning's coefficient, n and the critical slope angle for the deposition, θ_{cr} was demonstrated in the case study of both the Kumamoto debris flow and Hofu shallow landslides. Table 3 recaps the upper and lower bound values of these parameter for the two case study area. In both cases the lower value of n and the upper value $\theta_{cr}$was equivalent except the eastern side of Hofu case study area which as a 4 degree value. The upper value of n and the lower value of θ_{cr} showed some differences.

Table 5 summary of the upper and lower bound values of calibrated material parameter

Case study area	n		θ_{cr} (degree)	
	Lower	upper	Lower	Upper
Hofu area	0.05	0.08	0.5	7 (4)
Kumamoto area	0.05	0.1	5	7

These difference arises due to the problem of predicting accurate initial volume of discharges. The prediction of initial slope failure is still a big issue to be improved. Nakata and Matsushima (2014) attempted a statistical analysis of landslide affected area which suggested the importance of considering the rain water catchment topography in relation to the saturation of soil as many others focused on (Burton and Bathurst 1998, Crosta and Frattini 2003). The difference in the terrain input data used in the two case study area has affected also the magnitude of the two material parameters. Prediction of the flow-path and the deposition fan of the debris flows is found to be more reliable with airborne survey high resolution terrain source compared to a freely available global source. However, calibration of the model parameters using globally available terrain source with identical resolutions all over the world will resolve such differences.

A slope disaster event occurred in the Debre Sina landslide area was large and wide to be clearly identified by the satellite images taken in the near dates of the event. We used some pictures and panoramic photos of the slope disaster event taken by previous researchers to evaluate images taken by the satellites. Identical morphological features were identified both in the pictures and in the satellite images.

We used these satellite images to make a calibration of the critical slope failure angle in order to identify the initial slope failure area. A similar approach proposed by Galas et al (2007) was adopted with addition of an index value to separately maximize the intersection between the predicted and observed failure area and both failure and the safe area distinctly. It was found that the index values were maximum until a critical slope failure angle of 32 degree.

A relatively higher number of simulated raindrops were also found corresponding to the main and major initial slope failure area. We used this threshold value to predict the places in the eastern and western peripheries where no signs of sliding was seen on the satellite images taken in the year 2007. After estimating the initial slope failure area we used the calibrated material parameters of the model to replicate the past landslide event. The replication of past landslide event was made using two extreme cases of the calibrated parameters, namely the lower bound values ($n = 0.05$ and $\theta_{cr} = 0.5\ deeree$) and upper limit values ($n = 0.08$ and $\theta_{cr} = 7\ degree$).

The lower bound values replicated a simulation debris mass under highly fluidized condition thus the flows involved several number of surges which led to a high impact energy, that represent one

of the most destructive cases. These replicated results were in agreement with the investigations made in the study area by previous researchers. In the case of upper bound values the simulation results reproduces a deposition of debris flows with shorter runout distances both in the upper slope failure area and the lower river canals.

The model can be used for both back analysis (simulation) of previous events and the forward-analysis (prediction or forecasting) of potential future events. The outcomes of the simulation results have revealed that the model reasonably reproduces the initial slope failure zone and the observed deposition area of the documented landslide event in the study area. Such an efforts will be helpful for prediction of possible future wide area slope disaster events in the neighboring areas. The capability of the model to reproduce a past event using a calibrated the parameters found from a well-documented case study area remains to be an essential achievements.

Ankober area is located at the edge of the eastern side of the EMR closer to the Debre Sina landslide area. It is characterized by a similar seismicity and geological characteristics. Both the Ankober and the Debre Sina area are near to the Afar Triangle where several old and recent volcanic eruptions are believed to exist due to existence of one or two Paleogene mantle plumes underneath the thin crust in this area (Schilling et al 1992; Ebinger and Sleep 1998).

A quantitative records of the past landslide events is not available in the Ankober area. Moreover, in-situ mechanical test records of the geomaterials are also rarely available. We used the topographic map of the study area together with the satellite images taken in the year 2019 to identify the places that demands to be protected primarily such as villages, roads, and forest covered areas. We identify also forest covered fertile areas that need to be most protected because slope failure disasters causes surface erosion of the fertile soil covers and results in deforestations in several cases.

Due to absence of the required data including the unsaturated and saturated bulk density of the soil mass as well as porosity n of the surface soil was not available to compute the slope angle corresponding the safety factor value. Therefore, we set a higher critical slope failure angle θ_f to predict the initiation area. From the overlap of the predicted slope disaster area and the topographic map it was seen that the eastern and western side of Ankober town, the road that connects to the capital city and the forest cover area are found to be near the predicted dangerous slope failure zones.

Before we made a flow spreading simulations using the two extreme cases of the calibrated parameters, we made a precipitation simulations to identify the most vulnerable places for surface erosions and debris flow deposition areas. The result showed a high concentrations of simulated raindrops in the eastern most side of the study area. Then a flow spreading simulations were made using the two extreme cases of the calibrated parameters, namely the lower bound values (n=0.05 and θ_{cr}=0.5 degree) and upper limit values (n=0.08 and θ_{cr}=7 degree). In both cases of the simulation results obtained by the calibrated parameters lower and upper bound values, it was seen that the identified places such as villages, roads, and forest covered area that necessitates to be protected primarily were simulated to be under high slope disaster risks. Moreover from the overlap of the simulated results and the satellite images, it was found that the most possible debris flows occurrence could be in the flood plains covered with trees or heavy brush, whose Manning's coefficient *n* is about a value of 0.1.

A most dangerous case of a flow was also assumed and θ_{cr} was set to a zero value. The results found using these material parameters showed a wide inundated area having a high value of velocity and it covers relatively large number of houses.

The predicted flow velocity at the initial stage was much higher than the previous case study areas due to a comparatively steep slope failure angle value more than 45 (deg.) occur in this area. The mean velocity of the predicted flow was found to be quite large value compared to the mean velocities of common debris flows under a channel gradients varying from about 40° in the starting zones to about 3° in the deposition zone (Hutter et al 1994). In general, the results showed the potential damages of slope disaster risks in the area and the necessity for further investigations.

7.2 Recommendations

The key issue here is to develop a method that is capable to obtain important material parameters from available in situ records that show the initial slope disaster locations as well as the extent and distributions of the debris flow surges in the given area. The availability of a model that can be integrated with a terrain model obtained from a global freely available sources though an open source Grass GIS application make it essentially applicable all over slope disaster susceptible places for both experts and practitioners, while models that are commercially available tend to be expensive. Moreover the model results are found to be directly applicable into risk assessment calculations in order to be used as a visualization and communication tools.

However, several key challenges remain, particularly the sensitivity of models to topographic resolution. Prediction of the flow-path and the deposition fan of the debris flows is found to be more reliable with airborne survey high resolution terrain source compared to a freely available global source. However, calibration of the model parameters using globally available terrain source with identical resolutions all over the world will resolve such differences.

It also turned out that the prediction of initial slope failure is still a big issue to be improved. Nakata and Matsushima (2014) attempted a statistical analysis of landslide affected area which suggested the importance of considering the rain water catchment topography in relation to the saturation of soil as many others focused on (Burton and Bathurst 1998, Crosta and Frattini 2003). To improve the accuracy slope failure predictions we incorporated erosion behavior of debris flow into the model. And Zhang and Matsushima (2016) proposed a simple diffusion model to describe the entrainment of debris material resting on the valley bottom by the flow.

In addition to these (Mcdougall 2016) recommended that, other emerging topics that warrant more attention from researchers and practitioners need improved model efficiency and user-friendliness, including shorter model setup, run times, and processing times. Improved model availability and cost, improved simulation of mitigation elements and integration of model results directly into risk assessment calculations remains to be the biggest challenges.

Moreover, it should be recognized that calibrated parameter values can depend strongly on the roughness of the input topography; therefore, until a standard approach to model setup is adopted widely, calibration results documented by different workers using different models may not be directly comparable. Therefore, the model need to be applied to several case studies in central and escarpment area of the highlands of Ethiopia in order to create a valuable database of calibrated parameters. Detail geotechnical field investigations and laboratory works need be done to adjust the input parameters for specific to the geologic and topographic conditions of Ethiopian highlands.

Acknowledgements

First and foremost, praised be He the Glorious and the Merciful. Next, I would like to sincerely thank my supervisor Professor Matsushima. Without his assistance and guidance this thesis would not exist. I am grateful to him for his perseverance and persistent support both in this and the master's thesis works. If it were not for his kindness that let me feel relax and if it were not for his passions that encouraged me to work hard, it is unimaginable to attain this accomplishment. I'd like to express my sincere gratitude to him once again.

I am also thankful to my co-advisors professor Shoji and assistance professor Yamamoto, who provided me not only with valuable advices in this thesis works, but also with their knowledge as professors in my classes. I am also grateful and thankful to professor Hattanji for his valuable comments on the detail technical subjects and for his diligent corrections of the entire thesis. I am thankful also for the president of the University of Tsukuba for the offers I received both in the financial assistances from the scholarship grants and the tuition fee exceptions. Thanks also to Japan students Organization (JASSO) for offering me a financial assistances.

I would like to express my thanks to the Geotechnical and to all Frontier Lab members. Thanks former graduate student Dr. Guo for his considerate helps.

Finally, I would like to thank my parents. Special thanks to my mom, for that I am, or what I aspire to be, I am indebted to her.

References

Abay, Asmelash, and Giulio Barbieri. "Landslide susceptibility and causative factors evaluation of the landslide area of Debresina, in the southwestern Afar escarpment, Ethiopia." *Journal of Earth Science and Engineering* 2.3 (2012).

Abebe, Bekele, et al. "Landslides in the Ethiopian highlands and the Rift margins." *Journal of African Earth Sciences* 56.4-5 (2010): 131-138.

Abebe, Bekele, et al. "Landslides in the Ethiopian highlands and the Rift margins." *Journal of African Earth Sciences* 56.4-5 (2010): 131-138.

Aipassa, Marlon Ivanhoe. "Landslide debris movement and its effects on slope and river channel in mountainous watershed." *RESEARCH BULLETINS OF THE COLLEGE EXPERIMENT FORESTS HOKKAIDO UNIVERSITY* 48.2 (1991): 375-418.

Alahmadi, Fahad S. "Evaluation of global digital elevation model ALOS/PALSAR using aerial LiDAR." The 12th GIS Symposium in Saudi Arabia held on 11th of April 2018 https://www.iau.edu.sa/en/events/gis-symposium

Alemayehu, L.; Gerra, S.; Zvelebil, J.; Šíma, J. Landslide Investigations in Tarmaber, Debre Sina, North Shewa Zone; Amhara Regional State; AQUATEST a.s.: Prague, Czech Republic, 2012.

Asfaw, Y. E. "Landslide Assessment in Blue Nile Gorge, Central Ethiopia." *Master Thesis, University Gent* (2010).

Ayalew, Lulseged, and Hiromitsu Yamagishi. "Slope failures in the Blue Nile basin, as seen from landscape evolution perspective." *Geomorphology* 57.1-2 (2004): 95-116.

Barnes, H.H., Jr., 1967, Roughness characteristics of natural channels: U.S. Geological Survey Water-Supply Paper 1849,213 p.

Canuti, P., P. Focardi, and C. A. Garzonio. "Correlation between rainfall and landslides." *Bulletin of the International Association of Engineering Geology-Bulletin de l'Association Internationale de Géologie de l'Ingénieur* 32.1 (1985): 49-54.

Chow, Ven T. "Open-channel hydraulics." McGraw-Hill civil engineering series (1959).

Cundall, P. A., Strack, O. D. (1979). A discrete numerical model for granular assemblies. geotechnique, 29(1), 47-65.

Cundall, Peter A., and Otto DL Strack, "A discrete numerical model for granular assemblies" *geotechnique* 29.1 (1979): 47-65.

Dai, F. C., and C. F. Lee. "Landslide characteristics and slope instability modeling using GIS, Lantau Island, Hong Kong." *Geomorphology* 42.3-4 (2002): 213-228.

Dai, F. C., C. F. Lee, and Y. Yip Ngai. "Landslide risk assessment and management: an overview." *Engineering geology* 64.1 (2002): 65-87.

Devoli G, Blasio FV, Elverhøi A, Høeg K (2008) Statistical analysis of landslide events in Central America and their run-out distance. Geotech Geol Eng 27(1):23–42

Duncan, J. Michael, Stephen G. Wright, and Thomas L. Brandon. *Soil strength and slope stability*. John Wiley & Sons, 2014.

Ebinger, C.J. and Sleep, N.H. (1998) Cenozoic magmatism throughout east Africa resulting from the impact of a single plume. *Nature*, 395, 788 – 791.

Ercanoglu, Murat, and Candan Gokceoglu. "Assessment of landslide susceptibility for a landslide-prone area (north of Yenice, NW Turkey) by fuzzy approach." Environmental geology 41.6 (2002): 720-730.

Fellenius, Bengt. *Basics of foundation design*. Lulu. com, 2017.

Froude, Melanie J., and D. Petley. "Global fatal landslide occurrence from 2004 to 2016." *Natural Hazards and Earth System Sciences* 18 (2018): 2161-2181.

Fubelli, G., et al. "Geomorphological evolution and present-day processes in the Dessie Graben (Wollo, Ethiopia)." *Catena* 75.1 (2008): 28-37.

Fubelli, Giandomenico, and Francesco Dramis. "Geo-hazard in Ethiopia." *Landscapes and Landforms of Ethiopia*. Springer, Dordrecht, 2015. 351-367.

Getahun, YS, and SL Gebre. "Flood hazard assessment and mapping of flood inundation area of the Awash River basin in Ethiopia using GIS and HEC-GeoRAS / HEC-RAS model." *Journal of Civil & Environmental Engineering* 5.4 (2015):

Gingold, R.A., and Monaghan, J.J. 1977. Smoothed particle hydrodynamics: theory and application to non-spherical stars. Monthly Notices of the Royal Astronomical Society, 181: 375–389. doi:10.1093/mnras/181.3.375.

Griffiths, D. F., and J. Lorenz. "An analysis of the Petrov—Galerkin finite element method." *Computer Methods in Applied Mechanics and Engineering* 14.1 (1978): 39-64.

Hagos, A.A. Remote sensing and GIS-based mapping on landslide phenomena and landslide susceptibility evaluation of Debresina Area (Ethiopia) and Rio San Girolamo basin (Sardinia). Ph.D. Thesis, Universita degli Studi di Cagliari, Cagliari, Italy, 2012.

Hakuno, Motohiko, and Yoshihiko Uchida. "Application of the distinct element method to the numerical analysis of debris flows." *Doboku Gakkai Ronbunshu* 1991.432 (1991): 31-41.

Haregeweyn, Nigussie, et al. "Comprehensive assessment of soil erosion risk for better land use planning in river basins: Case study of the Upper Blue Nile River." *Science of the Total Environment* 574 (2017): 95-108.

Hayes, Gavin P., et al. *Seismicity of the Earth 1900-2013 East African Rift*. No. 2010-1083-P. US Geological Survey, 2014.

Hervouet, J.M. (2007) Hydrodynamics of free surface flows: modelling with the finite element method (Vol. 360). New York: Wiley.

Hoang, G.Q., Matsushima, T., Yamada, Y., 2009. Debris flow simulation by particle method using PRISM-DSM. Proceedings of 6th Geo-Kanto Conference (in Japanese).

Hoffman JD; Frankel S (2001). *Numerical methods for engineers and scientists*. CRC Press, Boca Raton

http://floodlist.com/africa/ethiopia-landslide-south-east-dawuro-september-2019

Hübl, J., and H. Steinwendtner. "Two-dimensional simulation of two viscous debris flows in Austria." *Physics and Chemistry of the Earth, Part C: Solar, Terrestrial & Planetary Science* 26.9 (2001): 639-644.

Huggel C, Schneider D, Julio Miranda P, Delgado Granados H, Kääb A (2008) Evaluation of ASTER and SRTM DEM data for lahar modeling: a case study on lahars from Popocatépetl volcano, Mexico. J Volcanol Geotherm Res 170:99–110

Hungr O, Evans SG, Bovis MJ, Hutchinson JN (2001) A review of the classification of landslides of the flow type. Environ Eng Geosci 7(3):221–238

Hungr, O., Morgan, G. C., Kellerhals, R. (1984). Quantitative analysis of debris torrent hazards for design of remedial measures. Canadian Geotechnical Journal, 21(4), 663-677.

Hungr, Oldrich, F. M. Salgado, and P. M. Byrne. "Evaluation of a three-dimensional method of slope stability analysis." *Canadian geotechnical journal* 26.4 (1989): 679-686.

Hungr, Oldrich. "A model for the runout analysis of rapid flow slides, debris flows, and avalanches." Canadian Geotechnical Journal 32.4 (1995): 610-623.

Hutter, K., B. Svendsen, and D. Rickenmann. "Debris flow modeling: A review." *Continuum mechanics and thermodynamics* 8.1 (1994): 1-35.

Imamura, F. "Review of tsunami simulation with a finite difference method." *Long-wave runup models* (1996): 25-42.

Iverson, Richard M., and David L. George. "Modelling landslide liquefaction, mobility bifurcation and the dynamics of the 2014 Oso disaster." Géotechnique 66.3 (2015): 175-187.

Iwao, Y. (2003). Slope hazard induced by heavy rain in 2003, Minamata City, Kumamoto. Journal of the Japan Landslide Society, 40(3), 239-240 (in Japanese).

Jaluria Y; Atluri S (1994). "Computational heat transfer". *Computational Mechanics*. **14**: 385–386.

Kalkwijk, J. T., De Vriend, H. J. (1980). Computation of the flow in Shallow River bends. Journal of Hydraulic Research, 18(4), 327-342.

Koch, Thilo, Ralf Greve, and Kolumban Hutter. "Unconfined flow of granular avalanches along a partly curved surface. II. Experiments and numerical computations." Proceedings of the Royal Society of London. Series A: Mathematical and Physical Sciences 445.1924 (1994): 415-435.

Kropáček, Jan, et al. "Remote sensing for characterisation and kinematic analysis of large slope failures: Debre sina landslide, main ethiopian rift escarpment." *Remote Sensing* 7.12 (2015): 16183-16203.

Liu, Gui-Rong, and Moubin B. Liu. *Smoothed particle hydrodynamics: a meshfree particle method*. World scientific, 2003.

Liu, Gui-Rong. *Meshfree methods: moving beyond the finite element method*. CRC press, 2009.

Loew, S., Gschwind, S., Gischig, Keller-Signer, A., and Valenti, G. 2016. Monitoring and early warning of the 2012 Preonzo catastrophic rockslope failure. Landslides. doi:10.1007/s10346-016-0701-y.

Lucy, L.B. 1977. A numerical approach to the testing of the fission hypothesis. Astrophysical Journal, 82(12): 1013–1024. doi:10.1086/112164.

Matsui, Tamotsu, and Ka-Ching San. "Finite element slope stability analysis by shear strength reduction technique." *Soils and foundations* 32.1 (1992): 59-70.

McDougall, S., Hungr, O., 2004. A model for the analysis of rapid landslide motion across three-dimensional terrain. Can. Geotech. J. 41, 1084–1097.

McDougall, Scott. "2014 Canadian Geotechnical Colloquium: Landslide runout analysis—current practice and challenges." Canadian Geotechnical Journal 54.5 (2016): 605-620.

Nakata Alexandra Mayumi. *Evaluation of wide-area landslide hazard using depth-integrated particle method and GIS*. Diss. 筑波大学 (University of Tsukuba), 2016.

Nakata Mayumi Alessandra, *Evaluation of wide-area landslide hazard using depth-integrated particle method and GIS*. Diss. (University of Tsukuba), 2016.

Nakata, A.M., Matsushima, T., Statistical evaluation of damage area due to heavy-rain-induced landslide, Computer Methods and Recent Advances in Geomechanics (IACMAG), Oka, Murakami, Uzuoka & Kimoto Eds., Taylor and Francis, 1523-1528, 2014

Nakazawa T, Saito M, Taguchi Y (2003) Geologic and hydrologic background of slope failure and debris-flow disaster in Atsumari River Basin, Minamata City, Kumamoto Prefecture on July 20, 2003. Bull Geol Surv Jpn 55:113–127 (in Japanese).

Ochoa, Cristian Guevara, et al. "Analysis and Correction of Digital Elevation Models for Plain Areas." *Photogrammetric Engineering & Remote Sensing* 85.3 (2019): 209-219.

Pastor, M., Haddad, B., Sorbino, G., Cuomo, S., Drempetic, V., 2009. A depth-integrated, coupled SPH model for flow-like landslides and related phenomena. Int. J. Numer. Anal. Methods Geomech. 33, 143–172.

Peiró, Joaquim, and Spencer Sherwin. "Finite difference, finite element and finite volume methods for partial differential equations." *Handbook of materials modeling*. Springer, Dordrecht, 2005. 2415-2446.

Pudasaini, S.P., Hutter, K., 2003. Rapid shear flows of dry granular masses down curved and twisted channels. J. Fluid Mech. 495, 193–208.

Pudasaini, Shiva P., and Kolumban Hutter. "Rapid shear flows of dry granular masses down curved and twisted channels." *Journal of Fluid Mechanics* 495 (2003): 193-208.

Renn, Ortwin. "Concepts of risk: an interdisciplinary review part 1: disciplinary risk concepts." *Gaia-Ecological Perspectives for Science and Society* 17.1 (2008): 50-66.

Rickenmann, D., et al. "Comparison of 2D debris-flow simulation models with field events." *Computational Geosciences* 10.2 (2006): 241-264.

Schilling, J.-G, Kingsley, R., Hanan, B. and McCully, B. (1992) Nd-Sr-Pb isotopic variations along the Gulf of Aden: Evidence for the Afar mantle plume-lithosphere interaction. *J. Geophys. Res.*, 97, 10927 – 10966.

Schuster, Robert L., and Robert W. Fleming. "Economic losses and fatalities due to landslides." *Bulletin of the Association of Engineering Geologists* 23.1 (1986): 11-28.

Shang, Yanjun, et al. "A super-large landslide in Tibet in 2000: background, occurrence, disaster, and origin." *Geomorphology* 54.3-4 (2003): 225-243.

Sidle, Roy C., and Masahiro Chigira. "Landslides and debris flows strike Kyushu, Japan." *Eos, Transactions American Geophysical Union* 85.15 (2004): 145-151.

Soeters, Robert, and C. J. Van Westen. "Slope instability recognition, analysis and zonation." *Landslides: investigation and mitigation* 247 (1996): 129-177.

Sosio, R., G. B. Crosta, and P. Frattini. "Field observations, rheological testing and numerical modelling of a debris-flow event." *Earth Surface Processes and Landforms* 32.2 (2007): 290-306.

Stevens, N. F., V. Manville, and D. W. Heron. "The sensitivity of a volcanic flow model to digital elevation model accuracy: experiments with digitised map contours and interferometric SAR at Ruapehu and Taranaki volcanoes, New Zealand." Journal of Volcanology and Geothermal Research 119.1-4 (2003): 89-105.

Stolz, Adrian, and Christian Huggel. "Debris flows in the Swiss National Park: the influence of different flow models and varying DEM grid size on modeling results." Landslides 5.3 (2008): 311-319.

Strozzi, Tazio, Christian Ambrosi, and Hugo Raetzo. "Interpretation of aerial photographs and satellite SAR interferometry for the inventory of landslides." Remote Sensing 5.5 (2013): 2554-2570.

Takahashi, T., Das, D. K. (2014). Debris flow: mechanics, prediction and countermeasures. CRC press.

Taniguchi Y (2003) Debris disaster caused by local heavy rain in Kyushu area on July 20th, 2003 (prompt report), Minamata debris disaster. J Jpn Soc Erosion Control Eng 56:31–35 (in Japanese).

Tiberi, Christel, et al. "Inverse models of gravity data from the Red Sea-Aden-East African rifts triple junction zone." Geophysical Journal International 163.2 (2005): 775-787.

VanDine, D. F. (1985). Debris flows and debris torrents in the southern Canadian Cordillera. Canadian Geotechnical Journal, 22(1), 44-68.

Varnes D.J., (1996).Landslide Types and Processes. In: Turner, A.K., and R.L.Schuster (eds), Landslides: Investigation and Mitigation, Transportation Research Board Special Report 247, National Research Council, Wasington, D.C. N.Academy Press

Wakatsuki Tsuyoshi, Takeaki Ishizawa , Masaki Uetake , and Shinya Kawada "Characteristics of Debris Flow and Slope Failure on Granite Slopes Caused by Heavy Rainfall on July 2009 in Hofu and Yamaguchi Cities, Japan" (in Japanese) www.bosai.go.jp/activity_general/nenpo/img/012_22nenpou_2.pdf

Wang, C., Esaki, T., Xie, M., Qiu, C. (2006). Landslide and debris-flow hazard analysis and prediction using GIS in Minamata–Hougawachi area, Japan. Environmental Geology, 51(1), 91-102

Woldearegay, Kifle. "Review of the occurrences and influencing factors of landslides in the highlands of Ethiopia: With implications for infrastructural development." *Momona Ethiopian Journal of Science* 5.1 (2013): 3-31.

Yamashita Kumiko, Tsuyoshi Hattanji, Yasushi Tanaka, Shoji Doshida and Takashi Matsushima, "Topographic characteristics of rainfall-induced shallow landslides on granitic hillslopes: A case study in Hofu City, Yamaguchi Prefecture, Japan" ,Tsukuba Geoenvironmental Sciences, Vol. 13, pp. 23-29, Dec. 22, 2017

Zhang, N., Matsushima, T., Simulation of rainfall-induced debris flow considering material entrainment, Engineering Geology, 214, 107-115, 2016

Zhang, Ni, Takashi Matsushima, and Ningbo Peng. "Numerical investigation of post-seismic debris flows in the epicentral area of the Wenchuan earthquake." *Bulletin of Engineering Geology and the Environment* 78.5 (2019): 3253-3268.